[American Journal of Science, Vol. 322, February, 2022, P. 108–163, DOI 10.2475/02.2022.02]

# PALEO- TO MESOARCHEAN CRUSTAL GROWTH IN THE KARWAR BLOCK, SOUTHERN INDIA: CONSTRAINTS ON TTG GENESIS AND ARCHEAN TECTONICS

C. ISHWAR-KUMAR*†, K. SAJEEV**, M. SATISH-KUMAR***, IAN S. WILLIAMS§, SIMON A. WILDE§§, T. HOKADA§§§, and BRIAN F. WINDLEY‡

**ABSTRACT. In this study we present field relations, petrology, whole-rock major, trace and rare earth element geochemistry, zircon U-Pb ages, whole-rock Sr and Nd isotopes, and *in situ* zircon Hf and O isotopes from the Karwar block, western peninsular India. The rocks consist predominantly of tonalite-trondhjemite-granodiorite (TTG), granite and amphibolite. The felsic rocks are grouped into three: 1. TTG-I characterised by low $K_2O$, high $Na_2O$ and $Al_2O_3$, low Sr/Y and La/Yb ratios, slightly enriched HREEs, negative Sr, Eu and Ti anomalies, a 3.2 Ga crystallisation age, and 3.60 Ga and 3.47 Ga inherited zircons; 2. TTG-II with lower $SiO_2$, higher Sr/Y and La/Yb ratios, stronger REE fractionation with no HREE enrichment, negative Nb and Ta anomalies, a 3.2 Ga crystallisation age, but no inheritance; 3. Granites with high $SiO_2$ and $K_2O$, low $Na_2O$ and $Al_2O_3$, very low Sr/Y and La/Yb ratios, weak REE fractionation with enriched REEs, negative Sr, Eu and Ti anomalies and a 2.94 Ga crystallisation age. The TTG-I formed from a mantle source, but with a significant component of older crustal material, whereas the TTG-II originated mostly from a mantle-derived juvenile magma. The granite evolved from an enriched source containing a relatively large amount of older crustal material. The precursors of TTG-I and -II are similar to mid-ocean ridge basalts (MORB), whereas the granites are similar to volcanic arc/within-plate sources and the amphibolites are remnants of gabbros/basalts. An initial 3.6 Ga crust likely formed by the underplating of an accreted oceanic plateau-like or island arc-like crust. TTG-I was produced by subduction and slab melting at a moderate depth, induced melting of mafic lower crust and older upper crust at 3.2 Ga. TTG-II formed at 3.2 Ga by subduction and with a higher degree of slab melting at a greater depth than TTG-1, together with more effective mixing with mantle peridotite, followed by intrusion and induced melting of mafic lower crust. Basaltic magmatism at 3.0 Ga and subsequent metamorphism to amphibolite resulted in extensive and thicker crust. Assimilation and melting of TTG crust at a shallow depth during the emplacement of a mantle-derived magma produced the 2.94 Ga granites. The presence of inherited zircons, combined with whole-rock major and trace elements, Nd isotopes and *in situ* zircon Hf and O isotopes, indicates that older crustal material was incorporated into the source magma of TTG-I and that the Karwar block originally contained 3.60 to 3.47 Ga crust that was subsequently reworked during the Paleo- and Mesoarchean.**

Key words: Karwar block, India, TTG, Amphibolite, Archean crustal growth, U-Pb geochronology, *In situ* Zircon Hf and O isotopes, Geochemistry, Sr and Nd isotopes

* Department of Earth Sciences, Indian Institute of Technology Kanpur, Kanpur 208 016, India
** Centre for Earth Sciences, Indian Institute of Science, Bangalore 560 012, India
*** Department of Geology, Faculty of Science, Niigata University, Niigata, Japan
§ Research School of Earth Sciences, The Australian National University, Canberra, ACT, 2601, Australia
§§ School of Earth and Planetary Sciences, Curtin University, Bentley, Western Australia 6102, Australia
§§§ National Institute of Polar Research,10-3 Midori-cho, Tachikawa, Tokyo 190-8518, Japan
‡ School of Geography, Geology and the Environment, The University of Leicester, Leicester LE1 7RH, United Kingdom
† Corresponding author: C. Ishwar-Kumar: e-mail: ishwar@iitk.ac.in; krishnaisha@gmail.com

## INTRODUCTION

The majority of the present-day continental crust has its origins in the Archean, the remnants of which have been recycled many times throughout Earth history (for example, Armstrong, 1981; Taylor and McLennan, 1985; Hawkesworth and others, 2010; Cawood and others, 2013). These crustal rocks preserve valuable information about early Earth processes, including crustal formation and evolution, although in many Archean terranes they have been extensively deformed, metamorphosed and reworked. Archean rocks are preserved in *ca.* 35 cratons and in many smaller fragments worldwide (Bleeker, 2003). Eo-(4.0–3.6 Ga), Paleo-(3.6–3.2 Ga) and early Mesoarchean (*ca.* 3.2 Ga) crust is preserved in several terranes. For example, the *ca.* 4.0 to 3.9 Ga Acasta gneiss (Bowring and Williams, 1999), the *ca.* 3.95 Ga Nulliak supracrustal belt (Komiya and others, 2015), and the *ca.* 3.75 Ga Nuvvuagittuq belt (O'Neil and others, 2012) in Canada; the 3.9 to 3.6 Ga Itsaq-Isua-Akillia belt in Greenland (Nutman and others, 2015); the remainder of the Archean craton of Greenland (Garde and others, 2020); the *ca.* 3.8 Ga Napier complex in Antarctica (Guitreau and others, 2019); the 3.5 to 3.16 Ga East Pilbara belt (Van Kranendonk and others, 2015) and the 3.3 to 3.2 Ga West Pilbara belt at Cleaverville (Ohta and others, 1996) in Australia; the *ca.* 3.8 Ga North China (Liu and others, 2008) and the 3.45 to 3.2 Ga South China (Guo and others, 2014) cratons; the Kaapvaal craton in South Africa (De Wit and others, 2011); the 3.75 to 3.1 Ga Ukrainian Shield (Kushev and Kornilov, 1997); the 3.4 to 3.3 Ga São Francisco craton in Brazil (Zincone and others, 2016); the 3.5 to 3.3 Ga Singhbhum craton (Mishra and others, 1999) and 3.45 to 3.2 Ga Western Dharwar craton (Jayananda and others, 2018), India.

The tonalite-trondhjemite-granodiorite (TTG) suite was more common in the early Earth than in the Phanerozoic and thus provides invaluable information about how tectonic, magmatic and differentiation processes have changed as the Earth evolved through time (Moyen and Martin, 2012). Early Archean TTG rocks are considered to have formed by the subduction and partial melting of hydrated oceanic crust (Condie, 1986; Martin, 1986; Drummond and Defant, 1990; Feng and Kerrich, 1992; Taylor and McLennan, 1995; Windley, 1996; Foley and others, 2002; Rollinson, 2010; Moyen, 2011; Moyen and Martin, 2012). Alternative models for TTG genesis include partial melting at the base of thickened mafic crust by underplating (Atherton and Petford, 1993; Smithies, 2000; Bédard and others, 2003; Turkina and Nozhkin, 2003; Condie, 2005; Foley, 2008; Hastie and others, 2010), or partial melting of tectonically thickened island arc crust (Adam and others, 2012; Nagel and others, 2012). Martin and others (2014) proposed that TTG originated from the subduction of oceanic plateaux, recognising that crustal growth was episodic. However, based on the analysis of an extensive database of detrital zircons, Spencer (2020) suggested that growth of continental crust was continuous, although the style of tectonic processes has evolved through time. Furthermore, Johnson and others (2017) envisaged that Earth's first stable continents formed not by subduction, but near the base of a thick, plateau-like basaltic crust, accordingly Archean tectonics were different from modern-style plate tectonics. Windley and others (2021) also considered accretionary orogens and proposed that modern-style plate tectonics started by the Eoarchean.

The Archean terranes in southern India are dominated by TTG and associated volcano-sedimentary greenstone belts. The TTG are generally weakly to moderately deformed and most contain mafic enclaves or bands of amphibolites. These TTG-amphibolite associations are ideal for the study of Archean tectonics and crustal growth processes. The Karwar block in the western part of peninsular India (fig. 1), is one of those rare locations where early Archean crust is well preserved, containing Mesoarchean TTG, granites and amphibolites (Ishwar-Kumar and others, 2013, 2014), most of which are weakly to moderately deformed.

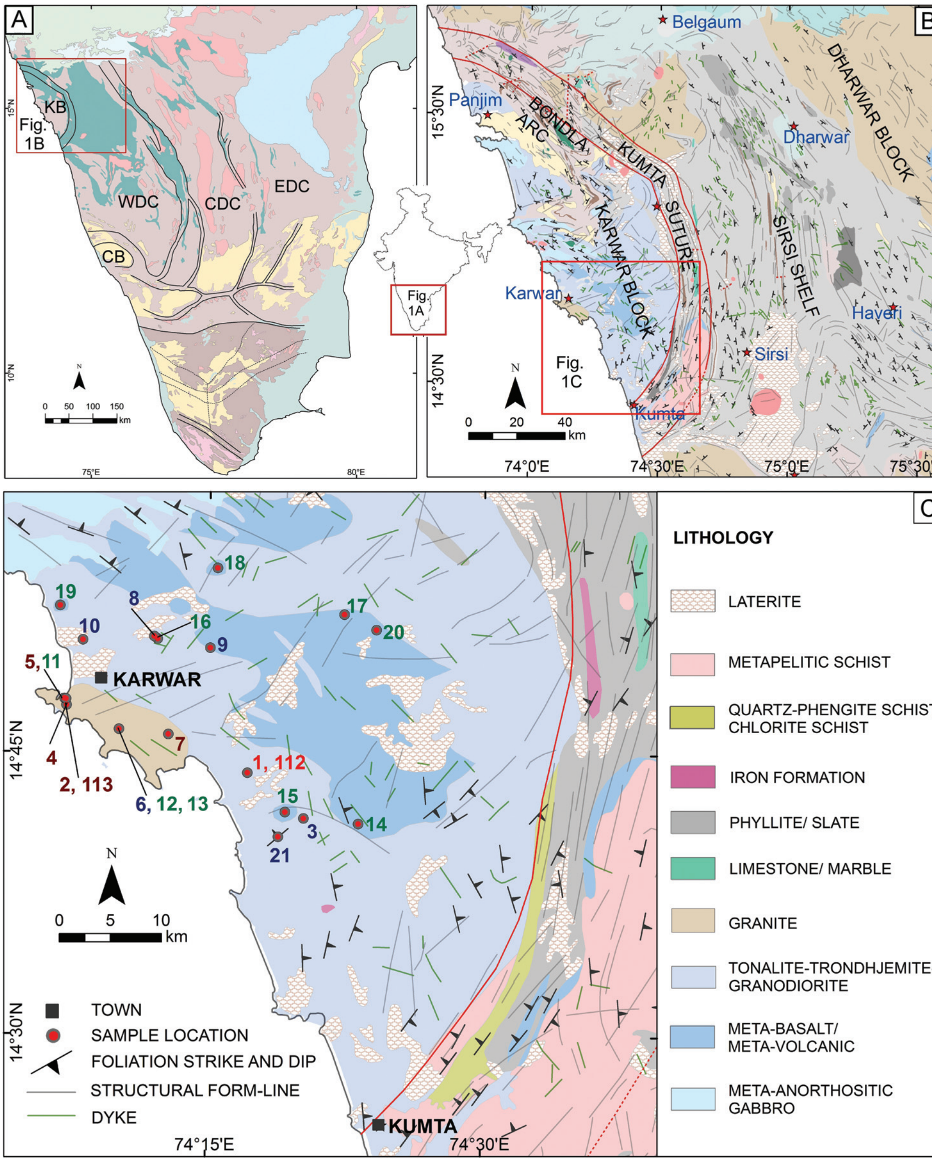


Fig. 1. A. Tectonic map of southern India (after Geological Survey of India, 2005; shear zones are after Ishwar-Kumar and others, 2013). The inset shows location of figure 1A within India. The rectangle in figure 1A marks the Karwar region shown in figure 1C, (KB-Karwar block, CB-Coorg block, WDC-Western Dharwar Craton, CDC-Central Dharwar Craton, EDC-Eastern Dharwar Craton). B. Regional geological map of the Karwar region (after Geological Survey of India, 1993, 1996 and 2005; Ishwar-Kumar and others, 2013; structural lineaments were extracted from Landsat ETM$^+$ satellite imagery and ASTER digital elevation model). The rectangle marks the location of figure 1C. C. Sample locations of TTG, granites and amphibolites and structural lineaments are overlain on the geological map of the southern Karwar block (modified after Geological Survey of India, 1993, 1996 and 2005; Ishwar-Kumar and others, 2013).

Many studies have been conducted on the Archean tectonics and crustal growth in southern India especially in the Dharwar craton (for example, Jayananda and others, 2006, 2008, 2013, 2015, 2018, 2020; Chardon and others, 2008; Hokada and others, 2013; Peucat and others, 2013; Dey, 2013; Manikyamba and others, 2017;

Guitreau and others, 2017; Ratheesh-Kumar and others, 2016, 2020; Sreehari and others, 2021; Vasanthi and Santosh, 2021). However few studies have been conducted on TTG genesis and the processes of Archean crustal growth from the Karwar block and on relations with adjacent crustal domains, even though it contains some of the oldest crust in southern India. A detailed study of Mesoarchean TTG is also important since it is proposed that the transition from a vertically-dominated to a horizontally-dominated style of tectonics occurred during this period (Næraa and others, 2012; Johnson and others, 2019). Hence, this multidisciplinary study, including field investigation, petrography, whole-rock major and trace element analysis, zircon U-Pb geochronology, whole-rock Sr and Nd isotope geochemistry, and *in situ* zircon Hf and O isotope analysis, provides a greater understanding of the Paleo- to Mesoarchean crustal growth processes in the Karwar block and the petrogenesis of TTG in this critical time period.

## REGIONAL GEOLOGY AND GEOLOGICAL BACKGROUND

The Karwar block, in western peninsular India (fig. 1A, B), lies to the south of the Deccan volcanics and consists mostly of TTG and granites, with associated amphibolites. The Bondla arc in the north-eastern Karwar block (fig. 1B) is a mafic-ultramafic complex consisting of gabbro, dolerite, chromitite, serpentinite, pyroxenite and peridotite (Jena, 1985; Dessai and others, 2009; Ishwar-Kumar and others, 2013, 2016a). The Karwar block is separated from the Dharwar craton in the east by the Mesoproterozoic Kumta suture, a *c.* 15 km-wide zone of greenschist to amphibolite facies quartz-phengite schist, garnet-biotite schist, chlorite schist, fuchsite schist and marbles (Ishwar-Kumar and others, 2013, 2016b) (fig. 1B). Published U-Th-Pb monazite ages of gneisses from the Karwar block are 3154 to 3138 Ma and for granitoids 2924 to 2500 Ma (Rekha and others, 2013). Detrital zircon U-Pb ages from the Karwar block are likewise bimodal; a *ca.* 3100 Ma population with relatively juvenile εHf(t) values, and a more evolved suite at *ca.* 2500 Ma (Armistead and others, 2018). Based on deformation history and Th-U-total Pb monazite ages, a Paleoproterozoic Northern Shear Zone (NSZ) has been proposed in the northern part of the Karwar block (Rekha and Bhattacharya, 2013, 2014; Rekha and others, 2014). Based on *in situ* laser ablation Rb-Sr ages of micas and feldspars, coupled with U-Pb zircon ages of rocks from Goa in the northern Karwar block, Li and others (2020) suggested a Mesoarchean (3300 to 3000 Ma) supracrustal formation event, younger Neoarchean and Paleoproterozoic granite formation, and Mesoproterozoic (*ca.* 1200 Ma) metamorphism. Based on positive εHf(t) values they proposed magma generation mostly from juvenile sources. The Sirsi shelf, along the eastern side of the suture (fig. 1B), is a *c.* 80 km-wide, westerly-dipping sequence of sedimentary and metasedimentary rocks (limestone, phyllite, shale, banded iron formation, sandstone and quartzite), interpreted as the remnants of an unconformable passive continental shelf on the western margin of the Dharwar block (Ishwar-Kumar and others, 2013).

## FIELD RELATIONS AND PETROGRAPHY

The study area is in the southern Karwar block (figs. 1B, C), from where a total of 30 felsic (TTG and granite) and 30 mafic (amphibolite) rock samples were collected (sample locations, field relations and mineral assemblages of representative analyzed samples are given in Appendix table A1 and the sample locations are marked on fig. 1C). The TTG rocks are massive, medium- to coarse-grained, and weakly to moderately deformed (figs. 2A, B). Locally, the TTG contain enclaves or bands of amphibolite (figs. 2A, D), both of which are intruded by quartz veins and pegmatite dikes (figs. 2C, E). The amphibolites associated with TTG are fine- to medium-grained and moderately deformed (figs. 2A, B). Locally, these amphibolites are foliated, fine-grained

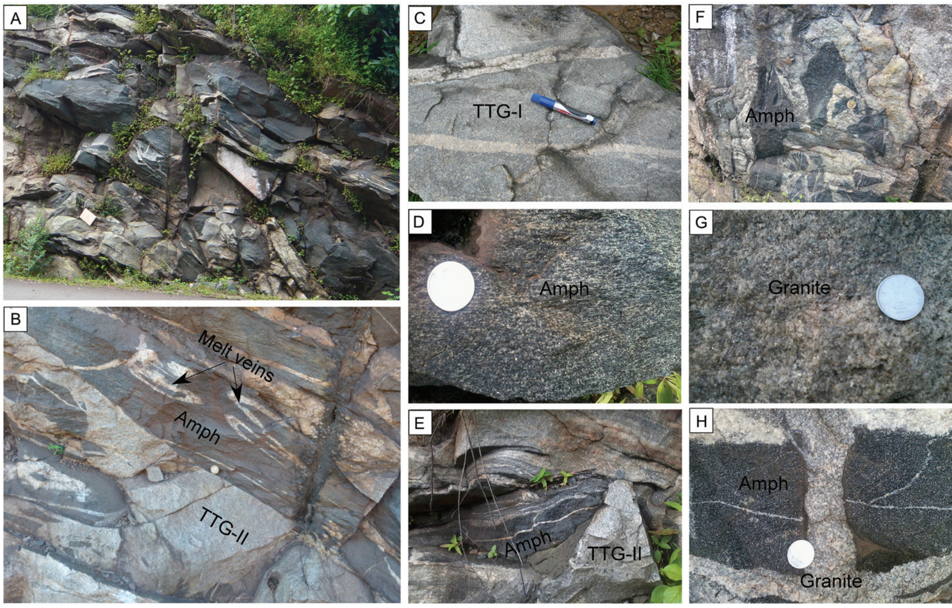


Fig. 2. Field photographs. A. A road-cut exposure of TTG-II and amphibolite cut by leucocratic veins. B. Amphibolite and TTG-II; the amphibolite contains isoclinally folded granitic veins. C. TTG-I intruded by quartz-rich veins. D. Close-up of amphibolite associated with TTG-II, showing preferred orientation of amphibole crystals. E. TTG-II associated with amphibolite bands and melt veins. F. Amphibolite enclaves with melt veins in granite. G. Close-up of fine- to medium-grained granite. H. Close-up photograph of amphibolite enclave within granite.

and contain isoclinally-folded leucocratic veins (fig. 2B). The granites are medium- to coarse-grained, heterogeneous, intruded by leucocratic veins (figs. 2F, G), and contain enclaves and bands of amphibolite (fig. 2H).

The dominant TTG rocks in the Karwar block consist of plagioclase (~45%), quartz (~30%), biotite (~8%) and amphibole (~7%). The quartz and plagioclase are medium- to coarse-grained and plagioclase is euhedral to anhedral and partly sericitized. Amphibole and biotite are euhedral to subhedral and fine-grained. The granites consist of K-feldspar (~30%), quartz (~25%), plagioclase (~20%), biotite (~10%) and amphibole (~5%). Quartz, plagioclase and K-feldspar are medium- to coarse-grained; plagioclase and K-feldspar are subhedral to anhedral. The amphibolites associated with TTG mainly consist of amphibole (~45%), plagioclase (~30%), biotite (~8%) and quartz (~7%), whereas the amphibolites associated with the granites consist of amphibole (~50%), plagioclase (~25%), biotite (~10%) and quartz (~5%). Amphibole and plagioclase in amphibolites are medium-grained and sub- to anhedral. Biotite is medium- to coarse-grained and mostly subhedral. Quartz also occurs as inclusions within amphibole and plagioclase. Accessory minerals in the TTG include zircon, pyrite and magnetite; in the granite they include zircon and magnetite; whereas in the amphibolite they include zircon, magnetite, ilmenite, rutile, epidote and titanite (Appendix fig. A1).

## SAMPLE PREPARATION AND ANALYSES

Samples were selected for whole-rock geochemistry based on mineralogy, lack of weathering and spatial distribution. They were cut into small, thin slabs, all the faces were ground to remove the cut-marks, then they were washed with distilled water in

Table 1

*Whole-rock major element data for TTG, granite and amphibolite samples*

| Sl No. | Rock type | $SiO_2$ | $TiO_2$ | $Al_2O_3$ | FeO | MnO | MgO | CaO | $Na_2O$ | $K_2O$ | $P_2O_5$ | LOI | Total |
|---|---|---|---|---|---|---|---|---|---|---|---|---|---|
| IK-1 | TTG-I | 73.73 | 0.18 | 15.14 | 1.10 | 0.02 | 0.32 | 2.12 | 5.49 | 1.66 | 0.05 | 0.42 | 100.23 |
| IK-112 | TTG-I | 73.55 | 0.19 | 15.32 | 1.19 | 0.02 | 0.46 | 2.12 | 5.54 | 1.76 | 0.05 | 0.45 | 100.64 |
| IK-3 | TTG-II | 70.75 | 0.27 | 16.20 | 1.70 | 0.02 | 0.80 | 2.93 | 5.76 | 1.04 | 0.09 | 0.53 | 100.09 |
| IK-6 | TTG-II | 72.04 | 0.25 | 15.96 | 1.44 | 0.02 | 0.65 | 2.45 | 5.72 | 1.57 | 0.08 | 0.48 | 100.66 |
| IK-8 | TTG-II | 73.03 | 0.23 | 15.17 | 1.35 | 0.01 | 0.72 | 1.74 | 5.27 | 2.40 | 0.07 | 0.79 | 100.78 |
| IK-9 | TTG-II | 70.01 | 0.38 | 15.86 | 2.37 | 0.02 | 0.99 | 2.90 | 5.36 | 1.47 | 0.11 | 0.88 | 100.37 |
| IK-10 | TTG-II | 70.67 | 0.35 | 15.91 | 2.10 | 0.02 | 0.90 | 2.64 | 5.69 | 1.38 | 0.11 | 0.52 | 100.30 |
| IK-21 | TTG-II | 74.93 | 0.12 | 14.71 | 1.07 | 0.02 | 0.36 | 1.72 | 6.02 | 1.17 | 0.04 | 0.00 | 100.00 |
| IK-2 | Granite | 74.85 | 0.06 | 14.46 | 0.44 | 0.01 | 0.16 | 0.78 | 3.97 | 5.61 | 0.01 | 0.24 | 100.59 |
| IK-4 | Granite | 74.38 | 0.13 | 14.07 | 1.06 | 0.03 | 0.30 | 0.98 | 4.00 | 4.75 | 0.03 | 0.48 | 100.19 |
| IK-5 | Granite | 75.30 | 0.12 | 13.92 | 1.12 | 0.02 | 0.23 | 0.92 | 4.14 | 4.41 | 0.02 | 0.46 | 100.66 |
| IK-7 | Granite | 75.92 | 0.14 | 13.68 | 0.42 | 0.00 | 0.09 | 1.07 | 4.22 | 4.94 | 0.04 | 0.24 | 100.76 |
| IK-113 | Granite | 73.08 | 0.21 | 14.15 | 1.64 | 0.03 | 0.46 | 1.22 | 3.84 | 4.68 | 0.06 | 0.60 | 99.98 |
| IK-15 | Amphibolite | 50.53 | 1.11 | 13.27 | 13.76 | 0.21 | 6.07 | 10.34 | 2.19 | 0.28 | 0.09 | 1.67 | 99.53 |
| IK-16 | Amphibolite | 49.25 | 1.38 | 13.90 | 11.28 | 0.19 | 7.20 | 12.04 | 1.90 | 0.19 | 0.11 | 2.30 | 99.74 |
| IK-17 | Amphibolite | 52.60 | 1.52 | 11.49 | 13.68 | 0.26 | 4.43 | 10.19 | 2.01 | 0.31 | 0.15 | 2.70 | 99.34 |
| IK-18 | Amphibolite | 51.72 | 0.86 | 13.74 | 10.97 | 0.20 | 6.81 | 11.08 | 2.11 | 0.55 | 0.08 | 2.03 | 100.13 |
| IK-19 | Amphibolite | 52.08 | 1.23 | 13.04 | 13.16 | 0.22 | 5.87 | 10.03 | 2.26 | 0.51 | 0.17 | 1.53 | 100.08 |
| IK-13 | Amphibolite | 52.72 | 1.86 | 13.54 | 12.77 | 0.17 | 4.28 | 7.28 | 3.68 | 1.25 | 0.24 | 2.13 | 99.92 |
| IK-14 | Amphibolite | 46.48 | 3.29 | 12.74 | 15.72 | 0.24 | 4.58 | 8.97 | 2.64 | 0.85 | 1.26 | 2.63 | 99.39 |
| IK-11 | Amphibolite | 50.17 | 0.61 | 14.08 | 9.71 | 0.17 | 9.11 | 10.82 | 2.85 | 0.75 | 0.05 | 1.38 | 99.70 |
| IK-12 | Amphibolite | 50.64 | 0.26 | 16.20 | 7.49 | 0.20 | 7.76 | 13.07 | 2.26 | 0.45 | 0.03 | 1.46 | 99.81 |
| IK-20 | Amphibolite | 55.28 | 0.69 | 8.46 | 9.91 | 0.18 | 11.19 | 9.91 | 1.95 | 0.56 | 0.05 | 1.47 | 99.65 |
| IK-22 | Amphibolite | 49.53 | 1.49 | 12.92 | 15.32 | 0.21 | 6.67 | 9.87 | 2.22 | 0.50 | 0.15 | 1.13 | 100.00 |
| IK-114 | Amphibolite | 50.34 | 1.16 | 13.56 | 13.98 | 0.21 | 5.66 | 8.65 | 2.53 | 0.82 | 0.13 | 2.73 | 99.79 |
| IK-115 | Amphibolite | 50.42 | 1.08 | 13.39 | 13.75 | 0.21 | 6.09 | 10.40 | 2.21 | 0.27 | 0.09 | 1.59 | 99.51 |

an ultrasonic bath, dried, and powdered in a ball mill. Powdered samples were used for whole-rock major, trace, rare earth element (REE) geochemistry and isotopic analyses. To establish the age relationships between the various rock types, U-Pb zircon dating was carried out on TTG-I (description given below) and granite samples, using SHRIMP II. For TTG-II (description given below) SHRIMP U-Pb zircon ages (*ca.* 3201 Ma) were previously reported in Ishwar-Kumar and others (2013) and for amphibolites LA-ICPMS U-Pb zircon ages (*ca.* 3000 Ma) were reported in Ishwar-Kumar (ms, 2015) and Li and others (2020). Zircons were separated by crushing and pulverizing, panning and handpicking under a binocular microscope. The sample locations are given in figure 1C and listed in Appendix table A1. A detailed account of the analytical protocols is provided in the Appendix. The values of standard reference materials for major and trace elements, REE and Sr, Nd isotope analyses are given in Appendix tables A2, A3 and A4 respectively.

## ANALYTICAL RESULTS

### *Whole-Rock Major and Trace Element Compositions*

The felsic samples are grouped into three types based on their composition (fig. 3; Appendix figs. A2, A3; tables 1, 2). The TTG-I samples (IK-1 and IK-112) are defined here as having low Nb, Y, $K_2O$ (< 2 wt.%) and high Sr, $SiO_2$, $TiO_2$, $Al_2O_3$, FeO, MgO, CaO and $Na_2O$ (> 4.2 wt.%) contents (figs. 3A, B, C, F, G; tables 1, 2). The TTG-II samples (IK-3, IK-6, IK-8, IK-9, IK-10 and IK-21) are defined as having very low Nb and Y, and are also characterised by low $SiO_2$ and $K_2O$ (< 3.5 wt.%) and high Sr, V, $TiO_2$, $Al_2O_3$, FeO, MgO, CaO and $Na_2O$ (> 4.2 wt.%) contents (figs. 3A, B, C,

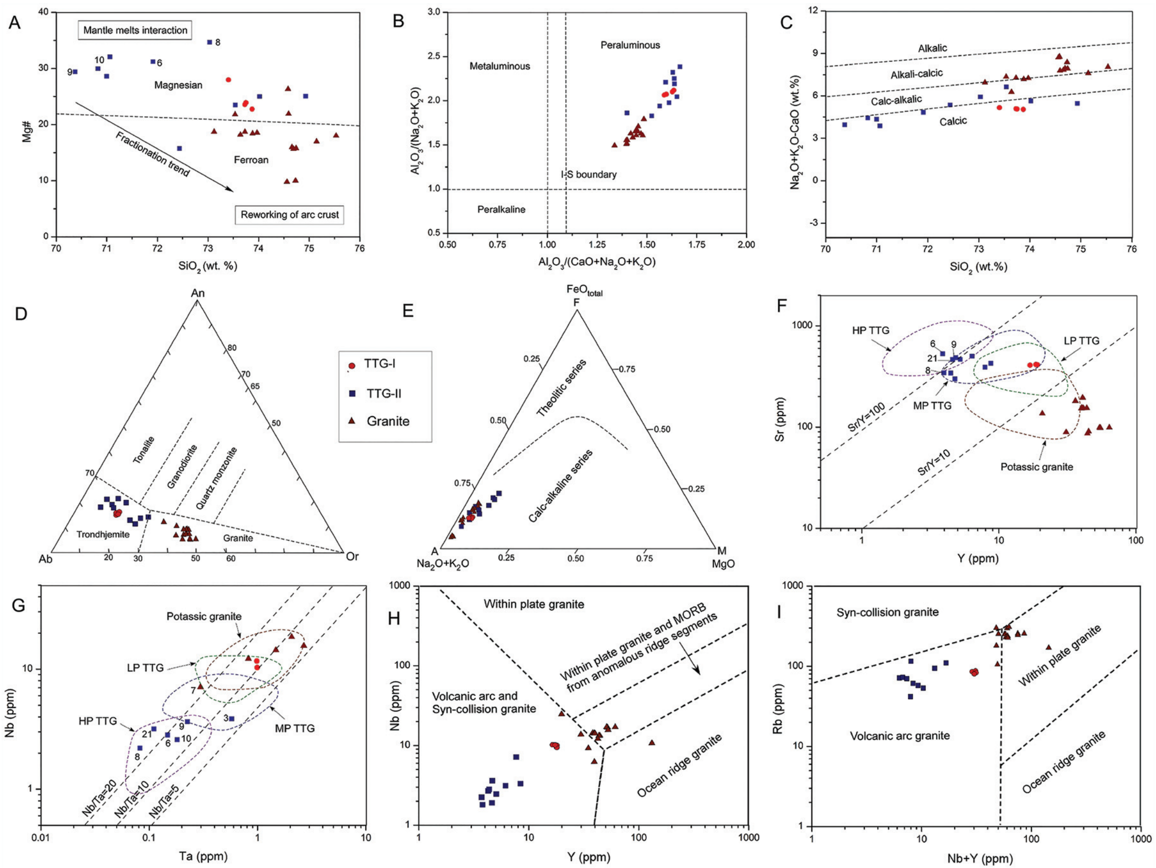


Fig. 3. Discrimination diagrams. A. Mg# vs. $SiO_2$ (wt.%) plot. B. $Al_2O_3/(Na_2O+K_2O)$ vs. $Al_2O_3/(CaO+Na_2O+K_2O)$ plot. C. $Na_2O$ + $K_2O$-CaO vs. $SiO_2$ (wt. %) plot. D. Normative classification of granitic rocks based on Ab-An-Or ternary diagram (after Barker, 1979). E. AFM diagram distinguishing calc-alkaline and tholeiitic series (after Irvine and Baragar, 1971). F. Sr vs Y (ppm) diagram (HP, MP, LP TTG fields are from Ge and others, 2018). G. Nb vs. Ta (ppm) diagram (HP, MP, LP TTG fields are from Ge and others, 2018). H. Nb vs.Y discrimination diagram (after Pearce and others, 1984). I. Rb vs. (Y+Nb) discrimination diagram (after Pearce and others, 1984).

TABLE 2

*Whole-rock trace and rare earth element data for TTG, granite and amphibolite samples*

| Sl No. | IK-1 | IK-112 | IK-3 | IK-6 | IK-8 | IK-9 | IK-10 | IK-21 | IK-2 | IK-4 | IK-5 | IK-7 |
|---|---|---|---|---|---|---|---|---|---|---|---|---|
| Li | 53.4 | 65.4 | 174.1 | 103.4 | 22.2 | 36.3 | 48.6 | 51.2 | 39.7 | 86.4 | 29.4 | 1.2 |
| B | 1.9 | 3.4 | 2.8 | 0.6 | 1.7 | 1.3 | 6.3 | 3.2 | 0.9 | 2.1 | 0.7 | 0.6 |
| Sc | 3.9 | 6.7 | 4.5 | 5.2 | 4.4 | 4.4 | 4.0 | 5.1 | 3.4 | 4.5 | 5.3 | 3.8 |
| V | 13.6 | 14.2 | 25.7 | 22.8 | 28.2 | 43.3 | 36.9 | 9.9 | 7.8 | 12.9 | 13.1 | 8.7 |
| Cr | 4.0 | 4.0 | 4.3 | 8.4 | 5.1 | 7.5 | 8.9 | 3.9 | 1.5 | 4.0 | 4.9 | 4.5 |
| Co | 2.3 | 3.1 | 5.2 | 4.9 | 4.6 | 7.8 | 6.6 | 2.6 | 1.2 | 1.5 | 2.1 | 1.5 |
| Zn | 76.7 | 39.4 | 47.7 | 40.2 | 19.7 | 55.3 | 62.8 | 38.0 | 16.0 | 31.0 | 32.6 | 2.5 |
| Ga | 18.5 | 20.0 | 18.7 | 18.4 | 18.7 | 19.6 | 20.0 | 18.5 | 20.0 | 19.9 | 18.3 | 14.2 |
| Ge | 0.427 | 0.432 | 0.327 | 0.284 | 0.404 | 0.367 | 0.372 | 0.474 | 0.687 | 0.681 | 0.360 | 0.520 |
| Cd | 0.033 | 0.081 | 0.038 | 0.019 | 0.046 | 0.027 | 0.022 | 0.038 | 0.033 | 0.041 | 0.035 | 0.032 |
| Cs | 3.028 | 3.735 | 8.317 | 2.914 | 3.370 | 1.872 | 7.807 | 2.073 | 8.924 | 9.214 | 2.667 | 0.415 |
| Ni | 2 | 0 | 7 | 3 | 2 | 0 | 1 | 0 | 8 | 9 | 18 | 0 |
| Rb | 81 | 88 | 95 | 73 | 71 | 54 | 61 | 42 | 303 | 257 | 171 | 107 |
| Ba | 113 | 116 | 135 | 128 | 283 | 141 | 130 | 139 | 229 | 283 | 220 | 389 |
| Th | 5.412 | 5.306 | 2.480 | 3.779 | 7.553 | 5.189 | 6.666 | 3.758 | 10.797 | 14.579 | 17.423 | 13.374 |
| U | 1.310 | 1.206 | 1.420 | 0.430 | 1.792 | 1.434 | 0.700 | 0.500 | 2.926 | 4.067 | 3.350 | 2.612 |
| Ta | 0.994 | 0.984 | 0.577 | 0.181 | 0.082 | 0.225 | 0.148 | 0.111 | 2.674 | 2.065 | 0.824 | 0.297 |
| Nb | 10.304 | 11.669 | 3.848 | 2.586 | 2.201 | 3.644 | 2.828 | 3.181 | 15.622 | 18.561 | 12.198 | 7.087 |
| Sr | 413 | 409 | 426 | 530 | 298 | 503 | 467 | 464 | 89 | 99 | 123 | 195 |
| P | 213 | 235 | 409 | 348 | 286 | 490 | 474 | 170 | 52 | 122 | 96 | 166 |
| Hf | 2.860 | 3.059 | 2.382 | 3.027 | 3.133 | 3.062 | 3.340 | 2.010 | 1.114 | 3.549 | 3.923 | 4.315 |
| Zr | 128 | 134 | 113 | 136 | 123 | 151 | 165 | 92 | 36 | 120 | 129 | 160 |
| Y | 19.119 | 16.884 | 8.736 | 3.891 | 4.787 | 6.377 | 5.214 | 4.601 | 30.977 | 55.010 | 136.355 | 40.853 |
| Pb | 13 | 15 | 8 | 9 | 11 | 9 | 10 | 12 | 24 | 23 | 23 | 23 |
| W | 2.043 | 12.537 | 2.346 | 2.437 | 4.149 | 4.971 | 4.329 | 8.894 | 7.509 | 2.714 | 3.774 | 11.656 |
| La | 15.893 | 15.942 | 12.376 | 22.670 | 20.678 | 23.104 | 25.485 | 15.673 | 12.162 | 32.788 | 19.834 | 42.271 |
| Ce | 29.651 | 31.125 | 21.702 | 41.494 | 38.794 | 44.137 | 45.698 | 26.742 | 22.972 | 64.783 | 39.279 | 73.288 |
| Pr | 3.654 | 3.584 | 2.427 | 4.626 | 4.545 | 4.906 | 4.928 | 2.882 | 2.762 | 7.587 | 4.740 | 8.631 |
| Nd | 12.884 | 12.808 | 8.104 | 15.968 | 16.026 | 16.787 | 16.668 | 9.682 | 10.176 | 25.712 | 16.693 | 30.114 |
| Sm | 2.755 | 2.641 | 1.366 | 2.284 | 2.791 | 2.572 | 2.514 | 1.601 | 2.635 | 5.777 | 4.612 | 5.961 |
| Eu | 0.454 | 0.543 | 0.474 | 0.557 | 0.606 | 0.727 | 0.694 | 0.385 | 0.418 | 0.571 | 0.586 | 0.670 |
| Gd | 2.537 | 2.515 | 1.299 | 1.435 | 2.056 | 1.876 | 1.693 | 1.192 | 3.237 | 5.747 | 8.932 | 6.178 |
| Tb | 0.462 | 0.385 | 0.161 | 0.144 | 0.230 | 0.229 | 0.185 | 0.149 | 0.659 | 1.179 | 2.141 | 1.030 |
| Dy | 2.924 | 2.154 | 0.960 | 0.633 | 1.022 | 1.074 | 0.801 | 0.723 | 4.633 | 7.768 | 17.392 | 6.210 |
| Ho | 0.631 | 0.458 | 0.193 | 0.097 | 0.137 | 0.183 | 0.149 | 0.127 | 1.020 | 1.693 | 4.220 | 1.274 |
| Er | 1.837 | 1.328 | 0.568 | 0.258 | 0.337 | 0.501 | 0.358 | 0.278 | 3.408 | 5.469 | 13.478 | 3.930 |
| Tm | 0.288 | 0.181 | 0.080 | 0.046 | 0.046 | 0.072 | 0.051 | 0.035 | 0.498 | 0.850 | 1.960 | 0.530 |
| Yb | 1.861 | 1.176 | 0.423 | 0.248 | 0.328 | 0.449 | 0.404 | 0.220 | 3.580 | 5.654 | 11.096 | 3.515 |
| Lu | 0.286 | 0.191 | 0.068 | 0.036 | 0.053 | 0.063 | 0.046 | 0.040 | 0.557 | 0.872 | 1.596 | 0.539 |
| Total REE | 76.12 | 75.03 | 50.20 | 90.50 | 87.65 | 96.68 | 99.68 | 59.73 | 68.72 | 166.45 | 146.56 | 184.14 |
| Sr/Y | 21.61 | 24.24 | 48.74 | 136.11 | 62.34 | 78.82 | 89.56 | 100.93 | 2.88 | 1.79 | 0.91 | 4.77 |
| Nb/Ta | 10.37 | 11.85 | 6.67 | 14.25 | 26.76 | 16.21 | 19.10 | 28.75 | 5.84 | 8.99 | 14.81 | 23.84 |
| Zr/Sm | 46.47 | 50.57 | 82.39 | 59.40 | 44.00 | 58.59 | 65.62 | 57.50 | 13.63 | 20.74 | 28.00 | 26.79 |
| Th/Nb | 0.53 | 0.45 | 0.64 | 1.46 | 3.43 | 1.42 | 2.36 | 1.18 | 0.69 | 0.79 | 1.43 | 1.89 |
| Eu/Eu* | 0.53 | 0.64 | 1.09 | 0.94 | 0.77 | 1.01 | 1.03 | 0.85 | 0.44 | 0.30 | 0.28 | 0.34 |
| $(Gd/Yb)_N$ | 1.13 | 1.77 | 2.54 | 4.78 | 5.19 | 3.45 | 3.47 | 4.49 | 0.75 | 0.84 | 0.67 | 1.45 |
| $(La/Yb)_N$ | 6.13 | 9.73 | 21.01 | 65.56 | 45.28 | 36.89 | 45.31 | 51.17 | 2.44 | 4.16 | 1.28 | 8.63 |

F, G; tables 1, 2). The granite samples (IK-2, IK-4, IK-5, IK-7 and IK-113) have high Nb and Y, and are also characterised by high Rb, $SiO_2$, $K_2O$ (> 4.0 wt.%) and low Sr, V, $TiO_2$, $Al_2O_3$, FeO, MgO, CaO and $Na_2O$ (< 4.2 wt.%) contents (figs. 3A, B, C, F, G; tables 1, 2). The TTG-I and TTG-II samples are magnesian, peraluminous and calcic to calc-alkalic, whereas the granites are ferroan, peraluminous and calc-alkalic to alkali-calcic (figs. 3A, B, C). Classification based on normative Ab-An-Or (Barker, 1979)

Table 2
*(continued)*

| Sl No. | IK113 | IK-15 | IK-16 | IK-17 | IK-18 | IK-19 | IK-13 | IK-14 | IK-11 | IK-12 | IK-20 |
|---|---|---|---|---|---|---|---|---|---|---|---|
| Li | 95.1 | 10.7 | 7.1 | 5.4 | 7.3 | 8.7 | 65.9 | 14.4 | 27.5 | 37.3 | 17.3 |
| B | 7.6 | 2.3 | 1.5 | 2.6 | 0.7 | 1.2 | 10.3 | 3.8 | 2.8 | 1.5 | 0.2 |
| Sc | 8.9 | 41.5 | 42.9 | 37.9 | 49.0 | 43.0 | 23.4 | 30.1 | 30.4 | 44.1 | 26.5 |
| V | 16.5 | 298.7 | 344.4 | 362.5 | 282.6 | 309.0 | 285.0 | 307.2 | 231.3 | 210.2 | 191.2 |
| Cr | 3.9 | 99.8 | 220.7 | 39.9 | 34.5 | 19.6 | 68.0 | 55.7 | 261.9 | 382.5 | 908.6 |
| Co | 3.3 | 62.9 | 51.8 | 43.9 | 47.6 | 54.0 | 55.1 | 52.5 | 48.7 | 43.4 | 49.8 |
| Zn | 43.8 | 113.4 | 89.5 | 133.9 | 80.2 | 99.4 | 125.2 | 138.6 | 83.7 | 60.7 | 70.8 |
| Ga | 19.5 | 16.4 | 17.4 | 17.3 | 15.8 | 16.6 | 23.0 | 19.8 | 13.4 | 13.2 | 10.0 |
| Ge | 0.865 | 1.474 | 1.430 | 1.683 | 1.564 | 1.825 | 1.362 | 1.691 | 1.152 | 1.215 | 1.406 |
| Cd | 0.106 | 0.093 | 0.086 | 0.112 | 0.115 | 0.129 | 0.079 | 0.173 | 0.053 | 0.106 | 0.048 |
| Cs | 10.581 | 0.578 | 0.131 | 0.098 | 0.142 | 0.564 | 4.475 | 0.468 | 1.167 | 1.478 | 2.707 |
| Ni | 7 | 73 | 94 | 45 | 64 | 40 | 101 | 50 | 167 | 158 | 264 |
| Rb | 241 | 11 | 8 | 6 | 19 | 14 | 75 | 33 | 19 | 12 | 19 |
| Ba | 537 | 39 | 36 | 21 | 114 | 165 | 171 | 192 | 5 | 10 | 16 |
| Th | 14.606 | 0.839 | 0.758 | 1.483 | 2.530 | 1.097 | 2.183 | 2.558 | 0.171 | 0.101 | 1.860 |
| U | 2.340 | 0.243 | 0.157 | 0.303 | 0.424 | 0.199 | 0.391 | 0.658 | 0.264 | 0.132 | 0.701 |
| Ta | 1.475 | 0.234 | 0.374 | 0.412 | 0.231 | 0.351 | 0.587 | 0.724 | 0.107 | 0.049 | 0.282 |
| Nb | 14.402 | 4.640 | 6.199 | 7.015 | 4.899 | 8.305 | 10.198 | 11.046 | 3.297 | 1.531 | 5.721 |
| Sr | 154 | 108 | 134 | 289 | 101 | 243 | 382 | 199 | 100 | 87 | 152 |
| P | 282 | 392 | 484 | 651 | 342 | 728 | 1062 | 5498 | 213 | 122 | 230 |
| Hf | 5.141 | 1.659 | 1.911 | 2.709 | 1.968 | 2.382 | 4.086 | 6.128 | 0.925 | 0.363 | 1.580 |
| Zr | 212 | 68 | 78 | 114 | 78 | 97 | 183 | 304 | 36 | 17 | 67 |
| Y | 43.766 | 23.864 | 24.908 | 36.471 | 29.148 | 26.638 | 28.522 | 57.890 | 16.507 | 14.787 | 17.244 |
| Pb | 23 | 2 | 1 | 4 | 4 | 2 | 2 | 5 | 3 | 5 | 2 |
| W | 18.021 | 14.011 | 5.747 | 8.230 | 6.903 | 11.182 | 5.093 | 7.857 | 4.971 | 3.710 | 2.429 |
| La | 60.776 | 4.994 | 5.640 | 9.038 | 9.058 | 11.728 | 20.318 | 29.838 | 1.973 | 0.907 | 7.638 |
| Ce | 117.470 | 12.515 | 13.998 | 22.138 | 18.603 | 27.094 | 45.091 | 69.058 | 5.461 | 2.237 | 18.052 |
| Pr | 12.680 | 1.821 | 2.073 | 3.181 | 2.297 | 3.624 | 5.868 | 9.543 | 0.878 | 0.331 | 2.375 |
| Nd | 42.051 | 8.562 | 10.099 | 14.971 | 9.431 | 15.858 | 24.446 | 41.431 | 4.524 | 1.597 | 10.120 |
| Sm | 7.335 | 2.545 | 2.933 | 4.147 | 2.486 | 3.974 | 5.405 | 9.055 | 1.491 | 0.512 | 2.583 |
| Eu | 0.948 | 0.882 | 1.071 | 1.344 | 0.805 | 1.314 | 1.669 | 2.780 | 0.512 | 0.249 | 1.061 |
| Gd | 6.497 | 3.392 | 3.791 | 5.260 | 3.509 | 4.296 | 5.505 | 10.350 | 2.207 | 1.018 | 2.844 |
| Tb | 1.040 | 0.634 | 0.661 | 0.907 | 0.653 | 0.677 | 0.883 | 1.660 | 0.401 | 0.219 | 0.478 |
| Dy | 6.192 | 4.100 | 4.230 | 6.150 | 4.559 | 4.388 | 5.020 | 10.164 | 2.536 | 1.802 | 2.882 |
| Ho | 1.319 | 0.872 | 0.879 | 1.252 | 0.992 | 0.880 | 0.925 | 2.089 | 0.565 | 0.470 | 0.586 |
| Er | 3.938 | 2.681 | 2.514 | 3.902 | 3.002 | 2.542 | 2.729 | 6.122 | 1.751 | 1.497 | 1.783 |
| Tm | 0.589 | 0.415 | 0.397 | 0.578 | 0.540 | 0.426 | 0.375 | 0.878 | 0.265 | 0.271 | 0.282 |
| Yb | 3.860 | 2.925 | 2.443 | 4.108 | 2.806 | 2.188 | 2.579 | 6.535 | 1.810 | 1.994 | 1.462 |
| Lu | 0.608 | 0.387 | 0.338 | 0.559 | 0.421 | 0.374 | 0.337 | 0.891 | 0.253 | 0.285 | 0.229 |
| Total REE | 265.30 | 46.72 | 51.07 | 77.54 | 59.16 | 79.36 | 121.15 | 200.39 | 24.63 | 13.39 | 52.37 |
| Sr/Y | 3.53 | 4.52 | 5.36 | 7.93 | 3.45 | 9.11 | 13.38 | 3.43 | 6.06 | 5.89 | 8.81 |
| Nb/Ta | 9.76 | 19.81 | 16.59 | 17.02 | 21.17 | 23.68 | 17.37 | 15.26 | 30.82 | 31.49 | 20.26 |
| Zr/Sm | 28.87 | 26.74 | 26.48 | 27.49 | 31.45 | 24.49 | 33.92 | 33.60 | 24.29 | 32.78 | 25.92 |
| Th/Nb | 1.01 | 0.18 | 0.12 | 0.21 | 0.52 | 0.13 | 0.21 | 0.23 | 0.05 | 0.07 | 0.33 |
| Eu/Eu* | 0.42 | 0.86 | 1.06 | 0.94 | 0.88 | 0.92 | 0.98 | 0.88 | 0.83 | 0.97 | 1.20 |
| $(Gd/Yb)_N$ | 1.39 | 0.96 | 1.28 | 1.06 | 1.03 | 1.62 | 1.77 | 1.31 | 1.01 | 0.42 | 1.61 |
| $(La/Yb)_N$ | 11.30 | 1.23 | 1.66 | 1.58 | 2.32 | 3.85 | 5.65 | 3.28 | 0.78 | 0.33 | 3.75 |

shows that the TTG samples are trondhjemitic (fig. 3D), whereas the AFM ($Na_2O+K_2O$, $FeO_{Total}$, MgO) discrimination diagram shows that all the TTG and granite samples have calc-alkaline affinities (Irvine and Baragar, 1971) (fig. 3E). The Sr vs. Y and Nb vs. Ta trace element diagrams indicate that TTG-II is a high- to medium-pressure TTG, TTG-I is a low-pressure TTG, and the granites are potassic (figs. 3F, G). On the Nb vs. Y and Rb vs. Nb+Y tectonic discrimination diagrams (Pearce

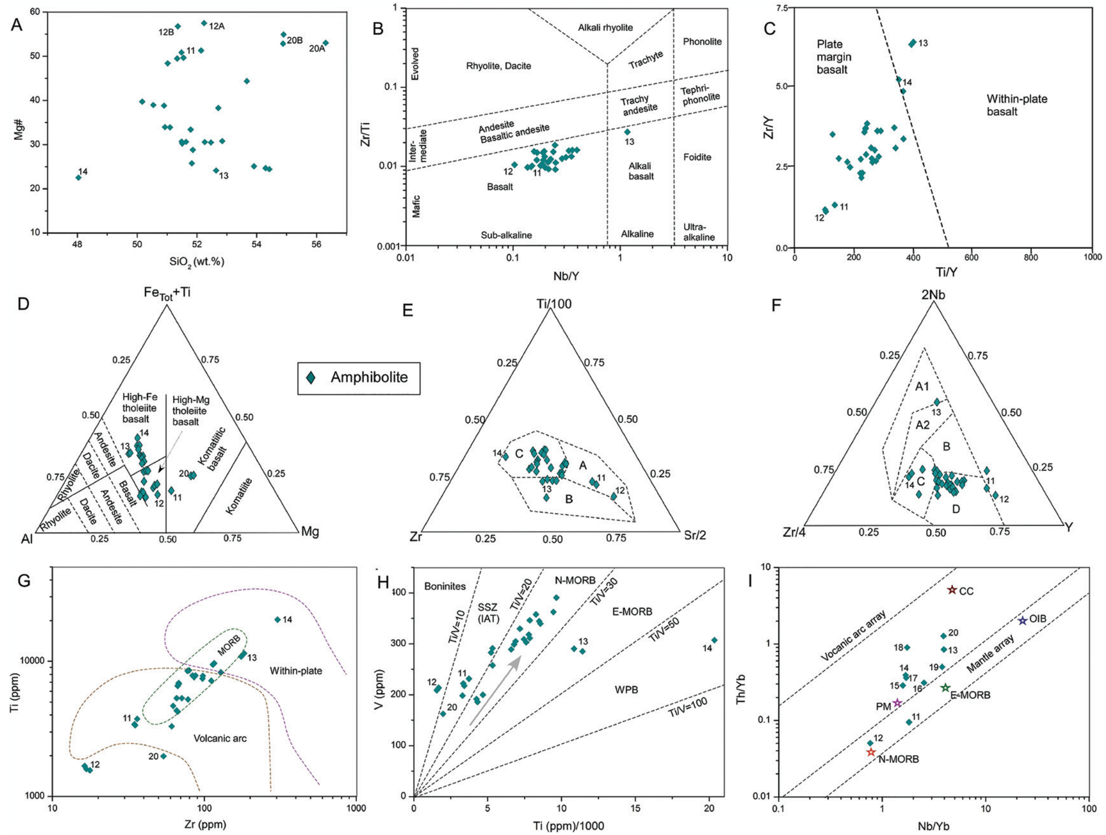


Fig. 4. Discrimination diagrams. A. Mg# vs. $SiO_2$ (wt. %) plot. B. Zr/Ti vs. Nb/Y discrimination diagram of volcanic rocks (after Winchester and Floyd, 1977; modified by Pearce, 1996). C. Zr/Y vs. Ti/Y diagram discriminating plate-margin basalts and within-plate basalts (after Pearce and Gale, 1977). D. Classification of mafic rocks according to Al, Fe+Ti, Mg cation percentages showing tholeiite, calc-alkaline and komatiite fields (after Rickwood, 1989). E. Ti-Zr-Sr discrimination diagram for basalts (after Pearce and Cann, 1973). A-Island-arc tholeiites; B-Calc-alkaline basalts; C-Mid-Ocean Ridge Basalts (MORB). F. The Zr-Nb-Y diagram for basalts (after Meschede, 1986). A1-Within-plate alkali basalts; A2- Within-plate alkali basalts and within-plate alkali tholeiites; B-E-type MORB; C-Within-plate basalts and volcanic-arc basalts; D-N-type MORB and volcanic-arc basalts. G. Discrimination diagram for basalts based on Ti-Zr variations (after Pearce, 1982). H. V vs. Ti variation diagram for amphibolites (after Shervais, 1982). I. Th/Yb vs. Nb/Yb variation diagram (after Pearce, 2008). Values of various mantle reservoirs are from Sun and McDonough (1989).

and others, 1984) the TTG-I and TTG-II samples plot in the volcanic arc field, whereas the granite samples plot in the within-plate to volcanic arc fields (figs. 3H, I).

The amphibolite samples do not show any clear systematic variations in major element compositions (Appendix figs. A4, A5). Most samples (IK-15, IK-16, IK-17, IK-18 and IK-19) have relatively high FeO, $TiO_2$ and low $Al_2O_3$, MgO and CaO contents, and samples IK-13 and IK-14 are richer in $TiO_2$, FeO, Nb and Zr (fig. 4; Appendix figs. A4, A5; tables 1, 2). A few samples (IK-11, IK-12, IK-20) have low FeO, $TiO_2$, Ba, Nb, Ta, Zr and Y, and high $Al_2O_3$, MgO, CaO, Cr and Ni contents (fig. 4; Appendix figs. A4, A5; tables 1, 2). On the Zr/Ti vs Nb/Y discrimination diagram for volcanic rocks (Winchester and Floyd, 1977; modified by Pearce, 1996) the amphibolites plot in the basalt field with a mafic and sub-alkaline composition (fig. 4B). The Zr/Y vs. Ti/Y diagram (Pearce and Gale, 1977) indicates that most of the amphibolites are comparable to plate margin basalts (fig. 4C). On the ternary diagram based on the cation percentages of Al, $Fe_{Tot}$+Ti and Mg (Rickwood, 1989) most of the amphibolite samples plot in the high Fe tholeiitic basalt field; a few plots in the komatiitic basalt field (fig. 4D). Several discrimination diagrams suggest a similar range of sources for the amphibolites. The Zr-Ti-Sr (Pearce and Cann, 1973) and Zr-Nb-Y (Meschede, 1986) ternary discrimination diagrams and the Ti vs Zr discrimination diagram of Pearce (1982) suggest that most of the amphibolites were derived from a source similar to that of MORB, with the exception of a few samples, that have either a within-plate (samples IK-13, IK-14) or volcanic arc (samples IK-11, IK-12, IK-20) signature (figs. 4C, E, F, G). The V vs. Ti diagram (Shervais, 1982) indicates that most of the amphibolites are similar to N-MORB, and a few are akin to island arc tholeiites that would be indicative of a supra-subduction zone origin (fig. 4H). On the Th/Yb vs. Nb/Yb diagram (Pearce, 2008) only two samples plot along the mantle array, whereas others plot from the primitive mantle (PM) to Archean continental crust (CC), in a trend indicating crustal contamination (fig. 4I). Accordingly, it may be surmised that a MORB-sourced magma underwent contamination by crustal assimilation during its evolution.

### *Rare Earth and Trace Element Patterns*

The TTG-I samples have negative Eu anomalies (Eu/Eu* ranges from 0.53 to 0.64) and slightly fractionated REE, with enriched LREE and flat HREE patterns (total REE ranges from 75.03 to 76.11 ppm) (fig. 5A; table 2). The TTG-II samples have no Eu anomaly and strongly fractionated REE patterns, with strong LREE enrichment, but no HREE enrichment (total REE ranges from 50.20 to 99.67 ppm) (fig. 5A). The granite samples have prominent negative Eu anomalies (Eu/Eu* ranges from 0.28 to 0.44) and no strong REE fractionation, with enrichments in both LREE and HREE (total REE ranges from 68.71 to 265.30 ppm) (fig. 5A). The amphibolite samples have flat REE patterns, but some samples (IK-13, IK-14) have higher total REE contents (fig. 5B), and samples (IK-11, IK-12, IK-20) have low total REE, and range from LREE-enriched to -depleted (in amphibolites $(Gd/Yb)_N$ varies from 0.42 to 1.76 and total REE ranges from 13.38 to 200.39 ppm) (fig. 5B; table 2).

The TTG-I samples have negative Ti and positive Sr anomalies, whereas the TTG-II samples have characteristic negative Nb and Ta, with positive Sr anomalies. The granite samples have negative Sr and Ti anomalies (fig. 5C; table 2). Some amphibolites (samples IK-11, IK-12, IK-20) have pronounced positive anomalies in incompatible and fluid-mobile elements (alkalis, Pb and Sr) (fig. 5D; table 2), probably an effect of late hydrothermal activity.

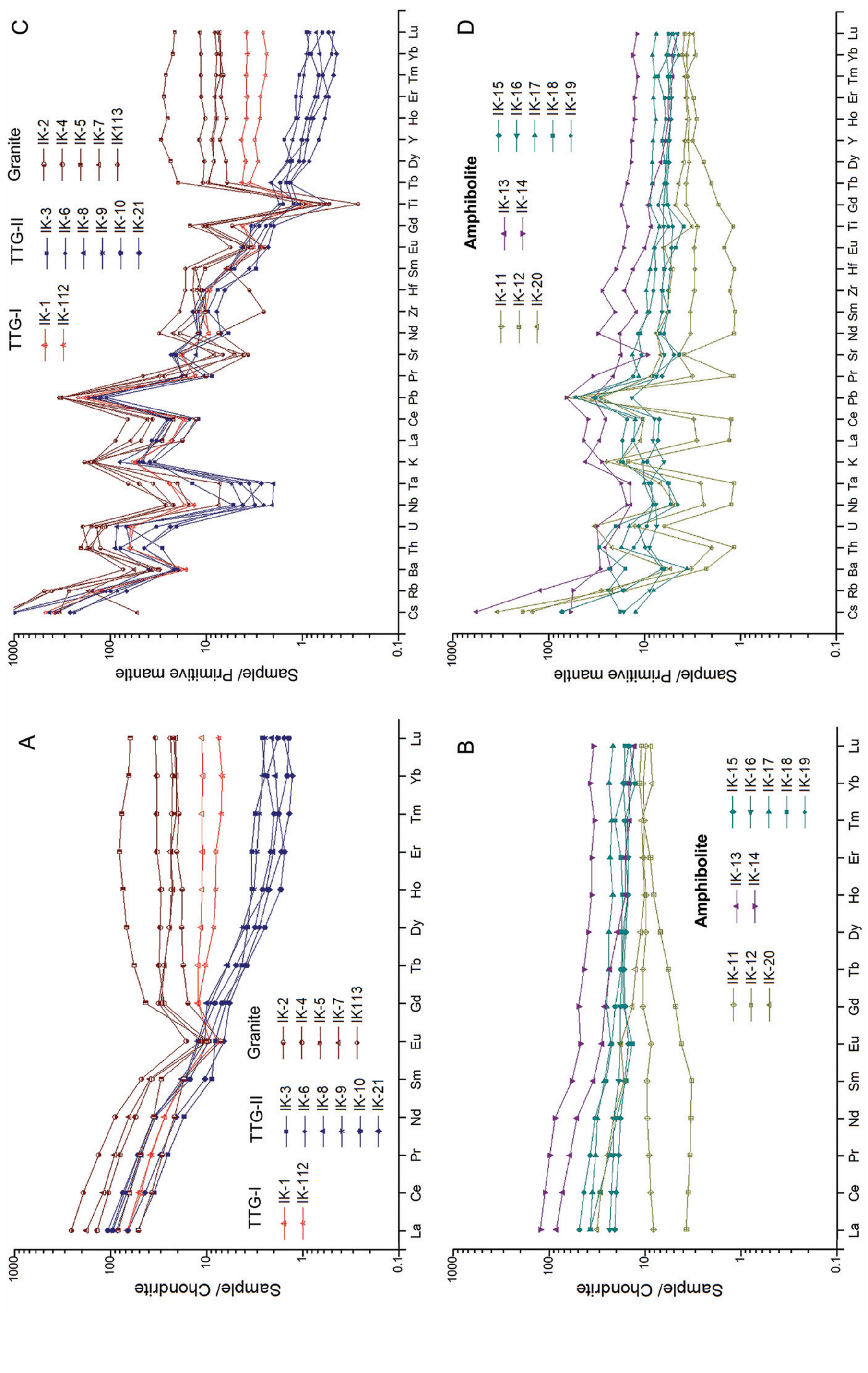


Fig. 5. Chondrite-normalised rare earth element plots: A. TTG and granite; B. Amphibolite. Primitive mantle-normalised trace element plots: C. TTG and granite; D. Amphibolite. (normalised after Sun and McDonough, 1989).

TABLE 3

*SHRIMP U-Pb zircon ages for IK-1 (TTG-I) and IK-2 (Granite) samples*

| Spot Name | U ppm | Th ppm | Pb* ppm | Th/U | % $^{206}Pb_c$ | $^{206}Pb^*/^{238}U$ | 1σ ±% | $^{207}Pb^*/^{235}U$ | 1σ ±% | $^{207}Pb^*/^{206}Pb$ | 1σ ±% | Date (Ma) 206/238 | ± 1σ | 207/235 | ± 1σ | 207/206 | ± 1σ | Error corrln |
|---|---|---|---|---|---|---|---|---|---|---|---|---|---|---|---|---|---|---|
| *a. IK-1 (TTG-I)* | | | | | | | | | | | | | | | | | | |
| 1.1 | 355 | 135 | 175 | 0.38 | 0.08 | 0.5727 | 1.5 | 19.70 | 1.5 | 0.2495 | 0.2 | 2917 | 36 | 3077 | 15 | 3177 | 4 | 0.99 |
| 2.1 | 103 | 38 | 53 | 0.37 | 0.00 | 0.5979 | 1.7 | 20.71 | 1.7 | 0.2512 | 0.4 | 3022 | 40 | 3125 | 16 | 3194 | 6 | 0.98 |
| 3.1 | 366 | 136 | 116 | 0.37 | 1.23 | 0.3690 | 1.5 | 12.08 | 1.5 | 0.2375 | 0.3 | 2003 | 26 | 2611 | 14 | 3038 | 12 | 0.90 |
| 4.1 | 97 | 31 | 54 | 0.32 | 0.00 | 0.6516 | 1.7 | 22.67 | 1.7 | 0.2523 | 0.4 | 3235 | 42 | 3213 | 16 | 3200 | 6 | 0.98 |
| 5.1 | 225 | 60 | 97 | 0.27 | 0.39 | 0.5026 | 1.6 | 17.42 | 1.6 | 0.2513 | 0.5 | 3070 | 37 | 2958 | 16 | 3170 | 3 | 0.95 |
| 6.1 | 255 | 66 | 142 | 0.26 | 0.04 | 0.6490 | 1.6 | 22.67 | 1.6 | 0.2534 | 0.3 | 3201 | 40 | 3213 | 15 | 3215 | 6 | 0.98 |
| 7.1 | 404 | 133 | 212 | 0.33 | 0.09 | 0.6105 | 1.5 | 20.92 | 1.5 | 0.2485 | 0.2 | 3139 | 40 | 3135 | 15 | 3187 | 6 | 0.99 |
| 8.1 | 154 | 100 | 85 | 0.65 | 0.00 | 0.6430 | 1.6 | 22.59 | 1.6 | 0.2548 | 0.4 | 2617 | 34 | 3209 | 16 | 3173 | 8 | 0.97 |
| 9.1 | 154 | 95 | 83 | 0.62 | 0.07 | 0.6278 | 1.6 | 21.72 | 1.6 | 0.2509 | 0.4 | 3044 | 39 | 3171 | 16 | 3176 | 7 | 0.97 |
| 10.1 | 164 | 102 | 85 | 0.62 | 0.12 | 0.6044 | 1.6 | 20.80 | 1.6 | 0.2496 | 0.4 | 3223 | 40 | 3129 | 16 | 3204 | 5 | 0.97 |
| 11.1 | 108 | 47 | 58 | 0.44 | 0.35 | 0.6265 | 1.6 | 21.53 | 1.7 | 0.2492 | 0.3 | 3127 | 41 | 3163 | 16 | 3160 | 7 | 0.96 |
| 12.1 | 309 | 210 | 186 | 0.68 | 0.11 | 0.7034 | 1.8 | 25.29 | 2.0 | 0.2608 | 0.8 | 3431 | 48 | 3320 | 19 | 3246 | 13 | 0.91 |
| 13.1 | 276 | 12 | 143 | 0.04 | 0.05 | 0.6030 | 1.6 | 20.73 | 1.6 | 0.2494 | 0.4 | 3041 | 38 | 3126 | 16 | 3178 | 7 | 0.96 |
| *b. IK-2 (Granite)* | | | | | | | | | | | | | | | | | | |
| 1.1 | 956 | 190 | 321 | 0.20 | 0.08 | 0.391 | 1.6 | 10.70 | 1.7 | 0.198 | 0.6 | 2129 | 29 | 2497 | 16 | 2812 | 10 | 0.93 |
| 1.2 | 1023 | 157 | 274 | 0.15 | 0.21 | 0.311 | 1.6 | 7.86 | 1.7 | 0.183 | 0.7 | 1748 | 24 | 2215 | 15 | 2681 | 12 | 0.90 |
| 3.1 | 1418 | 1483 | 438 | 1.05 | 7.62 | 0.360 | 1.2 | 9.59 | 4.7 | 0.193 | 4.5 | 1982 | 21 | 2396 | 42 | 2769 | 74 | 0.26 |
| 4.1 | 1268 | 124 | 284 | 0.10 | 0.34 | 0.260 | 1.5 | 5.65 | 1.9 | 0.157 | 1.1 | 1492 | 20 | 1923 | 16 | 2426 | 19 | 0.80 |
| 5.1 | 1811 | 1055 | 250 | 0.58 | 4.03 | 0.160 | 1.5 | 2.67 | 5.1 | 0.121 | 4.9 | 959 | 13 | 1320 | 37 | 1965 | 88 | 0.28 |
| 5.2 | 2155 | 1196 | 270 | 0.56 | 7.37 | 0.146 | 1.3 | 2.45 | 4.0 | 0.122 | 3.7 | 878 | 11 | 1256 | 28 | 1980 | 66 | 0.34 |
| 6.1 | 1751 | 1331 | 295 | 0.76 | 0.28 | 0.196 | 1.3 | 3.29 | 1.9 | 0.122 | 1.3 | 1153 | 14 | 1479 | 14 | 1984 | 23 | 0.72 |
| 7.1 | 2036 | 601 | 371 | 0.30 | 0.67 | 0.212 | 1.3 | 4.16 | 1.7 | 0.142 | 1.1 | 1240 | 14 | 1666 | 14 | 2253 | 19 | 0.76 |
| 7.2 | 2370 | 2565 | 291 | 1.08 | 0.83 | 0.143 | 1.2 | 1.91 | 2.3 | 0.097 | | 862 | 10 | 1085 | 15 | 1564 | 36 | 0.54 |
| 9.1 | 1514 | 72 | 295 | 0.05 | 0.26 | 0.227 | 1.6 | 4.86 | 1.9 | 0.155 | 1.1 | 1318 | 19 | 1795 | 16 | 2405 | 19 | 0.82 |
| 10.1 | 2515 | 1114 | 421 | 0.44 | 3.49 | 0.195 | 1.5 | 3.20 | 5.4 | 0.119 | 5.2 | 1147 | 16 | 1457 | 41 | 1945 | 93 | 0.28 |
| 11.1 | 2812 | 375 | 374 | 0.13 | 4.53 | 0.155 | 1.3 | 2.88 | 3.1 | 0.135 | 2.9 | 929 | 11 | 1376 | 23 | 2159 | 50 | 0.40 |
| 12.1 | 1638 | 1113 | 268 | 0.68 | 0.64 | 0.190 | 1.3 | 3.16 | 2.1 | 0.121 | 1.7 | 1124 | 14 | 1448 | 16 | 1964 | 30 | 0.63 |
| 13.1 | 2829 | 1760 | 540 | 0.62 | 0.69 | 0.222 | 1.2 | 4.31 | 1.8 | 0.141 | 1.3 | 1293 | 14 | 1695 | 14 | 2237 | 22 | 0.70 |
| 14.1 | 1161 | 109 | 251 | 0.09 | 0.42 | 0.251 | 1.8 | 5.77 | 2.1 | 0.166 | 1.1 | 1446 | 24 | 1942 | 18 | 2523 | 18 | 0.86 |
| 15.1 | 1880 | 797 | 338 | 0.42 | 0.28 | 0.209 | 2.4 | 4.18 | 2.5 | 0.145 | 0.6 | 1224 | 27 | 1669 | 20 | 2286 | 10 | 0.97 |
| 16.1 | 1908 | 1226 | 269 | 0.64 | 0.59 | 0.164 | 1.6 | 2.65 | 2.6 | 0.117 | 2.0 | 981 | 15 | 1314 | 19 | 1908 | 37 | 0.62 |

TABLE 3

*(continued)*

| Spot Name | U ppm | Th ppm | Pb* ppm | Th/U | % $^{206}Pb_c$ | $^{206}Pb^*/^{238}U$ | 1σ ±% | $^{207}Pb^*/^{235}U$ | 1σ ±% | $^{207}Pb^*/^{206}Pb$ | 1σ ±% | Date (Ma) 206/238 | ± 1σ | 207/235 | ± 1σ | 207/206 | ± 1σ | Error corrln |
|---|---|---|---|---|---|---|---|---|---|---|---|---|---|---|---|---|---|---|
| *b. IK-2 (Granite)* | | | | | | | | | | | | | | | | | | |
| 17.1 | 2429 | 1482 | 357 | 0.61 | 3.51 | 0.171 | 1.6 | 2.51 | 4.4 | 0.106 | 4.1 | 1019 | 15 | 1274 | 31 | 1734 | 75 | 0.37 |
| 18.1 | 1159 | 391 | 274 | 0.34 | 0.16 | 0.276 | 1.9 | 6.40 | 2.1 | 0.168 | 0.9 | 1570 | 26 | 2032 | 18 | 2541 | 16 | 0.89 |
| 19.1 | 2861 | 2579 | 389 | 0.90 | 2.06 | 0.158 | 1.4 | 2.89 | 2.7 | 0.133 | 2.3 | 946 | 13 | 1379 | 20 | 2132 | 40 | 0.54 |
| 20.1 | 2155 | 1837 | 481 | 0.85 | 2.70 | 0.260 | 1.6 | 5.41 | 3.1 | 0.151 | 2.6 | 1490 | 21 | 1886 | 26 | 2355 | 45 | 0.52 |
| 21.1 | 1978 | 1145 | 328 | 0.58 | 3.34 | 0.193 | 1.8 | 3.01 | 4.7 | 0.113 | 4.4 | 1137 | 19 | 1411 | 36 | 1854 | 80 | 0.38 |
| 22.1 | 2577 | 2131 | 377 | 0.83 | 1.40 | 0.170 | 1.5 | 2.93 | 2.4 | 0.125 | 1.9 | 1014 | 14 | 1390 | 18 | 2026 | 34 | 0.61 |
| 23.1 | 1064 | 79 | 247 | 0.07 | 0.27 | 0.271 | 2.0 | 6.26 | 2.2 | 0.168 | 1.0 | 1545 | 27 | 2012 | 19 | 2533 | 17 | 0.90 |
| 24.1 | 2649 | 2220 | 534 | 0.84 | 0.15 | 0.234 | 1.4 | 4.89 | 1.6 | 0.151 | 0.7 | 1358 | 17 | 1801 | 13 | 2362 | 12 | 0.90 |
| 25.1 | 1400 | 191 | 321 | 0.14 | 1.44 | 0.267 | 2.0 | 5.74 | 3.0 | 0.156 | 2.3 | 1524 | 27 | 1938 | 26 | 2415 | 39 | 0.66 |
| 27.1 | 3593 | 1997 | 449 | 0.56 | 3.77 | 0.146 | 1.4 | 2.58 | 3.5 | 0.128 | 3.2 | 876 | 11 | 1294 | 25 | 2075 | 57 | 0.40 |
| 28.1 | 2356 | 2080 | 411 | 0.88 | 0.58 | 0.203 | 1.5 | 3.87 | 2.3 | 0.138 | 1.7 | 1191 | 16 | 1607 | 18 | 2204 | 29 | 0.67 |
| 29.1 | 1414 | 772 | 240 | 0.55 | 0.54 | 0.198 | 1.9 | 3.11 | 3.0 | 0.114 | 2.4 | 1164 | 20 | 1435 | 23 | 1864 | 42 | 0.63 |
| 31.1 | 1250 | 696 | 440 | 0.56 | 0.97 | 0.410 | 1.9 | 11.17 | 2.2 | 0.198 | 1.1 | 2216 | 35 | 2538 | 20 | 2806 | 19 | 0.85 |
| 31.2 | 1995 | 2370 | 525 | 1.19 | 1.99 | 0.307 | 1.6 | 7.75 | 2.1 | 0.183 | 1.4 | 1724 | 24 | 2202 | 19 | 2683 | 23 | 0.75 |
| 32.1 | 2339 | 1570 | 360 | 0.67 | 0.99 | 0.179 | 1.5 | 3.52 | 2.2 | 0.143 | 1.5 | 1062 | 15 | 1532 | 17 | 2260 | 26 | 0.72 |
| 33.1 | 1667 | 1649 | 301 | 0.99 | 1.32 | 0.210 | 1.7 | 4.10 | 2.9 | 0.142 | 2.3 | 1230 | 19 | 1655 | 23 | 2246 | 39 | 0.61 |
| 34.1 | 2304 | 1778 | 440 | 0.77 | 0.94 | 0.222 | 1.6 | 4.46 | 2.1 | 0.145 | 1.4 | 1295 | 19 | 1723 | 18 | 2291 | 24 | 0.75 |
| 35.1 | 2185 | 1816 | 322 | 0.83 | 0.24 | 0.172 | 1.5 | 2.55 | 1.9 | 0.108 | 1.2 | 1021 | 15 | 1287 | 14 | 1762 | 21 | 0.80 |
| 37.1 | 1011 | 490 | 267 | 0.49 | 1.45 | 0.308 | 2.5 | 7.52 | 4.6 | 0.177 | 3.9 | 1731 | 37 | 2175 | 41 | 2625 | 65 | 0.53 |
| 38.1 | 1655 | 1189 | 249 | 0.72 | 3.54 | 0.175 | 2.0 | 3.14 | 7.3 | 0.130 | 7.1 | 1039 | 19 | 1442 | 55 | 2100 | 124 | 0.27 |
| 39.1 | 2350 | 1947 | 410 | 0.83 | 2.42 | 0.203 | 7.5 | 3.44 | 12.0 | 0.123 | 9.4 | 1191 | 82 | 1513 | 90 | 1997 | 167 | 0.62 |
| 40.1 | 634 | 601 | 227 | 0.95 | 0.52 | 0.416 | 2.5 | 11.39 | 2.7 | 0.198 | 1.1 | 2244 | 47 | 2555 | 25 | 2813 | 19 | 0.91 |
| 41.1 | 1798 | 1146 | 272 | 0.64 | 2.98 | 0.176 | 1.8 | 2.92 | 4.2 | 0.120 | 3.8 | 1046 | 17 | 1387 | 31 | 1960 | 67 | 0.43 |
| 42.1 | 2949 | 2268 | 736 | 0.77 | 1.18 | 0.290 | 1.5 | 6.98 | 1.9 | 0.174 | 1.2 | 1644 | 22 | 2109 | 17 | 2599 | 21 | 0.77 |
| 44.1 | 2528 | 791 | 502 | 0.31 | 0.74 | 0.231 | 1.5 | 4.87 | 1.9 | 0.153 | 1.1 | 1341 | 19 | 1797 | 16 | 2376 | 18 | 0.83 |
| 45.1 | 1444 | 763 | 304 | 0.53 | 1.18 | 0.245 | 2.0 | 4.98 | 2.5 | 0.147 | 1.6 | 1414 | 25 | 1817 | 21 | 2315 | 27 | 0.77 |
| 46.1 | 2648 | 3116 | 485 | 1.18 | 0.30 | 0.213 | 1.6 | 3.85 | 1.9 | 0.131 | 1.0 | 1246 | 18 | 1604 | 15 | 2113 | 18 | 0.84 |
| 47.1 | 1950 | 1044 | 411 | 0.54 | 1.48 | 0.245 | 1.7 | 5.33 | 2.4 | 0.158 | 1.7 | 1414 | 21 | 1873 | 20 | 2430 | 29 | 0.70 |
| 48.1 | 1624 | 105 | 246 | 0.06 | 0.70 | 0.176 | 1.8 | 2.99 | 2.9 | 0.123 | 2.3 | 1047 | 17 | 1404 | 22 | 1997 | 40 | 0.62 |
| 49.1 | 1986 | 399 | 335 | 0.20 | 2.31 | 0.196 | 1.8 | 3.75 | 3.1 | 0.138 | 2.6 | 1156 | 19 | 1582 | 25 | 2207 | 45 | 0.56 |
| 49.2 | 1164 | 922 | 232 | 0.79 | 1.08 | 0.232 | 2.0 | 4.79 | 2.9 | 0.150 | 2.1 | 1347 | 25 | 1783 | 24 | 2341 | 36 | 0.69 |
| 50.1 | 1372 | 1422 | 261 | 1.04 | 0.53 | 0.222 | 1.9 | 4.15 | 2.2 | 0.135 | 1.3 | 1292 | 22 | 1663 | 18 | 2170 | 22 | 0.83 |

TABLE 3

*(continued)*

| Spot Name | U ppm | Th ppm | Pb* ppm | Th/U | % $^{206}Pb_c$ | $^{206}Pb^*/^{238}U$ | 1σ ±% | $^{207}Pb^*/^{235}U$ | 1σ ±% | $^{207}Pb^*/^{206}Pb$ | 1σ ±% | Date (Ma) 206/238 | ± 1σ | 207/235 | ± 1σ | 207/206 | ± 1σ | Error corrln |
|---|---|---|---|---|---|---|---|---|---|---|---|---|---|---|---|---|---|---|
| *b. IK-2 (Granite)* | | | | | | | | | | | | | | | | | | |
| 36.1 | 1772 | 1131 | 255 | 0.64 | 0.26 | 0.167 | 1.7 | 2.55 | 1.9 | 0.111 | 0.8 | 997 | 16 | 1287 | 14 | 1809 | 15 | 0.90 |
| 51.1 | 1405 | 978 | 258 | 0.70 | 0.48 | 0.213 | 1.8 | 4.14 | 2.2 | 0.141 | 1.3 | 1247 | 21 | 1662 | 18 | 2236 | 22 | 0.83 |
| 52.1 | 1142 | 98 | 305 | 0.09 | 0.58 | 0.310 | 2.0 | 7.66 | 2.4 | 0.179 | 1.3 | 1743 | 30 | 2192 | 21 | 2644 | 22 | 0.83 |
| 53.1 | 1657 | 1433 | 357 | 0.86 | 2.66 | 0.251 | 1.8 | 5.38 | 3.0 | 0.155 | 2.5 | 1444 | 23 | 1882 | 26 | 2407 | 42 | 0.58 |
| 54.1 | 4584 | 623 | 1456 | 0.14 | 0.71 | 0.370 | 1.2 | 10.14 | 1.3 | 0.199 | 0.5 | 2028 | 21 | 2448 | 12 | 2818 | 8 | 0.93 |
| 55.1 | 1109 | 225 | 246 | 0.20 | 0.40 | 0.258 | 2.0 | 5.73 | 2.5 | 0.161 | 1.5 | 1479 | 26 | 1936 | 22 | 2468 | 26 | 0.79 |
| 56.1 | 1645 | 743 | 263 | 0.45 | 6.07 | 0.186 | 1.8 | 2.93 | 5.8 | 0.114 | 5.5 | 1101 | 19 | 1391 | 43 | 1869 | 99 | 0.32 |
| 57.1 | 1390 | 318 | 283 | 0.23 | 1.27 | 0.237 | 1.8 | 4.75 | 2.7 | 0.145 | 2.0 | 1371 | 23 | 1776 | 23 | 2293 | 35 | 0.67 |
| 59.1 | 1046 | 278 | 239 | 0.27 | 0.26 | 0.266 | 2.0 | 6.19 | 2.2 | 0.169 | 1.0 | 1520 | 27 | 2003 | 19 | 2545 | 17 | 0.89 |
| 60.1 | 858 | 33 | 417 | 0.04 | 0.29 | 0.566 | 2.2 | 16.52 | 2.2 | 0.212 | 0.4 | 2892 | 51 | 2907 | 21 | 2918 | 7 | 0.98 |
| 61.1 | 1148 | 884 | 389 | 0.77 | 1.35 | 0.395 | 2.0 | 10.50 | 2.5 | 0.193 | 1.4 | 2145 | 37 | 2480 | 23 | 2768 | 22 | 0.83 |
| 62.1 | 1420 | 1208 | 454 | 0.85 | 1.84 | 0.372 | 1.8 | 10.23 | 2.3 | 0.200 | 1.3 | 2038 | 32 | 2456 | 21 | 2823 | 22 | 0.81 |
| 63.1 | 1469 | 953 | 237 | 0.65 | 0.63 | 0.188 | 1.8 | 2.97 | 2.4 | 0.115 | 1.5 | 1110 | 19 | 1401 | 18 | 1877 | 28 | 0.76 |
| 64.1 | 1866 | 598 | 344 | 0.32 | 2.16 | 0.215 | 1.7 | 3.93 | 2.8 | 0.133 | 2.2 | 1255 | 19 | 1620 | 22 | 2135 | 39 | 0.60 |
| 65.1 | 1800 | 1337 | 319 | 0.74 | 3.08 | 0.206 | 1.7 | 3.50 | 3.6 | 0.123 | 3.2 | 1209 | 19 | 1528 | 28 | 2002 | 57 | 0.47 |
| 66.1 | 1695 | 394 | 309 | 0.23 | 0.81 | 0.212 | 1.7 | 4.22 | 2.4 | 0.144 | 1.6 | 1241 | 20 | 1678 | 19 | 2279 | 27 | 0.74 |
| 67.1 | 1253 | 210 | 231 | 0.17 | 0.25 | 0.214 | 1.9 | 4.43 | 2.2 | 0.150 | 1.2 | 1252 | 21 | 1717 | 18 | 2343 | 20 | 0.85 |
| 68.1 | 294 | 86 | 81 | 0.29 | 0.42 | 0.322 | 3.8 | 8.30 | 4.1 | 0.187 | 1.7 | 1802 | 59 | 2265 | 37 | 2714 | 28 | 0.91 |
| 69.1 | 2029 | 1678 | 359 | 0.83 | 2.49 | 0.206 | 1.7 | 3.73 | 3.2 | 0.131 | 2.8 | 1207 | 18 | 1578 | 25 | 2118 | 48 | 0.51 |
| 70.1 | 1841 | 1318 | 367 | 0.72 | 0.67 | 0.232 | 1.7 | 4.65 | 2.2 | 0.145 | 1.5 | 1344 | 20 | 1758 | 19 | 2292 | 26 | 0.75 |
| 71.1 | 1167 | 95 | 241 | 0.08 | 0.50 | 0.241 | 1.9 | 5.23 | 2.3 | 0.158 | 1.2 | 1390 | 24 | 1858 | 19 | 2432 | 20 | 0.85 |
| 72.1 | 1521 | 1565 | 233 | 1.03 | 0.50 | 0.178 | 1.8 | 2.67 | 2.4 | 0.109 | 1.5 | 1058 | 18 | 1320 | 17 | 1776 | 28 | 0.77 |

Errors are 1-sigma; $Pb_c$ and $Pb^*$ indicate the common and radiogenic portions, respectively.
Error in Standard calibration was 0.54%.
Common Pb corrected using measured $^{204}Pb$.

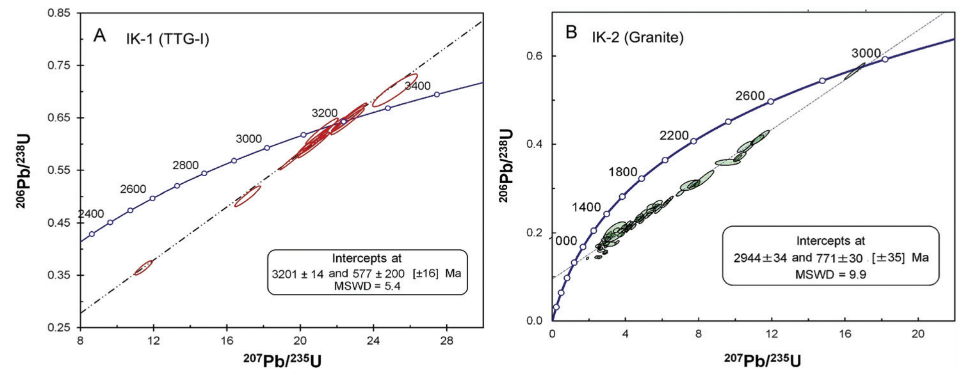


Fig. 6. A. Concordia plot (Wetherill) of zircons analyzed by U-Pb SHRIMP method from sample IK-1 (TTG-I); B. Concordia plot (Wetherill) of zircons analyzed by U-Pb SHRIMP method from sample IK-2 (granite).

### *SHRIMP U-Pb Zircon Geochronology*

Zircon grains from TTG-I (sample IK-1) are colorless to pale violet, mostly 50 to 100 μm in length and have a range of morphologies and internal structures. They are mostly elongate prisms with oscillatory zones and no evidence of metamorphic overgrowths (Appendix fig. A6A). One spot was dated in each of 13 zircons (table 3a); the analyses yield an upper intercept age of 3201 ± 14 Ma and a lower intercept age of 577 ± 200 Ma, with an MSWD of 5.4 (fig. 6A).

The zircon grains from granite (sample IK-2) are colorless to pale violet, mostly 50 to 200 μm in length and have a variety of morphologies and internal structures. The grains are mostly elongate prisms with oscillatory zones and no evidence of metamorphic overgrowths (Appendix fig. A6B). One spot was dated in each of 77 zircons, of which 72 were used for the age calculation (table 3b). The zircon analyses, most of which are strongly discordant, yield an upper intercept age of 2944 ± 34 Ma and a lower intercept age of 771 ± 30 Ma, with an MSWD of 9.9 (fig. 6B).

### *Whole-Rock Sr and Nd Isotopic Analyses*

Whole-rock Sr and Nd isotopic compositions were measured for two TTG-I, six TTG-II, five granite and ten amphibolite samples. The results are listed in table 4 and presented in figure 7A, B. The ratios of $^{87}Sr/^{86}Sr_{(i)}$ and $^{143}Nd/^{144}Nd_{(i)}$ were calculated using the ages of 3.2 Ga for TTG-I and TTG-II (Present study; Ishwar-Kumar and others, 2013,) and 2.94 Ga for the granites (Present study) and 3.0 Ga for the amphibolites (Ishwar-Kumar, ms, 2015; Li and others, 2020). The uncertainties of all measured ratios were < 0.000015. For TTG-I $^{87}Sr/^{86}Sr_{(i)}$ ranges from 0.70086 to 0.70089 and $^{143}Nd/^{144}Nd_{(i)}$ from 0.50840 to 0.50841. For TTG-II $^{87}Sr/^{86}Sr_{(i)}$ ranges from 0.70057 to 0.70184, $^{143}Nd/^{144}Nd_{(i)}$ ratios from 0.50842 to 0.50871, slightly higher than that of TTG-I. The granites have $^{87}Sr/^{86}Sr_{(i)}$ that ranges from 0.70593 to 0.75522 and $^{143}Nd/^{144}Nd_{(i)}$ from 0.50850 to 0.50881, which are higher than corresponding values for both TTG-I and TTG-II. For the amphibolites, $^{87}Sr/^{86}Sr_{(i)}$ ranges from 0.70116 to 0.70415 and $^{143}Nd/^{144}Nd_{(i)}$ from 0.50861 to 0.50889 (fig. 7A). The εNd(t) for TTG-I at 3.2 Ga is -1.4, whereas for TTG-II at 3.2 Ga εNd(t) ranges from -1.1 to 4.6. The granites have a more heterogeneous isotopic composition at 2.94 Ga, with εNd(t) ranging from -3.0 to -0.2. For the amphibolites at 3.0 Ga, εNd(t) ranges from -2.5 to 3.1 (figs. 7B, 8A). The $T_{DM_c}$ model ages for TTG-I ranges from 3359 to 3354 Ma, whereas for TTG-II from 3274 to 2809 Ma, for granites from 3558 to 2965 Ma and for amphibolites from 3954 to 2196 Ma.

TABLE 4

*Whole-rock Sr and Nd isotope results from TTG, granite and amphibolite samples*

| Sl No. | Rock type | $^{87}Sr/^{86}Sr$ | Sr(ppm) | Rb(ppm) | $^{87}Rb/^{86}Sr$ | $^{87}Sr/^{86}Sr_{(i)}$ | $^{143}Nd/^{144}Nd$ | Nd (ppm) | Sm(ppm) | $^{147}Sm/^{144}Nd$ | $^{143}Nd/^{144}Nd_{(i)}$ | $T_{DM}^{c}$ | ε Nd |
|---|---|---|---|---|---|---|---|---|---|---|---|---|---|
| IK-1 | TTG-I | 0.726364 | 413 | 81 | 0.548522 | 0.700864 | 0.511203 | 12.884 | 2.755 | 0.132017 | 0.508412 | 3359 | -1.4 |
| IK-112 | TTG-I | 0.728664 | 409 | 88 | 0.597404 | 0.700892 | 0.511101 | 12.808 | 2.641 | 0.127281 | 0.508409 | 3354 | -1.4 |
| IK-3 | TTG-II | 0.729950 | 426 | 95 | 0.625178 | 0.700886 | 0.510730 | 8.104 | 1.366 | 0.104040 | 0.508529 | 3121 | 1.0 |
| IK-6 | TTG-II | 0.718517 | 530 | 73 | 0.384717 | 0.700632 | 0.510294 | 15.968 | 2.284 | 0.088284 | 0.508427 | 3274 | -1.1 |
| IK-8 | TTG-II | 0.732923 | 298 | 71 | 0.668463 | 0.701847 | 0.510987 | 16.026 | 2.791 | 0.107529 | 0.508713 | 2809 | 4.6 |
| IK-9 | TTG-II | 0.714587 | 503 | 54 | 0.301398 | 0.700576 | 0.510581 | 16.787 | 2.572 | 0.094591 | 0.508580 | 3053 | 2.0 |
| IK-10 | TTG-II | 0.717794 | 467 | 61 | 0.364779 | 0.700836 | 0.510612 | 16.668 | 2.514 | 0.093097 | 0.508643 | 2964 | 3.2 |
| IK-21 | TTG-II | 0.713068 | 464 | 42 | 0.250142 | 0.701439 | 0.510710 | 9.682 | 1.601 | 0.102107 | 0.508550 | 3089 | 1.4 |
| IK-2 | Granite | 1.160243 | 89 | 303 | 9.500387 | 0.755225 | 0.511773 | 10.176 | 2.635 | 0.159872 | 0.508670 | 3558 | -3.0 |
| IK-4 | Granite | 1.039319 | 99 | 257 | 7.264574 | 0.729618 | 0.511439 | 25.712 | 5.777 | 0.138701 | 0.508747 | 3133 | -1.5 |
| IK-5 | Granite | 0.881594 | 123 | 171 | 3.866140 | 0.716774 | 0.511817 | 16.693 | 4.612 | 0.170551 | | | |
| IK-7 | Granite | 0.771381 | 195 | 107 | 1.535253 | 0.705931 | 0.511181 | 30.114 | 5.961 | 0.122205 | 0.508809 | 2965 | -0.2 |
| IK-113 | Granite | 0.903109 | 154 | 241 | 4.367167 | 0.716929 | 0.510853 | 42.051 | 7.335 | 0.107695 | 0.508762 | 3039 | -1.2 |
| IK-15 | Amphibolite | 0.711189 | 108 | 11 | 0.296518 | | 0.512398 | 8.562 | 2.545 | 0.183491 | 0.508763 | 2771 | 0.4 |
| IK-16 | Amphibolite | 0.706621 | 134 | 8 | 0.176516 | | 0.512719 | 10.099 | 2.933 | 0.179270 | | | |
| IK-17 | Amphibolite | 0.706263 | 289 | 6 | 0.054338 | 0.703898 | 0.512268 | 14.971 | 4.147 | 0.171020 | 0.508879 | 2196 | 2.7 |
| IK-18 | Amphibolite | 0.715509 | 101 | 19 | 0.539021 | | 0.511734 | 9.431 | 2.486 | 0.162764 | | | |
| IK-19 | Amphibolite | 0.706596 | 243 | 14 | 0.166140 | | 0.511853 | 15.858 | 3.974 | 0.154694 | 0.508788 | 2839 | 0.9 |
| IK-13 | Amphibolite | 0.724895 | 382 | 75 | 0.545334 | 0.701161 | 0.511481 | 24.446 | 5.405 | 0.136505 | 0.508776 | 2916 | 0.7 |
| IK-14 | Amphibolite | 0.721931 | 199 | 33 | 0.462550 | 0.701801 | 0.511573 | 41.431 | 9.055 | 0.134924 | 0.508899 | 2619 | 3.1 |
| IK-11 | Amphibolite | 0.726371 | 100 | 19 | 0.531601 | 0.703235 | 0.512819 | 4.524 | 1.491 | 0.203498 | 0.508787 | 3954 | 0.9 |
| IK-12 | Amphibolite | 0.712369 | 87 | 12 | 0.370388 | | 0.512942 | 1.597 | 0.512 | 0.197745 | | | |
| IK-20 | Amphibolite | 0.719184 | 152 | 19 | 0.345437 | 0.704150 | 0.511736 | 10.120 | 2.583 | 0.157568 | 0.508614 | 3494 | -2.5 |

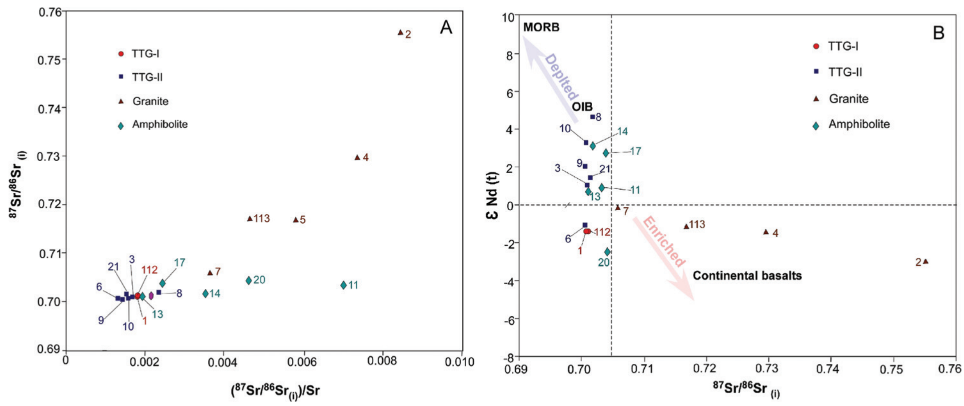


Fig. 7. A. $^{87}Sr/^{86}Sr(i)$ vs. $^{87}Sr/^{86}Sr(i)/Sr$ diagram for TTG, granite and amphibolite; B. εNd(t) vs. $^{87}Sr/^{86}Sr(i)$ plot for TTG, granite and amphibolite.

### *Zircon Lu-Hf Isotopic Analyses*

The zircon Lu-Hf isotopic results are presented in table 5. Fourteen sites on zircons from sample IK-1 (TTG-I) were analyzed for Lu-Hf isotopic composition. The εHf(t) value, calculated at *ca.* 3.2 Ga, ranges from 1.0 to 4.1 and the $T_{DM_c}$ model age from 3294 to 3476 Ma (fig. 8B).

### *Zircon Oxygen Isotope Analyses*

The U-Pb and oxygen isotopic compositions measured on zircons separated from samples IK-1 (TTG-I) and IK-2 (granite) are listed in Appendix table A5 and plotted in figure 8C. The zircon grains from sample IK-1 that are concordant or near-concordant have a relatively narrow range of $\delta^{18}O$, mostly 5.3 to 6.2 ‰ ($\delta^{18}O$ ranges from 4.0 to 6.5 ‰, with one exceptionally low value of 2.4 ‰). Several of the more discordant grains have $\delta^{18}O$ values in the same range, but most show a progressive decrease in $\delta^{18}O$ with decreasing $^{207}Pb/^{206}Pb$ (increasing discordance), decreasing to a mean value of *c.* 4.5 ‰. Both the increasing discordance and the falling $\delta^{18}O$ values indicate that most of the zircons, following crystallisation at *ca.* 3.2 Ga, became open to isotopic exchange with circulating hydrothermal fluids.

The effects of late alteration is more pronounced in sample IK-2 (granite) in which not only are all but one zircon analysis is highly discordant, but the array of zircon analyses indicates that the *ca.* 2.94 Ga granites were strongly affected by a *ca.* 0.77 Ga event. Most of the zircons do not preserve their original mantle $\delta^{18}O$ values and there is a wide range of values between -0.1 and 5.4 ‰ (one higher value at 7.8 ‰), with most of the analyses spread between 0.5 and 2.5 ‰ (fig. 8C). Such low $\delta^{18}O$ values indicate interaction with an isotopically light fluid, probably with a large component of hydrothermal fluid. The high common Pb contents of many of the grains are also indicative of significant isotopic exchange.

## DISCUSSION

### *Models for TTG Petrogenesis*

The petrogenesis of TTG remains a major topic of debate. Although it is evident that they can originate from partial melting of hydrated basaltic rocks, both the process and geodynamic setting are controversial. The TTG magma could be generated by (a) melting of oceanic plateau crust; (b) melting of subducted oceanic crust that

TABLE 5

*LA-ICPMS single zircon Lu–Hf isotopic data for IK-1 sample (TTG-I)*

| Sample | t (Ma) | $^{176}Yb/^{177}Hf$ | 2σ | $^{176}Lu/^{177}Hf$ | 2σ | $^{176}Hf/^{177}Hf$ | 2σ | $e_{Hf}(0)$ | $e_{Hf}(t)$ | 2 s | $T_{DM}$ | $T_{DM}^{c}$ | $f_{Lu/Hf}$ |
|---|---|---|---|---|---|---|---|---|---|---|---|---|---|
| 1512-1 | 3201 | 0.033709 | 0.000976 | 0.001032 | 0.000029 | 0.280900 | 0.000021 | -66.2 | 3.9 | 0.7 | 3267 | 3306 | -0.97 |
| 1512-2 | 3201 | 0.017545 | 0.000634 | 0.000598 | 0.000021 | 0.280856 | 0.000027 | -67.8 | 3.3 | 0.9 | 3290 | 3343 | -0.98 |
| 1512-3 | 3201 | 0.032156 | 0.000689 | 0.000974 | 0.000017 | 0.280870 | 0.000021 | -67.3 | 2.9 | 0.8 | 3302 | 3362 | -0.97 |
| 1512-4 | 3201 | 0.021139 | 0.000635 | 0.000727 | 0.000022 | 0.280870 | 0.000023 | -67.3 | 3.5 | 0.8 | 3281 | 3329 | -0.98 |
| 1512-5 | 3201 | 0.025997 | 0.000747 | 0.000825 | 0.000021 | 0.280878 | 0.000022 | -67.0 | 3.6 | 0.8 | 3278 | 3324 | -0.98 |
| 1512-6 | 3201 | 0.015875 | 0.000261 | 0.000536 | 0.000008 | 0.280874 | 0.000021 | -67.1 | 4.1 | 0.7 | 3260 | 3295 | -0.98 |
| 1512-7 | 3201 | 0.023836 | 0.000268 | 0.000784 | 0.000008 | 0.280858 | 0.000022 | -67.7 | 2.9 | 0.8 | 3303 | 3364 | -0.98 |
| 1512-8 | 3201 | 0.035148 | 0.000426 | 0.001037 | 0.000013 | 0.280906 | 0.000027 | -66.0 | 4.1 | 1.0 | 3259 | 3294 | -0.97 |
| 1512-9 | 3201 | 0.023920 | 0.000277 | 0.000780 | 0.000009 | 0.280826 | 0.000025 | -68.8 | 1.8 | 0.9 | 3345 | 3431 | -0.98 |
| 1512-10 | 3201 | 0.030167 | 0.001019 | 0.001045 | 0.000035 | 0.280856 | 0.000035 | -67.7 | 2.3 | 1.2 | 3327 | 3401 | -0.97 |
| 1512-11 | 3201 | 0.016036 | 0.000546 | 0.000536 | 0.000016 | 0.280836 | 0.000026 | -68.5 | 2.7 | 0.9 | 3311 | 3378 | -0.98 |
| 1512-12 | 3201 | 0.027343 | 0.000265 | 0.000889 | 0.000012 | 0.280811 | 0.000022 | -69.3 | 1.0 | 0.8 | 3374 | 3476 | -0.97 |
| 1512-13 | 3201 | 0.021463 | 0.000744 | 0.000698 | 0.000020 | 0.280864 | 0.000021 | -67.5 | 3.3 | 0.8 | 3287 | 3339 | -0.98 |

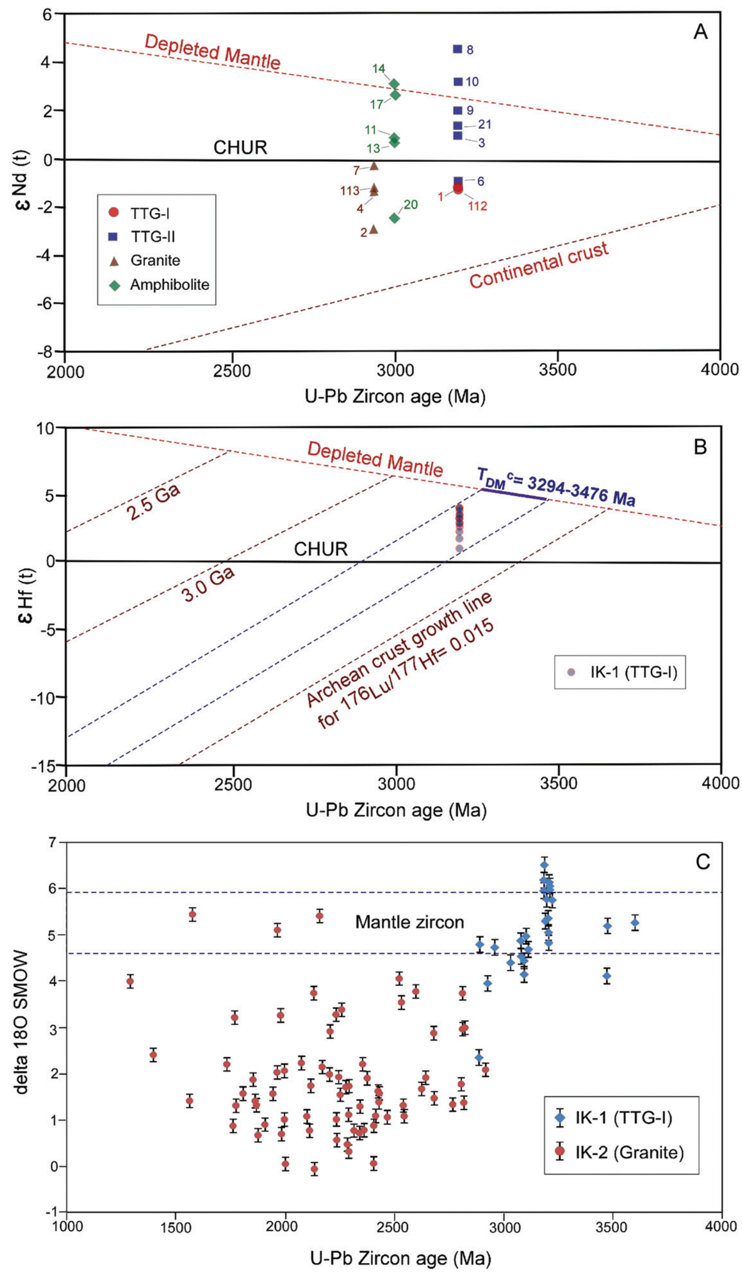


Fig. 8. A. A plot of εNd(t) vs. U-Pb zircon ages of TTG, granite and amphibolite samples. B. εHf(t) vs. U-Pb zircon ages ($^{207}Pb/^{206}Pb$) plot for sample IK-1 (TTG-I). C. δ $^{18}O$ SMOW vs. U-Pb zircon ages ($^{207}Pb/^{206}Pb$) plot for samples IK-1(TTG-I) and IK-2 (granite). Note that in Fig.8C for sample IK-2, analyzed sites are mostly isotopically disturbed.

originated at a spreading center; (c) melting of basalt at the base of an oceanic arc (Polat, 2012), or (d) partial melting of the mafic lower crust (Hastie and others, 2010). Many studies support a uniformitarian paradigm according to which horizontal forces in the early Earth were responsible for the development of plate tectonics and

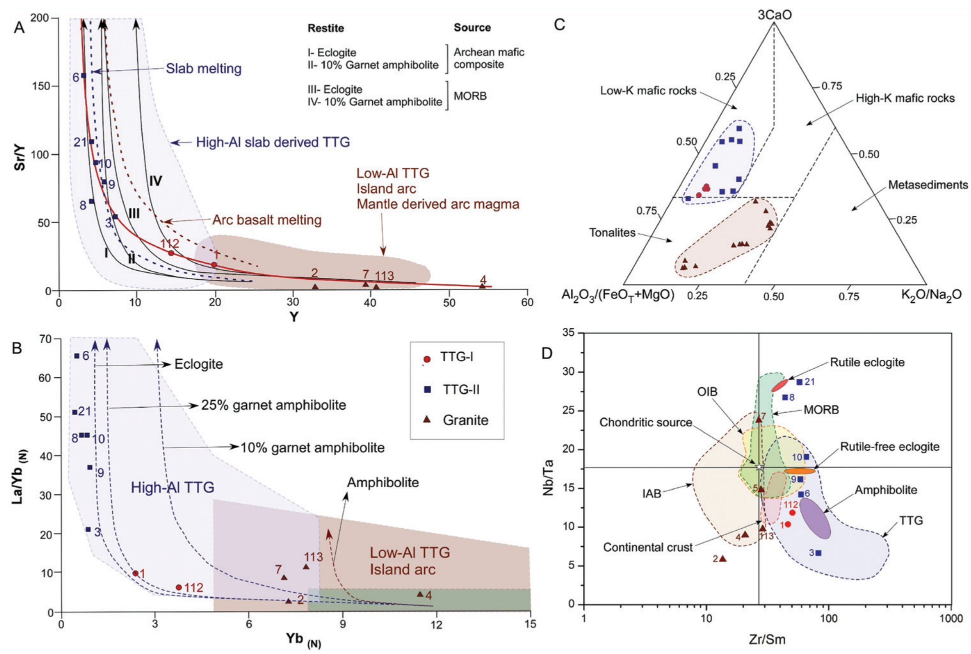

Fig. 9. A. Sr/Y vs. Y (ppm) plot (after Drummond and Defant, 1990) showing the differences between slab-derived TTG and TTG from mantle-derived magma. The basalt partial melting curves distinguishing source and restite compositions are also overlayed suggesting that TTG-II rocks formed by slab melting and granite from melting of older crust during intrusion of mantle-derived arc magma. B. La/Yb$_{(N)}$ vs. Yb$_{(N)}$ diagram (after Martin, 1986; Drummond and Defant, 1990) showing basalt partial melting curves with restite assemblages. C. $Al_2O_3/(FeO_t + MgO)$-3*CaO-5*($K_2O/Na_2O$) diagram with fields representing the compositions of melts derived from a range of potential sources (after Laurent and others, 2014). D. Nb/Ta versus Zr/Sm of samples, comparing results of modelled melting of rutile-bearing eclogite, rutile-free eclogite and amphibolite (after Foley and others, 2002).

the early crust of Earth developed by some form of modern-style accretionary plate tectonics. They envisage that TTG formed during subduction and partial melting of hydrated MORB-like crust at various times in the Archean (for example, Condie, 1986; Martin, 1986; Drummond and Defant, 1990; Windley, 1996; Foley and others, 2002; Taylor and McLennan, 1995; Rollinson, 2010; Windley and others, 2021). Most studies considered TTG to be the Archean analogues of modern adakites, which probably formed by oceanic slab melting in subduction zones. However, adakites are characterised by lower $SiO_2$ and higher MgO contents, which differ from the Archean TTG compositions. TTG are also proposed to have formed by melting of subduction-derived mafic lavas, such as tholeiitic basalt and boninite, in the lower part of thickened oceanic island arcs (Nagel and others, 2012; Adam and others, 2012). Polat (2012) proposed that Archean TTG formed by partial melting of arc basalts under amphibolite-to-eclogite facies metamorphic conditions in the lower section of Archean oceanic arcs. Based on *in situ* zircon Hf isotopic evidence, Guitreau and others (2012) suggested that continental crust was generated by partial melting at subduction zones of oceanic plateaux, which in turn were formed by the shallow melting of primitive mantle material brought from the lower mantle by upwelling plume heads. This plume model was followed by Martin and others (2014) who proposed that, given the similarity in trace element signatures between Archean TTG-associated amphibolites and the basalts of plume-related oceanic plateaux, TTG were produced episodically when oceanic plateaux were subducted. Alternatively, Jayananda and others (2015) proposed a model that involved subduction of oceanic slabs to generate island arc crust, followed by the remelting of the thickened island arc base to produce TTG magma.

In contrast, many other studies have proposed non-uniformitarian models, suggesting that vertical forces were dominant in the early Earth, and that TTG were generated by the partial melting of mafic material at the base of thickened crust (for example, Atherton and Petford, 1993; Smithies, 2000; Bédard and others, 2003; Turkina and Nozhkin, 2003; Condie, 2005; Hastie and others, 2010). Smithies (2000) pointed out that, unlike modern adakites, TTG older than 3.0 Ga show no evidence of mantle wedge peridotite interactions or that the magma originated from a slab. Differences between Archean and modern subduction processes possibly account for the differences between TTG and adakites, with shallow subduction in the Archean producing magmas with higher $SiO_2$ and lower MgO contents than the deeper subduction of the present day (Smithies, 2000). According to Smithies and others (2019), most TTG formed thorough melting of hydrated mafic crust, but high-pressure TTG were formed by fractionation of melts derived from metasomatically enriched lithospheric mantle. Any environment in which hydrous mafic rocks, either former oceanic plateaux (Willbold and others, 2009) or MORB (Rollinson, 2009), melting at a high pressure would be suitable to form TTG, provided the mafic crust was thick enough.

### *TTG Genesis in the Karwar Block*

The inferred TTG-I protoliths were the products of volcanic arc magmatism (figs. 3G, H), resulting from the subduction and partial melting of a MORB-like (amphibolite) crust at moderate depths and under moderate pressure conditions (figs. 9A, B, C). This is evident from their negative Nb and Ta anomalies (Zheng, 2019), weakly enriched HREE (figs. 5A, C), moderate Fe, Mg, Ca, Na and Sr contents (figs. 3A, B, C, D), and Sr/Y and La/Yb $_{(N)}$ ratios (Drummond and Defant, 1990) (figs. 9A, B). It is also evident that TTG-I formed from the melting of low-K mafic rocks (fig. 9C; after Laurent and others, 2014). The Nb/Ta vs. Zr/Sm variation diagram (fig. 9D; after Foley and others, 2002) indicates that TTG-I formed by melting of amphibolites at low- to moderate-degrees of partial melting. TTG-I rocks are characterised by less-fractionated REE patterns than TTG-II, with characteristic negative Eu anomalies (Eu/Eu* ranges from 0.53 to 0.64) and low Sr/Y and La/Yb $_{(N)}$ ratios indicative of plagioclase in the residue (without significant residual garnet) and hence were derived from low-degree melting at relatively shallow depth. TTG-I (sample IK-1) has a zircon U-Pb crystallisation age of *ca.* 3201 Ma, plus evidence of *ca.* 3601 Ma, 3476 Ma, 3473 Ma zircon inheritance (Ishwar-Kumar and others, 2013). These results, and the weak negative $\epsilon$Nd(t) value of $-1.4$ (figs. 7B, 8A), weak positive $\epsilon$Hf(t) values of 1.0 to 4.1 (fig. 8B) and $\delta^{18}O$ values mostly within, but with a few outside, the mantle zircon range (total range of 4.0–6.5 ‰ with most between 5.3–6.2 ‰ and one exceptionally low value of 2.4 ‰) (fig. 8C), suggest incorporation of a significant component of older crustal material by the mantle-derived material in the source of TTG-I. The $T_{DM}{}^{c}$ model ages suggests that the melt source of TTG-I was possibly separated from the depleted mantle between 3.29 to 3.47 Ga (fig. 8B). Older zircon inheritance and crustal material incorporation in TTG-I is also consistent with melting at moderate depth under moderate pressure-temperature *(P-T)* conditions.

The inferred TTG-II protoliths were also formed from a volcanic arc magma (figs. 3G, H), likely resulting from the subduction and partial melting of a MORB-like (amphibolite) crust, but at greater depth and under higher pressure conditions than for TTG-I (figs. 9A, B). The strong negative Nb-Ta anomaly, strong LREE/HREE fractionation and high Sr/Y and La/Yb $_{(N)}$ ratios indicate the presence of residual garnet (more than 25%) and rutile in residual eclogite, which can form in (a) the deeper part of a slab, (b) thickened mafic lower crust or (c) sagducted hydrated mafic greenstones (Hoffman and others, 2011; Zheng, 2019). The high Th/Nb ratios in modern subduction-related magmas with distinct negative Nb and Ta anomalies are due to fluid-fluxed melting in the mantle wedge between the downgoing oceanic lithosphere and overriding magmatic arc (Hawkesworth and others, 2020). Hence strong negative Nb and Ta anomalies and high Th/Nb ratios provide evidence for a subduction-related origin (Zheng, 2019; Hawkesworth and others, 2020). The strong negative Nb and Ta anomalies, together with high Th/Nb ratios (1.18 to 3.43, except for 0.64 in sample IK-3), in TTG-II are indicative of a subduction origin. Lack of HREE enrichment (figs. 5A, B), the high Fe, Mg, Ca, Na and Sr contents (figs. 3A, B, C, D) and high Sr/Y vs. Y and La/$Yb_{(N)}$ vs. $Yb_{(N)}$ (figs. 9A, B) all point to an origin at greater depth and under higher pressure conditions than TTG-I. The TTG-II formed from melting of low-K mafic rocks (fig. 9C), that is, Archean MORB with eclogite/garnet amphibolite as residue (figs. 9A, B). The Nb/Ta vs. Zr/Sm variation diagram (fig. 9D) (after Foley and others, 2002) indicates that TTG-II rocks were the result of a moderate- to high-degree of melting. It is also evident that most TTG-II samples are high-pressure TTG formed by melting at a greater depth, with rutile eclogite (samples IK-8 and IK-21) or eclogite as residue (samples IK-6, IK-9 and IK-10), whereas sample IK-3 is a medium-pressure TTG formed by melting at a moderate depth with an amphibolite residue (figs. 3F, G; figs. 9A, B, D). The fractionated REE patterns of TTG-II with low HREE and high $(Gd/Yb)_N$ and $(La/Yb)_N$ values are indicative of garnet in the residue, and hence melting at a greater depth and interaction with the mantle wedge. TTG-II has lower Rb/Sr ratios and no Eu anomalies, because at greater depths plagioclase is not retained in the residue. The high LREEs in TTG-II may also be due to interaction with fluids during slab melting. REE patterns and positive $\epsilon$Nd(t) values (4.6 to 1.0, with one exception at −1.1) (figs. 7B, 8A) indicate that the TTG-II source was most likely a mantle-derived juvenile magma that had an Ocean Island Basalt (OIB) or Mid-Ocean Ridge Basalt (MORB) signature (fig. 7B). However, sample IK-6 has a weak negative $\epsilon$Nd(t) value (-1.1), probably a result of an older crustal input. A major contribution of mantle magma in TTG-II is consistent with melting (both slab and wedge melting) at a greater depth than TTG-I with more effective mixing of the slab melt with mantle peridotite.

The granites were mostly derived from intracrustal melting during within-plate magmatism, as indicated by their trace element signatures (figs. 3H, I) and also the lack of Nb and Ta anomalies, which do not support a subduction-related origin (fig. 5A). The association of the granites with amphibolites and melt veins, along with their Nd isotope and trace element signatures, indicate that the granites were probably formed by the melting of older TTG crust (fig. 9C) as a result of intrusion of mantle-derived arc magma (fig. 9A). The granites have high K and Rb and low Na, Fe, Mg and Sr contents, and low Sr/Y, $(La/Yb)_N$ and $(Gd/Yb)_N$ ratios, all consistent with a derivation by assimilation and melting of pre-existing crust at a shallow depth and under low-pressure conditions (figs. 9A, B). At such a shallow depth, plagioclase would be stable in the residue, and hence the granites have prominent negative Eu anomalies (Eu/Eu* ranges from 0.28 to 0.44), and relatively high Rb/Sr ratios, because Rb is incompatible and concentrates in the melt at low degrees of melting. The granites have less fractionated REE patterns and high HREE contents (fig. 5B), because garnet and amphibole are not stable at shallow depth. Hence, underplating of the early-formed TTG crust by the ascent of a mantle-derived magma resulted in crustal assimilation, induced melting and differentiation, leading to the formation of granites at 2.94 Ga. The granites have negative $\epsilon$Nd(t) (−0.2 to −3.0) values (fig. 7B, 8A) consistent with incorporation of older crust. The granites also have low zircon $\delta^{18}O$ (range of −0.1 to 5.4 ‰ with most between 0.5 and 2.5 ‰) (fig. 8C), but most of the zircons are discordant suggesting they were affected by hydrothermal alteration. Various processes can be invoked to explain low $\delta^{18}O$ zircon, for example assimilation and melting of hydrothermally-altered crust either at shallow crustal levels, deep in the crust, by differentiation from a low $\delta^{18}O$ mantle source (Bindeman and others, 2008), or by post-emplacement interaction of the zircon with meteoric water. Neodymium isotopes indicate that the granites incorporated older crustal material either in the source or as the result of assimilation during emplacement (figs. 7A, B).

All the amphibolite samples represent metamorphosed basalt/gabbro (figs. 4B, D). Most amphibolites (except samples IK-13 and IK-14) appear to have been plate-margin basalt (fig. 4C), with MORB-like chemical compositions, consistent with being either mafic volcanics or instrusive gabbros (figs. 4E, F, G, H, I; fig. 5B). Some amphibolites (samples IK-11 and IK-12) are characterised by a lack of LREE enrichment and have low Fe, Ti, Nb and Zr, and high Mg contents, similar to island-arc tholeiite (SSZ) and volcanic arc basalts (figs. 4E, F, G, H; figs.5B, D). Samples IK-13 and IK-14 have high Fe, Ti, Nb and Zr, and low Mg contents, high $(Gd/Yb)_N$ and $(La/Yb)_N$ ratios and enriched REE patterns indicating melting at a greater depth in a within-plate setting from an enriched source (figs. 4E, F, G, H, I; figs. 5B, D). The εNd (t) values of the amphibolites ranges from 0.7 to 3.1 (one exceptional value of -2.5, sample IK-20), indicative of a magma source mostly from depleted mantle (figs. 7B, 8A).

### *Compositional Variations in TTG*

Most TTG are sodic in composition, however some potassic plutonic rocks resembling TTG have been referred to as enriched or transitional TTG (similar to granite) (Turkina and Nozhkin, 2003), although many studies have suggested that only high-Al sodic rocks with fractionated REE and low HREE are true TTG (for example, Feng and Kerrich, 1992; Willbold and others, 2009). The $K_2O$ content of a rock is mainly a function of its source composition (potassic minerals in the source) and the degree of partial melting (Shaw, 1970). During the subduction of oceanic crust beneath continental crust, a subducted slab dehydrates, and the upwelling of derived fluids can cause melting in the mantle wedge or at the base of the overlying crust. A slab may also partially melt and interact with the upper mantle and lower crust, causing metamorphic reactions. According to Fyfe and McBirney (1975), during the initial dehydration minerals such as talc, serpentine, mica and amphibole from the subducting slab break down and some of them release Na-rich fluids, raising the K/Na ratio in the slab. Low-Al TTG can be produced after the extraction of trondhjemitic melts, resulting in an enrichment of $K_2O$ in the remaining melt, thus producing potassic TTG (Fyfe and McBirney, 1975; Drummond and Defant, 1990). The Mg, Ni and Cr contents of a magma are also controlled by the depth of melting and mixing of a slab melt with peridotite in the overlying mantle wedge. The low Mg content in Archean TTG might have been due to low-angle subduction in the Archean, which resulted in partial melting at a moderate to shallow depth with less contamination from a thin mantle wedge (Hastie and others, 2016). Based on a study of TTG and granites from the Singhbhum craton of India, Upadhyay and others (2019) proposed a geodynamic setting with a very hot subduction or “dripduction” regime involving shallow melting due to delamination of the base of the mafic lower crust, leading to simultaneous generation of trondhjemitic TTG and granites (potassic TTG).

Transitional TTG (TTG-I) or potassic TTG (granites) are generated by low degrees of partial melting of hydrous basaltic rocks at moderate to low pressures (10–12 kbar; *c.* 30–36 km depth) in the plagioclase stability field (Moyen, 2011; Moyen and Martin, 2012). They are characterised by high K, Rb, Nb and Ta, and low Al, Na, Sr and Eu contents, high Rb/Sr and low La/Yb and Sr/Y ratios, weakly fractionated

REE, and high HREE contents (figs. 3A, B, C, D, and 5A, B). As subduction of the slab continues to greater depths, the degree of partial melting increases and the melt becomes richer in Fe and Mg and lower in $K_2O$ and Rb (Moyen and Martin, 2012). Trondhjemitic TTG (TTG-II) melts are generated by high degrees of partial melting at depths > *c.* 45 km and under high-pressure (> 15 kbar) conditions (Moyen and Stevens, 2006). They are characterised by high Al, Na, Sr and Eu contents, high La/Yb and Sr/Y ratios, low K, Rb, Y, Nb and Ta contents, and fractionated REE patterns with low total HREEs (figs. 3A, B, C, D, and 5A, B). REE fractionation and lack of HREE enrichment of the melt indicate partial melting of mafic rocks at depths at which garnet is stable in the residue, thereby retaining the HREE (Moyen and Martin, 2012). The LREE enrichment found in the Karwar TTG-II is not very strong, perhaps because the depth of partial melting and fractionation was barely within the garnet stability field.

*Development of Plate Tectonics and Formation of TTG in the Archean*

When and how modern-style plate tectonics began on Earth, and how TTG developed within that framework is one of the most controversial subjects in Earth sciences today (Condie and Pease, 2008). Utilising the results from this study, we will summarize the plate tectonic models that are consistent with the field and geochemical evidence for the occurrence of TTG and how this relates to the geology of the Karwar block. There are two main models for the operation of plate tectonics today and in the Archean:

A uniformitarian approach, which has long considered that Wilson cycle plate tectonics (Wilson, 1968) has prevailed on Earth back to the Archean-Proterozoic boundary at *ca.* 2.5 Ga or 3.2 to 3.0 Ga (Condie and Pease, 2008; Hawkesworth and others, 2010; Van Kranendonk, 2011; Shirey and Richardson, 2011; Cawood and others, 2013; Dhuime and others, 2012; Næraa and others, 2012; Johnson and others, 2017, 2019). Wilson Cycle Plate Tectonics starts with the rifting of a continent, as in East Africa, and ends with the collision of two continental blocks, as in the Himalaya, and has a relatively short life of *ca.* 200 Ma. However, the Wilson cycle plate approach to early Earth history has been demonstrated to be inadequate, because it failed to recognise the role of Accretionary Plate Tectonics (Şengör and Natal'in, 1996; Cawood and others, 2009), which has long been known to be responsible for the development of the orogenic belts along the current Western Pacific from the incipient stage in Indonesia (Hamilton, 1969) to the mature stage in Japan with a 500 My history, to completion in the Central Asian Orogenic Belt (Windley and others, 2007) and the Arabian-Nubian Shield (Kröner and others, 2007).

Accretionary Cycle Plate Tectonics starts with an ocean opening against a continental back-stop, continues with successive accretion of mafic oceanic crust, of pelagic oceanic cherts (ocean plate stratigraphy), juvenile island arcs, ophiolites, oceanic plateaux and seamounts, and ends with collision against a continental block (Wakita and others, 2013). Accretionary orogens can be tracked back to about 4.0–3.9 Ga (Komiya and others, 2015; Nutman and others, 2015; Hastie and others, 2016; Harrison, 2020; Windley and others, 2021), the evidence being the diagnostic ocean plate stratigraphy that records the presence of an oceanic plate as it moves from a mid-oceanic ridge to a trench, of accreted island arcs, and of thrust piles of accreted trench-type material in worldwide supracrustal belts in Nuvvuagittuq and Nulliak in Canada, Isua in Greenland, the East Pilbara in Australia, and Barberton in South Africa (Windley and others, 2021).

Specific geological, geophysical and geochemical features that suggest burial of surface material to depths of 50 to 100 km include an "arc" signature, the structure of thrust belts and dipping seismic reflectors, and paired metamorphic belts, which were interpreted to be subduction-related (van Hunen and Moyen, 2012). From a geochemical study of *ca.* 3.7 Ga high-pressure TTGs from the Tarim craton in NW China, Ge and others (2018) suggested they were generated by partial melting of a subducted proto-arc during arc accretion, and consequentially that modern-style plate tectonics was operative, at least locally, during the Eoarchean and responsible for generating some of the oldest continental nuclei. Based on their synthesis of geodynamical and geochemical evidence, van Hunen and Moyen (2012) proposed that shallow and flat subduction occurred in the Archean, which was more episodic, with more intermittent plate motions, than the present day. Hence, the major geochemical difference between TTG and modern adakites is, low MgO and other compatible elements in TTG (Smithies, 2000), which might be due to shallow and flat subduction in the Archean, coupled with melting at shallower depths and less interaction with the mantle wedge.

Non-uniformitarian models are mostly based on the idea that there were no accretionary plate tectonics in the early-mid Archean, but instead mantle plumes generated early Archean magmatic rocks, and modern-style plate tectonics started at 3.2 to 3.0 Ga Ga., the evidence largely being placed on changes in the Rb/Sr ratio in juvenile crust (Dhuime and others, 2012) and on changes in eclogitic inclusions in kimberlitic diamonds (Shirey and Richardson, 2011). Windley and others (2021) pointed out that accretionary plate tectonics has been operating since 4.0 to 3.9 Ga and that 3.2 to 3.0 Ga marks the time when the first major Andean-type magmatism with a change in Rb-Sr ratios developed in active continental margin belts. After several later failed attempts to form small blocks of continental crust, and after the surge in growth of accretionary greenstone belts with their abundant mineralisation at *ca.* 2.9 to 2.7 Ga, sufficient crustal growth had taken place by the end of the Archean that large stable continents appeared and large-scale continents emerged above sea-level that enhanced continental weathering (Windley, 1977; Herwartz and others, 2021), which all reflected the major change in plate tectonic evolution at the Archean-Proterozoic boundary, as outlined by Windley (1996).

Non-uniformitarian models are myriad and include: dome-and-basin tectonics, sagduction and diapirism, ultra-hot orogens, and stagnant-lid tectonics, as well as predominant plume-generated oceanic plateaux (Windley and others, 2021). According to Hastie and others (2010), modern-style plate tectonics involving the subduction of lithospheric slabs has been a continuous process that probably did not start until about 3.1 Ga. In contrast, the production of TTG has been episodic, with most formed before 3.0 Ga. The *in situ* zircon Hf and O isotopic studies of Dhuime and others (2012) revealed that the process of continental growth in the Archean may have been continuous but at variable rates. A decrease in crustal growth rate at *ca.* 3.0 Ga was linked to the onset of subduction-driven plate tectonics. The Hf isotopic study of Næraa and others (2012) suggested that modern-style plate tectonic processes started at *ca.* 3.2 Ga when large volumes of continental crust were produced. Hawkesworth and others (2016) suggested that prior to 3.0 Ga crustal growth occurred in a pre-plate tectonic regime and that early plate tectonics, involving hot subduction with shallow slab breakoff, started by 3.0 Ga. They correlated the decrease in crustal growth at about 3.0 Ga with crustal recycling due to subduction. Johnson and others (2017) suggested that the early continents were not formed by subduction; instead TTG were formed near the base of thick plateau-like basaltic crust, and Johnson and others (2019) envisaged a fundamental transition in the geodynamic regime from vertical forces dominated by stagnant lid processes to laterally dominant mobile lid or plate tectonic processes starting at 3.3 to 3.0 Ga.

Rozel and others (2017) proposed a “Plutonic squishy lid tectonics regime dominated by intrusive magmatism” for the formation of Archean TTG that resulted in hotter geotherms that could form the HP, MP and LP TTG in the Archean. This is in contrast to "Io-like heat-pipe tectonics regime dominated by volcanism" of Moore and Webb (2013), which they argued could not produce Earth's primordial continental crust. In a recent study, Brown and others (2020) proposed that modern-style plate tectonics can be demonstrated on Earth only after the early Paleoproterozoic (*ca.* 2.2. Ga), that there was a transition from an early stagnant or sluggish lid tectonics to plate tectonics at 3.2 to 2.3 Ga and that development of a global network of narrow boundaries separating multiple plates could have been initiated by plume-induced subduction. Based on high-resolution three-dimensional numerical thermomechanical modeling, Gerya and others (2015) suggested that plume-induced subduction initiation could have started the first subduction zones without the help of plate tectonics, and Gerya (2014) envisaged that development of modern-style subduction on Earth started at 3.2 to 2.5 Ga, marked by the appearance of paired metamorphic belts and the oldest eclogites in subcontinental lithospheric mantle. However, more frequent slab break-off due to a hotter mantle resulted in more episodic subduction than at the present time.

Recently, Ranjan and others (2020) proposed that TTG $< 3.5$ Ga with juvenile εHf and short crustal residence time (no inheritance $> 3.6$ Ga) of the protoliths, have a subduction-related origin. They also proposed TTG $> 3.5$ Ga have chondritic or crust-like εHf with longer persistence of mafic sources suggesting generation at the base of a thicker crust or oceanic plateau. Most of the above studies suggested that a transition in the tectonic style of crust formation occurred between 3.3 to 3.0 Ga. However, the oxygen isotopes of chemical sediments (cherts) over Earth's history reflects directly on the composition of Archean seawater, on the spreading rate of oceanic crust, and on continental weathering and emergence, which are consistent with the onset of modern-style plate tectonics in the Eoarchean (Herwartz and others, 2021).

Many studies have proposed that the early crust on Earth was formed as a result of low angle subduction or underthrusting and delamination of an oceanic plateau-like crust (Foley and others, 2003; Martin and others, 2014; Nutman and others, 2015; Hastie and others, 2016; Johnson and others, 2017) which was dominant in the Eo- to Paleoarchean and that modern-style steep subduction processes started during the late Archean. However, although the partial melting of accreted oceanic plateau-like crust was a likely source for the TTG, some authors consider the formation of early crust was likely due to the partial melting of accreted island arc-like crust (Hoffman and others, 2014; Hastie and others, 2015). Based on phase-equilibrium modeling, Palin and others (2016) estimated a *P-T* range of ~10–18 kbar and ~800 to 950 °C for TTG genesis by metamorphism of hydrated basalt at the base of *c.* 40 km thick Archean oceanic plateau/over-thickened crust by delamination or tectonic underplating by shallow subduction. Choudhury and others (2020), based on numerical modeling, proposed that the late Archean secular transition from stagnant-lid to plate tectonic regime was caused by peel-back convergence. Sizova and others (2015) conducted 2D petrological-thermomechanical tectono-magmatic numerical experiments indicating a variety of tectono-magmatic settings in which felsic melts can be generated from hydrated primitive basaltic crust: (a) by delamination and dripping of the lower primitive basaltic crust into the mantle; (b) by local thickening of primitive basaltic crust; and (c) by small-scale crustal overturns. Turner and others (2014) investigated the stratigraphy and geochemistry of 3.8 Ga rocks from the Nuvvuagittuq complex of Canada and suggested that their compositions match modern-day forearcs and that at least some form of subduction might have been operating as early as the Eoarchean. Based on the study of the greenstones from the 3.8 Ga Nuvvuagittuq complex of Canada, Adam and others (2012) suggested that Earth's early crust could have been organised into several tectonic environments and these could have formed the first continental crust. They also suggested that the early Earth crust could have formed by horizontal tectonics and not only by plume-driven tectonics. O'Neill and others (2018) suggested that subduction might have operated in the early Earth, but it might have been short-lived. They also suggested that the transition from a pre-plate tectonic Earth to modern plate tectonics was nonlinear, and characterized by intermittent, short-lived subduction events during the Archean, transitioning to a more continual style of modern cold subduction during the Neoproterozoic. Roberts and others (2015) suggested that continental growth could have occurred in multiple ways, within and across geological time, with different contributions from primitive, or subduction-enriched, mantle and incorporating recycled continental crust, depending on the tectonic environment, resulting in the unique characteristics of the different terranes preserved today.

Considering that Archean TTGs may have evolved within the framework of several of the above tectonic models (Moyen and Martin, 2012), we note that in the Karwar block, TTGs of two predominant types both formed at *ca.* 3.2 Ga during a period of active continental magmatism.

This suggests the possibility of two distinct models:

(i) The TTG were the products of partial melting of the deeper parts of oceanic plateaux (Smithies and others, 2009; Willbold and others, 2009; Hastie and others, 2010, 2015; Van Kranendonk and others, 2015). However, Windley and others (2021) demonstrated using detailed trace element analysis that the geochemical characteristics of the main Archean TTG are far more compatible with a subduction zone origin than with a plume-generated oceanic plateau.

(ii) The TTG were generated by hydrous high-pressure fractional crystallisation in the lower crust of an island arc that resulted from subduction of oceanic lithosphere, as in the Cretaceous Kohistan arc batholith in the Himalaya of Pakistan (Jagoutz and others, 2013), the trace element characteristics of which are identical to those of Archean TTG. Although a similar idea was negated by Martin and others (2014), the Kohistan example demonstrates that a subduction-arc origin is entirely feasible.

### *Early Crust Formation and Paleo- to Mesoarchean Crustal Growth*

Crust formation processes depend on several factors such as the extent, continuity and thickness of pre-existing crust, the rate of plate movement, the input of mantle heat, and mantle convection. Crustal growth also varies according to the tectonic conditions of a region and through the time period from the Eo- to Mesoarchean. Smaller and thinner crustal fragments (Brown and others, 2020) allow faster plate motion and subduction and melting at moderate to greater depths, likely resulting in the formation of rocks similar to TTG-I and TTG-II, respectively, in the Karwar block. Larger areas of thicker crust would act as insulators that restrict the escape of heat from the mantle and may result in partial melting at the base of this thick pre-existing crust to form enriched granites, as in the Karwar block.

Accretion and under-thrusting of oceanic plateau-like or island arc-like crust would produce a thickened stack of crust (Martin and others, 2014). Melting at the base of this thickened crust at shallow to moderate depths (amphibolite facies zone) induced by magmatic underplating, probably formed segregations of thin TTG cumulates at 3.6 Ga in the Karwar block (fig. 10A). Such a process of crust formation is compatible with several models previously discussed (for example, Foley and others, 2003;

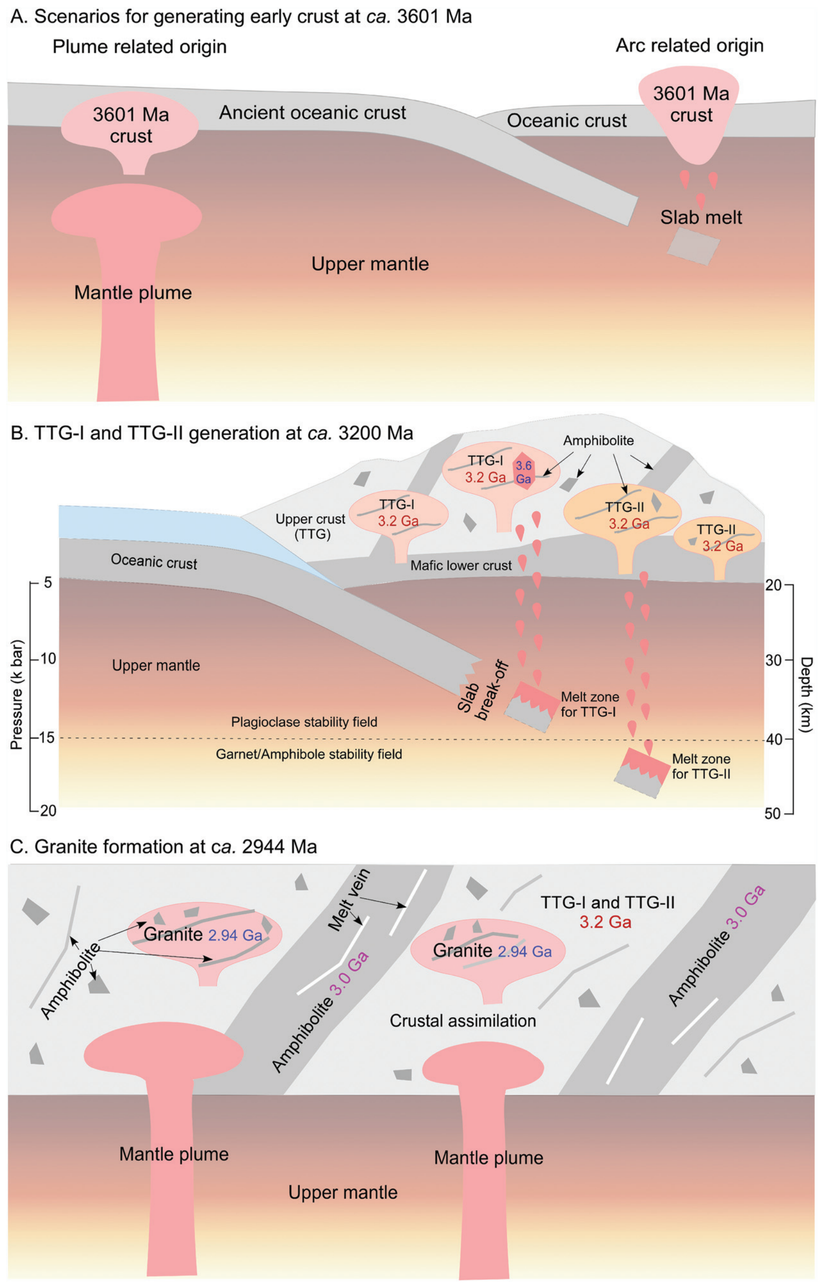


Fig. 10. Schematic model illustrating Archean crustal growth processes in the Karwar block. A. Generation of early crust at 3.6 Ga: Accretion and under-thrusting of oceanic plateaus to produce a thickened stack of crust. Melting at the base of the thickened crust at a shallow depth (amphibolite zone) induced by magmatic underplating to form the early 3.6 Ga crust. B. Generation of TTG-I and TTG-II rocks at *ca.* 3.2 Ga: Subduction of MORB beneath the early formed crust to form TTG-I (by slab melting at a moderate depth, partial melting of mafic lower crust and older upper crust) and TTG-II (by slab melting at a greater depth and partial melting of mafic lower crust) cumulates and remnant amphibolites. C. Thickened and more extensive crust, mantle-derived magma emplacement, assimilation and melting of the older TTG crust resulting in further differentiation that generated more enriched melts to form *ca.* 2.94 Ga granites.

Martin and others, 2014; Nutman and others, 2015; Hoffman and others, 2014; Hastie and others, 2015). The $\epsilon$Nd(t) vs. Sr(i) diagram (fig. 7B) indicates TTG-I rocks were likely derived from a lower crustal granulite facies mafic protolith. In contrast, *in situ* zircon $\epsilon$Hf(t) and $\delta^{18}$O values record the isotopic signature of a uniform (depleted) mantle reservoir for the source of the TTG-I rocks. Hence, TTG-I were formed at *ca.* 3.2 Ga most likely by subduction and a low-degree of slab melting (also wedge melting due to volatile release) at shallow to moderate depths. This caused underplating and induced melting of mafic lower crust and, when mixed with slab melt, formed a hybrid TTG melt that was further contaminated with older 3.4 to 3.6 Ga crust (fig. 10B). The *ca.* 3.60 Ga and *ca.* 3.47 Ga zircon inheritance (Ishwar-Kumar and others, 2013), the major and trace element compositions, and the Nd, Hf and O isotopic data together indicate the presence of older crust in the source region of TTG-I. The protolith magma was likely separated from the depleted mantle between 3.47 and 3.29 Ga (fig. 8B), and then incorporated *ca.* 3.6 Ga crustal material, indicating the existence of 3.6 Ga precursor crust and crustal reworking in the Paleo- to Mesoarchean. The TTG-II rocks also formed at *ca.* 3.2 Ga, most likely by subduction and partial melting of a MORB-like crust under moderate- to high-pressure conditions at a greater depth, together with efficient mixing with a mantle-derived magma (fig. 10B). The Nd isotopic data and trace element characteristics suggest that the TTG-II magma was also a hybrid magma, consisting of a dominant juvenile mantle component, with only minor additions from the lower crust. Intrusion of basaltic magma (possibly forming gabbros) at *ca.* 3.0 Ga and subsequent metamorphism likely formed the amphibolites. The granites formed at *ca,* 2.94 Ga from intracrustal melts in a within-plate setting by the assimilation and partial melting of pre-existing thickened crust, which was mixed with mantle-derived magma and further differentiated during the ascent (fig. 10C).

Similar crustal growth processes have been reported from many other Paleo-Mesoarchean terranes around the world. Upadhyay and others (2019) studied 3.4 Ga and 3.3 Ga TTG and granites, and 3.1 Ga granites, from the Indian Singhbhum craton and proposed a "dripduction" model to explain the simultaneous generation of TTG and granites. The 3.4 Ga and 3.3 Ga granitoids formed by melting of the same mafic crust, but crustal contamination increased from 3.4 Ga to 3.3 Ga. The *ca.* 3.4 Ga juvenile TTG formed by shallow melting of delaminated mafic lower crust, whereas large-scale delamination and melting of mafic lower crust and felsic proto-crust gave rise to younger granites with both juvenile and recycled signatures. They also proposed that the increasing $K_2O/Na_2O$ ratio of the granitoids from 3.45 Ga to 3.05 Ga was related to gradual thickening of the continental crust and to increasing contributions of intra-crustal melts in the form of the younger granitoids. Similar compositional variations are present in *ca.* 3.2 Ga TTG and *ca.* 2.94 Ga granites in the Karwar block, where the TTG have low $K_2O/Na_2O$, and the granites have high $K_2O/Na_2O$. Here, TTG-II have positive $\epsilon$Nd(t), whereas TTG-I have low negative $\epsilon$Nd(t), and the granites have negative $\epsilon$Nd(t). Overall, these geochemical signatures and their genesis are comparable with crustal growth in the Singhbhum craton.

In the Dharwar craton, there were five major periods of felsic crust formation, at *ca.* 3.45 to 3.3 Ga, 3.23 to 3.15 Ga, 3.0 to 2.96 Ga, 2.7 to 2.6 Ga, and 2.56 to 2.52 Ga, which are sub-contemporaneous with episodes of greenstone volcanism (Jayananda and others, 2018). Crustal growth in the Karwar block at 3.2 Ga, 3.0 Ga and 2.94 Ga is comparable with the Dharwar craton. Based on their geochemical and geochronological studies, Jayananda and others (2015) reported two major periods of crustal growth (3.35–3.28 Ga and 3.23–3.2 Ga) in the southern parts of the Western Dharwar craton (WDC), where low-Al TTG formed by low-pressure melting of a depleted mafic source at a shallow depth (island arc-type crust), whereas high-Al TTG formed by high-pressure melting of a less depleted mafic source (base of island arc crust or thickened oceanic plateau). The trondhjemites (younger TTG/3.23–3.2 Ga) were derived by high-pressure melting of an island arc-type crust with minor involvement of previously-accreted TTG. Granites formed at *ca.* 3100 Ma by crustal melting (Jayananda and others, 2015). The younger TTG (trondhjemite) rocks have negative Nb and Ta anomalies, higher Sr/Y and $(La/Yb)_N$ ratios and $\epsilon Nd(t)$ values of $-0.5$ to 2.4, suggesting mostly a juvenile mantle source, but with older crustal input. Hence, TTG-I and TTG-II are largely comparable with trondhjemites from the WDC in both composition and age. The granites in the Dharwar craton were derived mostly from a crustal source with minor mantle input and formed by melting at a shallow depth (Jayananda and others 2015, 2020). Results from this study indicate that the granites from the Karwar block have a similar origin to those of the WDC (even though the ages vary for granites in the WDC).

The Antongil block in north-eastern Madagascar was adjacent to the Karwar block before the break-up of India from Madagascar. TTG from the Nosy Boraha and Masoala suites of the Antongil block recorded early crustal growth at 3320 to 3231 Ma and 3187 to 3154 Ma (Schofield and others, 2010). Compositionally the difference is, the Antongil block contains less fractionated granitoids with low K/Na ratios and more fractionated TTG-like samples with high K/Na ratios; whereas the Karwar block contains less fractionated granitoids (granites) with high K/Na ratios and more fractionated granitoids (TTG-II) with low K/Na ratios. The Antongil block granitoids also have a wide range of REE patterns, with $(La/Yb)_N$ ratios ranging from 3 to 120 (Schofield and others, 2010). The rocks with high K/Na from the Antongil block have fractionated REE patterns with negative Nb and Ta anomalies, no Eu anomaly and high $(La/Yb)_N$ ratios, which are comparable with the TTG-II from the Karwar block. The low K/Na samples from the Antongil block have less fractionated REE patterns and negative Eu and Ti anomalies, which are comparable with the granites from the Karwar block. The high-K, younger *ca.* 2542 Ma granitoids from the Antongil block are similar in age to K-rich biotite-bearing *ca.* 2542 Ma granites of the Dharwar craton (Jayananda and others, 2000; Moyen and others, 2003), but both are younger than *ca.* 2944 Ma Karwar granites. The Antongil granites have highly fractionated REE patterns, which are also different from granites of the Karwar block and the Dharwar craton.

Based on a study of Archean crustal growth in the Dharwar craton, Jayananda and others (2018) suggested secular changes in TTG compositions through time, with a decrease in Si and increase in Ca, Fe, Mn, Mg, Ti, Ni, Cr, V, Ba, Sr and REE, which can be interpreted as resulting from an increasing depth of melting of oceanic arc crust and involvement of enriched mantle. TTG rocks older than *ca.* 3.6 Ga have not been documented from the Dharwar craton, but there are reports of >3.6 Ga detrital zircons, which Jayananda and others (2018) suggested might have been derived from an exotic source, possibly from the Pilbara and/or Kaapvaal cratons. TTG-I rocks from the Karwar block have *ca.* 3601 Ma inherited zircon, have whole-rock major, trace and REE compositions, Nd isotopes and *in situ* zircon Hf, O isotopic data that indicate the presence of *ca.* 3601 Ma crust in the Karwar block and its reworking during the Paleo- to Mesoarchean.

In the Karwar block, within just a small domain of crust, and during a relatively short period of time, crustal growth occurred by two different processes; shallow subduction and slab melting, followed by the assimilation and partial melting of pre-existing thickened crust accompanied by the intrusion of mantle-derived magma. Similar crust formation processes can be identified at the present-day, however they produce adakite instead of TTG due to steep subduction and melting at a greater depth, leading to more efficient mixing with mantle peridotite. The results of the present study suggest that many variable processes and tectonic styles contributed to Archean crustal growth in the Mesoarchean. Furthermore, the crust formation processes during the Archean were not unique, and that present-day styles of tectonics were at least locally active during the Mesoarchean.

## CONCLUSIONS

From the present study, based on the field, geochemical, geochronological, and isotopic results, the following conclusions can be made regarding TTG genesis and Archean crustal growth in the Karwar block:

- Integration of whole-rock major, trace and rare earth element data and Nd isotopes with *in situ* zircon Hf and O isotopic results, coupled with zircon inheritance, indicate the existence of 3.60 Ga and 3.47 Ga Paleo- Mesoarchean crust in the Karwar block.
- This early Archean crust was likely formed by the underplating and delamination of accreted/underthrust ocean plateau-like crust/island arc-like crust at *ca.* 3.60 Ga, and subsequently at *ca.* 3.47 Ga.
- Subduction of MORB-derived oceanic crust beneath the early-formed crust produced two types of TTG at *ca.* 3.2 Ga. TTG-I (by slab melting at a moderate depth and partial melting of mafic lower crust and older upper crust) and TTG-II (by slab melting at a greater depth than TTG-I, more effective mixing with mantle, accent of slab melt and induced partial melting of mafic lower crust).
- Amphibolites were derived from basalt/gabbro formed by *ca.* 3.0 Ga mafic magmatism. Most amphibolites have a MORB-like composition, some have island arc tholeiite or volcanic arc affinities, and a few have enriched compositions akin to within-plate basalts.
- Magma emplacement, assimilation and partial melting of thick and extensive crust resulted in further differentiation to generate more enriched melts that formed granites at *ca.* 2.94 Ga.
- The above results suggest that crustal growth processes in the Archean were not unique and varied according to the tectonic setting of the region, and that plate tectonic processes operated during the Paleo- to Mesoarchean.

## ACKNOWLEDGEMENTS

We thank three anonymous reviewers for their constructive reviews and suggestions, which significantly improved the manuscript. We thank Bruce Godfrey (CEO, Australian Scientific Instruments) for funding the SHRIMP II oxygen isotope analyses at RSES. The authors acknowledge help from Toshiro Takahashi and Rikako Nohara at Niigata University during the geochemical analyses. Analytical work at Niigata University was partially supported by the Japan Society for the Promotion of Science, Kakenhi Grant Numbers JP25302008 and JP15H05831 to M. S-K.

## APPENDIX

TABLE A1

*Sample details and mineralogy of TTG, granite and amphibolite from the Karwar block*

| Sl. No | Longitude | Latitude | Rock type | Major minerals | Accessary minerals | Texture | Field observations |
|---|---|---|---|---|---|---|---|
| IK-1 | 74.2846 | 14.7334 | TTG-I | Qtz, Pl, Bt, Amph | Zr, Py, Mt/ Ilm | Coarse-grained, euhedral fine -grained Bt along grain boundaries | Weakly deformed, no Amphibolite association observed in exposure |
| IK-112 | 74.2846 | 14.7334 | TTG-I | Qtz, Pl, Bt, Amph | Zr, Py, Mt/ Ilm | Coarse-grained, euhedral fine -grained Bt along grain boundaries | Moderately deformed, no Amphibolite associatio observed in exposure |
| IK-3 | 74.3360 | 14.6932 | TTG-II | Qtz, Pl, Bt, Amph | Zr, Mt/ Ilm | Coarse-grained | No Amphibolite association observed |
| IK-6 | 74.1686 | 14.7707 | TTG-II | Qtz, Pl, Bt, Amph | Zr, Py, Mt/ Ilm | Coarse-grained, euhedral Bt along grain boundaries | Moderately deformed,TTGs contain enclaves of amphibolites, leucocratic veins |
| IK-8 | 74.2028 | 14.8516 | TTG-II | Qtz, Pl, Bt, Amph | Zr, Mt/ Ilm | Coarse and wealky foliated grains, Bt along grain boundaries | Weak banding of amphibolites observed |
| IK-9 | 74.2510 | 14.8439 | TTG-II | Qtz, Pl, Bt, Amph | Zr, Py, Mt/ Ilm | Coarse-grained, euhedral Bt along grain boundaries | Weakly deformed, no Amphibolite association observed |
| IK-10 | 74.1244 | 14.8472 | TTG-II | Qtz, Pl, Bt, Amph | Zr, Mt/ Ilm | Coarse-grained, euhedral Bt along grain boundaries | Weak banding of amphibolites observed |
| IK-21 | 74.3141 | 14.6760 | TTG-II | Qtz, Pl, Bt, Amph | Zr, Py, Mt | Coarse-grained, euhedral Bt along grain boundaries | Weakly deformed, no Amphibolite association observed in exposure |
| IK-2 | 74.1394 | 14.7776 | Granite | Qtz, Pl, Bt, Amph, K-fls | Zr, Mt/ Ilm | Coarse-grained, fine -grained Qtz and Pl in matrix | Has luecocratic veins, moderately deformed |
| IK-4 | 74.1202 | 14.7978 | Granite | Qtz, Pl, Bt, Amph, K-fls | Zr, Mt/ Ilm | Medium-grained Qtz and Pl in matrix | Weakly deformed |
| IK-5 | 74.1187 | 14.7975 | Granite | Qtz, Pl, Bt, Amph, K-fls | Zr, Mt/ Ilm | Medium-grained Qtz and Pl in matrix | Weakly deformed |
| IK-7 | 74.2131 | 14.7671 | Granite | Qtz, Pl, Bt, Amph, K-fls | Zr, Mt/ Ilm | Coarse-grained, fine -grained Qtz and Pl in matrix | Similar to melt-veins observed in IK-6, moderately deformed |
| IK-113 | 74.1394 | 14.7776 | Granite | Qtz, Pl, Bt, Amph, K-fls | Zr, Mt/ Ilm | Coarse-grained, fine -grained Qtz in matrix | Similar to melt-veins observed in IK-6, weakly deformed |
| IK-15 | 74.3133 | 14.6944 | Amphibolite | Amph, Pl, Qtz, Bt | Mt/ Ilm/ Rt | Coarse grained, subhedral grains | Weakly deformed, found as enclaves within TTG-II |
| IK-16 | 74.1995 | 14.8537 | Amphibolite | Amph, Pl, Qtz, Bt | Zr, Mt/ Ilm | Medium-grained, perfectly euhedral Pl grains | Weakly deformed, no TTG association observed |
| IK-17 | 74.3717 | 14.8737 | Amphibolite | Amph, Pl, Qtz, Bt | Mt/ Ilm | Medium-grained | Undeformed, no TTG association |

TABLE A1
*(continued)*

| Sl. No | Longitude | Latitude | Rock type | Major minerals | Accessary mineral | Texture | Field observations |
|---|---|---|---|---|---|---|---|
| IK-18 | 74.2522 | 14.9111 | Amphibolite | Amph, Pl, Qtz, Bt | Mt/ Ilm | Medium-grained | Undeformed, no TTG association observed in exposure |
| IK-19 | 74.1137 | 14.8805 | Amphibolite | Amph, Pl, Qtz, Bt | Zr, Mt/ Ilm | Coarse-grained, euhedral Pl grains | Undeformed, no TTG association |
| IK-13 | 74.1686 | 14.7707 | Amphibolite | Amph, Pl, Qtz, Bt | Mt/ Ilm | Very fine-grained, anhedral amph grains | Weakly deformed, occurs as enclaves within TTG-II |
| IK-14 | 74.3873 | 14.6882 | Amphibolite | Amph, Pl, Qtz | Mt/ Ilm/ Rt | Coarse-grained, subhedral grains | Weakly deformed, no TTG association observed in exposure |
| IK-11 | 74.1187 | 14.7975 | Amphibolite | Amph, Pl, Qtz, Bt | Zr | Medium size anhedral grains, Zr in l grains, Bt along grain boundaries | Amphibolite as enclaves within TTG-II |
| IK-12 | 74.1686 | 14.7707 | Amphibolite | Amph, Pl, Qtz, Bt | Zr, Sph | Medium size anhedral grains, Zr in l grains, Bt along grain boundaries | Folaited amphibolites as enclaves within TTG- II, melt veins within amphibolites, all intruded by late pegmatite dikes |
| IK-20 | 74.4021 | 14.8604 | Amphibolite | Amph, Pl, Qtz | Zr, Mt/ Ilm | Medium size anhedral grains, folitae | Well foliated, occurs as enclaves within TTG -II |

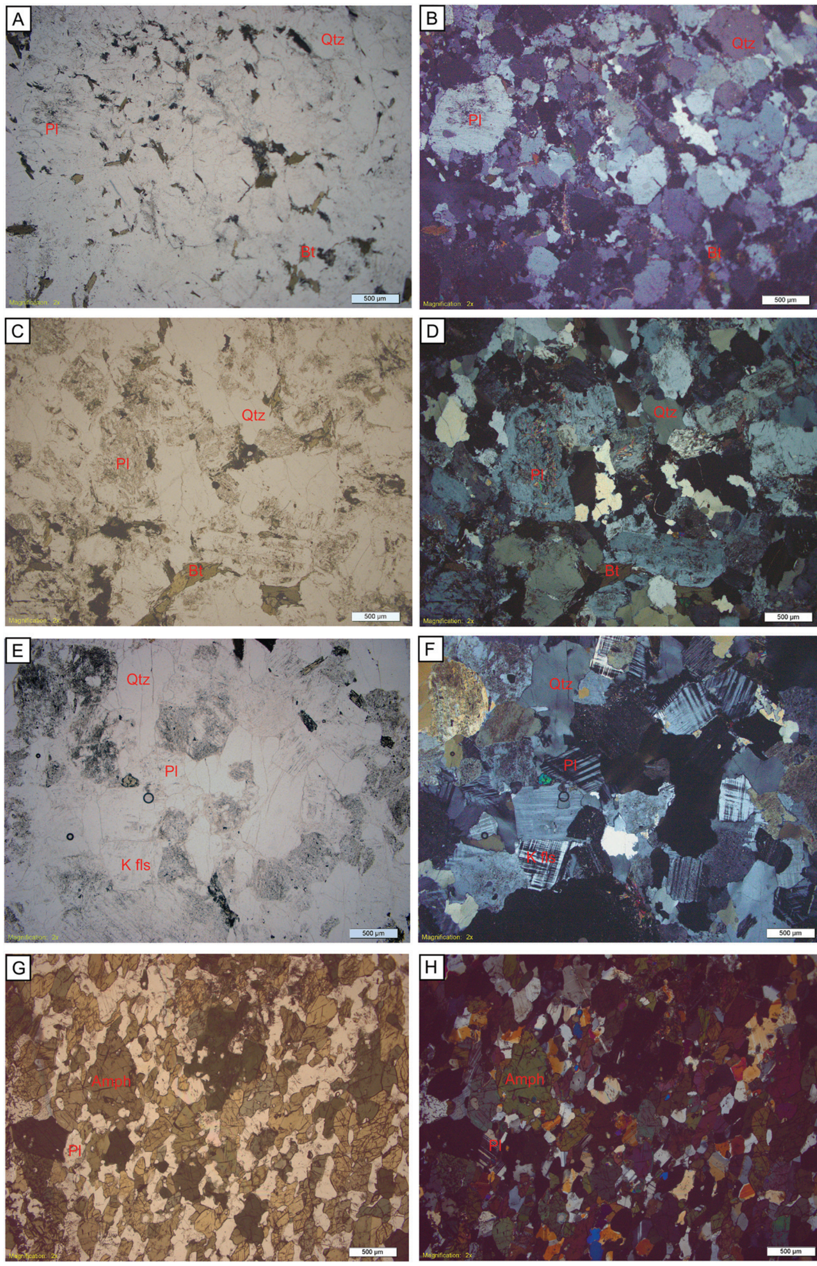


Fig. A1. Photomicrographs of samples in plane polarised (A, C, E, G) and cross polarised (B, D, F, H) light. A, B TTG-I; C, D TTG-II; E, F-Granite and G, H- Amphibolite. Acronyms: Qtz- Quartz, Pl- Plagioclase, K fls- K feldspar, Amph Amphibole, Bt- Biotite.

## ANALYTICAL TECHNIQUES

### *Whole-Rock Major and Trace Element Analysis*

A total of 30 felsic and 30 mafic rock samples were collected from the Karwar block. Whole-rock major and trace elements were analyzed by X-ray fluorescence (XRF) at Niigata University, Japan, for 29 felsic and 29 mafic samples. Data given in

TABLE A2

*Major and selected trace element compositions of reference materials measured using XRF*

| Sample No. | JB-2 | JB-2 | JB-2 | JB-1b | JB-1b | JB-1b | JB-1b | JB-1b |
|---|---|---|---|---|---|---|---|---|
| Major elements (wt%) | | | | | | | | |
| $SiO_2$ | 53.23 | 53.20 | 52.67 | 52.56 | 51.58 | 52.46 | 51.63 | 52.69 |
| $TiO_2$ | 1.19 | 1.19 | 1.17 | 1.25 | 1.28 | 1.25 | 1.28 | 1.25 |
| $Al_2O_3$ | 14.80 | 14.80 | 14.66 | 14.34 | 14.16 | 14.32 | 14.16 | 14.42 |
| FeO* | 14.21 | 14.23 | 14.12 | 9.09 | 9.18 | 9.07 | 9.17 | 9.05 |
| MnO | 0.22 | 0.22 | 0.22 | 0.15 | 0.15 | 0.15 | 0.15 | 0.15 |
| MgO | 4.59 | 4.57 | 4.53 | 8.55 | 8.18 | 8.57 | 8.10 | 8.72 |
| CaO | 9.82 | 9.81 | 9.74 | 9.69 | 9.98 | 9.71 | 9.99 | 9.72 |
| $Na_2O$ | 2.03 | 2.05 | 2.08 | 2.67 | 2.73 | 2.66 | 2.71 | 2.72 |
| $K_2O$ | 0.42 | 0.42 | 0.42 | 1.33 | 1.35 | 1.32 | 1.35 | 1.32 |
| $P_2O_5$ | 0.11 | 0.11 | 0.10 | 0.28 | 0.28 | 0.26 | 0.28 | 0.27 |
| Total | 100.59 | 100.58 | 99.70 | 99.90 | 98.86 | 99.75 | 98.82 | 100.30 |
| Trace elements (ppm) | | | | | | | | |
| Ba | 236.9 | 255 | 251.6 | 522.4 | 552 | 546.9 | 529.1 | 552.3 |
| Cr | 27.7 | 27.6 | 27.4 | 451.1 | 442.6 | 435.5 | 434.3 | 442.1 |
| Nb | 2.483 | 0.84 | 1.042 | 25.5 | 28.767 | 27.94 | 27.91 | 28.089 |
| Ni | 13.4 | 9.3 | 9.4 | 152.0 | 149.5 | 154.3 | 154.5 | 152.7 |
| Rb | 7.71 | 6.26 | 6.47 | 35.3 | 33.73 | 34.61 | 36.18 | 34.89 |
| Sr | 174.47 | 175.62 | 176.46 | 444.3 | 442.09 | 446.78 | 451.29 | 448.36 |
| V | 571.42 | 567.06 | 560.81 | 213.1 | 203.93 | 204.57 | 206.91 | 207.03 |
| Y | 24.163 | 24.719 | 24.207 | 23.0 | 24.243 | 24.187 | 23.892 | 24.465 |
| Zr | 47.48 | 47.4 | 46.28 | 125.4 | 133.97 | 134.24 | 134.74 | 135.26 |
| Pb | 3.141 | 3.049 | 5.032 | 6.0 | 3.438 | 5.619 | 4.597 | 5.273 |
| Th | n.d. | n.d. | n.d. | 5.0 | 6.612 | 6.107 | 5.77 | 6.055 |

the tables are powders prepared from 13 felsic and 13 mafic rock samples (table 1) at Niigata University. Major and trace elements were also analyzed for other powder samples prepared at the Indian Institute of Science, Bangalore, and these data were used only in figure 3 and figure 4, and are not given in the tables, although they are broadly similar to the Niigata samples. The whole-rock major element oxides were determined using a Rigaku RIX 3000 system at the Faculty of Science, Niigata University, Japan. Analytical procedures were as described by Takahashi and Shuto (1997) with GSJ reference materials (JB-2 and JB-1b) as standards. Glass disks were prepared by fusing each rock powder sample (1.8 g) with lithium tetraborate ($Li_2B_4O_7$, 3.6 g) for major element analysis. The values of standard reference material given in Appendix table A2.

### *Rare Earth Element Analysis*

REE and additional trace elements were analyzed for the same 13 felsic and 10 of the mafic rock samples (table 2) by inductively-coupled plasma mass spectrometry (ICP-MS, Agilent 7500a) at Niigata University. For the analyses, solutions were prepared by the alkali digestion method, using a $Na_2CO_3$ fusion and acid digestion procedure at 1050°C in a platinum crucible. After dissolution, solids were diluted by a factor of one million. Analytical procedures followed Neo and others (2009), with BHVO-2 of the US Geological Survey used as a standard. The deviation values were less than 5%. The values of standard reference material given in Appendix table A3.

Table A3

*Trace element compositions of reference materials measured using ICP-MS*

| | Average BHVO-2 n = 6 | 1 s | BHVO2-1 | BHVO2-2 | BHVO2-3 | BHVO2-4 | BHVO2-5 | BHVO2-6 | BHVO-2 Neo et al. 2006 |
|---|---|---|---|---|---|---|---|---|---|
| Li | 5.59 | 1.36 | 4.18 | 7.34 | 7.21 | 4.57 | 5.08 | 5.15 | |
| B | 24.68 | 25.65 | 1.07 | 2.02 | 1.10 | 43.84 | 47.58 | 52.46 | |
| Sc | 36.97 | 8.37 | 28.26 | 44.66 | 49.91 | 32.41 | 33.04 | 33.52 | 32.5 |
| V | 362.09 | 68.83 | 291.44 | 425.57 | 468.54 | 324.66 | 327.76 | 334.55 | 326 |
| Cr | 298.53 | 50.89 | 242.77 | 347.92 | 374.09 | 268.72 | 275.10 | 282.57 | |
| Co | 49.45 | 7.53 | 42.04 | 56.66 | 60.99 | 45.30 | 45.44 | 46.28 | 45 |
| Zn | 111.33 | 13.36 | 97.51 | 123.72 | 131.91 | 103.54 | 105.42 | 105.89 | 104.6 |
| Ga | 21.59 | 2.12 | 19.19 | 23.64 | 24.71 | 20.45 | 20.55 | 21.03 | 20.8 |
| Ge | 1.93 | 0.26 | 1.68 | 2.27 | 2.25 | 1.84 | 1.81 | 1.75 | |
| Rb | 9.52 | 0.51 | 8.85 | 9.92 | 10.29 | 9.40 | 9.23 | 9.44 | 9.4 |
| Sr | 389.87 | 18.90 | 367.00 | 404.13 | 419.91 | 384.50 | 381.58 | 382.13 | 389 |
| Y | 28.13 | 1.35 | 26.95 | 29.26 | 30.32 | 27.51 | 27.50 | 27.23 | 27.5 |
| Zr | 169.91 | 7.45 | 161.70 | 175.42 | 182.07 | 167.47 | 167.35 | 165.47 | 179 |
| Nb | 19.65 | 0.88 | 18.87 | 20.31 | 21.11 | 19.43 | 19.08 | 19.11 | 19.2 |
| Cd | 0.09 | 0.03 | 0.11 | 0.09 | 0.12 | 0.06 | 0.08 | 0.06 | |
| Cs | 0.10 | 0.01 | 0.10 | 0.09 | 0.09 | 0.11 | 0.09 | 0.10 | 0.1 |
| Ba | 126.01 | 3.21 | 129.05 | 123.33 | 122.75 | 130.40 | 126.69 | 123.82 | 132 |
| La | 14.73 | 0.48 | 15.45 | 14.46 | 14.56 | 15.20 | 14.44 | 14.27 | 15.2 |
| Ce | 35.96 | 1.12 | 37.36 | 35.09 | 35.05 | 37.30 | 35.97 | 34.99 | 36.9 |
| Pr | 5.22 | 0.19 | 5.32 | 5.04 | 5.05 | 5.53 | 5.27 | 5.12 | 5.32 |
| Nd | 23.29 | 1.04 | 24.72 | 22.69 | 22.07 | 24.37 | 23.22 | 22.69 | 24.3 |
| Sm | 5.69 | 0.24 | 5.91 | 5.47 | 5.44 | 6.04 | 5.63 | 5.64 | 6.05 |
| Eu | 1.98 | 0.10 | 1.95 | 1.88 | 1.86 | 2.10 | 2.06 | 2.02 | 2.03 |
| Gd | 5.93 | 0.23 | 6.36 | 5.88 | 5.72 | 6.01 | 5.82 | 5.81 | 6.14 |
| Tb | 0.89 | 0.04 | 0.96 | 0.89 | 0.85 | 0.90 | 0.86 | 0.86 | 0.95 |
| Dy | 4.88 | 0.29 | 5.33 | 4.84 | 4.50 | 5.09 | 4.83 | 4.69 | 5.23 |
| Ho | 0.93 | 0.05 | 1.02 | 0.90 | 0.89 | 0.98 | 0.91 | 0.90 | 0.99 |
| Er | 2.44 | 0.16 | 2.62 | 2.37 | 2.30 | 2.65 | 2.36 | 2.33 | 2.56 |
| Tm | 0.37 | 0.02 | 0.38 | 0.37 | 0.34 | 0.38 | 0.37 | 0.36 | |
| Yb | 1.89 | 0.19 | 1.87 | 1.64 | 1.80 | 2.06 | 2.16 | 1.83 | 1.96 |
| Lu | 0.25 | 0.02 | 0.28 | 0.24 | 0.22 | 0.26 | 0.25 | 0.25 | 0.27 |
| Hf | 3.72 | 0.28 | 3.96 | 3.57 | 3.33 | 4.10 | 3.69 | 3.65 | 4.22 |
| Ta | 1.06 | 0.07 | 1.10 | 1.00 | 0.97 | 1.16 | 1.08 | 1.02 | 1.18 |
| W | 0.26 | 0.05 | 0.35 | 0.22 | 0.26 | 0.25 | 0.20 | 0.28 | |
| Pb | 1.31 | 0.15 | 1.59 | 1.32 | 1.30 | 1.25 | 1.17 | 1.20 | 1.3 |
| Th | 1.16 | 0.11 | 1.29 | 1.06 | 1.02 | 1.26 | 1.22 | 1.15 | 1.25 |
| U | 0.41 | 0.05 | 0.44 | 0.35 | 0.34 | 0.47 | 0.42 | 0.41 | 0.416 |

### *SHRIMP Zircon U-Pb Geochronology*

For TTG-I (sample IK-1) (table 3a) zircon U-Pb dates were obtained using a sensitive high-resolution ion microprobe (SHRIMP II) at Curtin University, Australia. Zircons from each sample were mounted together with standards in an epoxy resin disc that was polished to obtain cross-sections through the grains. The C23 zircon standard was utilised, with a $^{206}Pb/^{238}U$ age of 564 Ma (Nelson, 1997). Prior to the U-Pb analyses, the mount was cleaned and coated with 40Å thickness of gold. To determine the internal structure of individual grains and to identify suitable analytical sites, backscattered electron (BSE) and cathodoluminescence (CL) images were obtained using a scanning electron microscope (SEM; JEOL JSM-5900 LV) at Curtin University. To obtain the SEM images a 0.2nA electron beam current and a 15kV acceleration voltage were used on the gold coated mounts. For the SHRIMP analyses, an $O_2-$

Table A4

*Sr and Nd isotopic compositions of reference materials measured using TIMS*

| Magazine/ Log | Sl. No | Sample No. | $^{87}Sr/^{86}Sr$ | Standard | Normalising Factor | $^{87}Sr/^{86}Sr$ |
|---|---|---|---|---|---|---|
| 2743 | 1 | NIST987 | 0.710242 | 0.710230 | 1.000030 | 0.710263 |
| 2743 | 2 | NIST987 | 0.710227 | 0.710230 | 1.000030 | 0.710248 |
| 2743 | 3 | NIST987 | 0.710221 | 0.710230 | 1.000030 | 0.710242 |
| 2744 | 4 | NIST987 | 0.710198 | 0.710201 | 1.000070 | 0.710248 |
| 2744 | 5 | NIST987 | 0.710193 | 0.710201 | 1.000070 | 0.710243 |
| 2744 | 6 | NIST987 | 0.710212 | 0.710201 | 1.000070 | 0.710262 |
| 2745 | 7 | NIST987 | 0.710279 | 0.710253 | 0.999997 | 0.710277 |
| 2745 | 8 | NIST987 | 0.710227 | 0.710253 | 0.999997 | 0.710225 |
| 2760 | 9 | NIST-987 | 0.710269 | 0.710241 | 1.000014 | 0.710279 |
| 2760 | 10 | NIST-987 | 0.710213 | 0.710241 | 1.000014 | 0.710223 |
| 2761 | 11 | NIST-987 | 0.710210 | 0.710227 | 1.000033 | 0.710234 |
| 2761 | 12 | NIST-987 | 0.710245 | 0.710227 | 1.000033 | 0.710268 |
| 2761 | 13 | NIST-987 | 0.710199 | 0.710199 | 1.000073 | 0.710251 |
| 2763 | 14 | NIST-987 | 0.710239 | 0.710239 | 1.000017 | 0.710251 |
| 2764 | 15 | NIST-987 | 0.710185 | 0.710185 | 1.000092 | 0.710251 |
| Average | | | | | | 0.710251 |
| SD | | | | | | 0.000017 |

| Magazine/ Log | Sl. No | Sample No. | $^{143}Nd/^{144}Nd$ | Standard | Normalising Factor | $^{143}Nd/^{144}Nd$ |
|---|---|---|---|---|---|---|
| 2745 | 1 | JNdi-1 | 0.512089 | 0.512072 | 1.000066 | 0.512123 |
| 2745 | 2 | JNdi-1 | 0.512055 | 0.512072 | 1.000066 | 0.512089 |
| 2746 | 3 | JNdi-1 | 0.512068 | 0.512061 | 1.000089 | 0.512113 |
| 2746 | 4 | JNdi-1 | 0.512053 | 0.512061 | 1.000089 | 0.512099 |
| 2747 | 5 | JNdi-1 | 0.512055 | 0.512051 | 1.000108 | 0.512110 |
| 2747 | 6 | JNdi-1 | 0.512047 | 0.512051 | 1.000108 | 0.512102 |
| 2748 | 7 | JNdi-1 | 0.512065 | 0.512056 | 1.000097 | 0.512115 |
| 2748 | 8 | JNdi-1 | 0.512048 | 0.512056 | 1.000097 | 0.512097 |
| Average | | | | | | 0.512106 |
| SD | | | | | | 0.000011 |

primary ion beam of 2 nA intensity was utilized to sputter the analytical spots of 25 to 30μm diameter on zircons in the polished mounts. A correction for common Pb was made on the basis of the measured $^{204}Pb$ and the model for common Pb compositions proposed by Stacey and Kramers (1975). The U-Pb data were reduced using the SQUID 2 and Isoplot 3 software (Ludwig, 2008). Uncertainties reported for individual analyses are at the $1\sigma$ level, and for pooled ages they are at the 95% confidence level.

For granite sample (IK-2) (table 3b) zircon U-Pb dates were obtained using a sensitive high-resolution ion microprobe (SHRIMP II) at the National Institute of Polar Research (NIPR), Tokyo, Japan. Analytical procedures for the U-Pb analysis were carried out following Horie and others (2012) and Hokada and others (2013). Zircons from each sample were mounted together with standards in an epoxy resin disc that was abraded and polished to obtain cross-sections through the grains. Prior to the U-Pb analyses the surfaces of grain mounts were washed with 2% HCl (ultrasonic cleaning-petroleum ether) to remove any lead contamination, and then coated with gold about 135Å thick. To determine the morphology and internal structure of individual grains and to determine the suitable analytical spots backscattered electron (BSE) and cathodoluminescence (CL) images were obtained using a scanning electron microscope (SEM; JEOL JSM-5900 LV) at the National Institute of Polar Research in Tokyo,

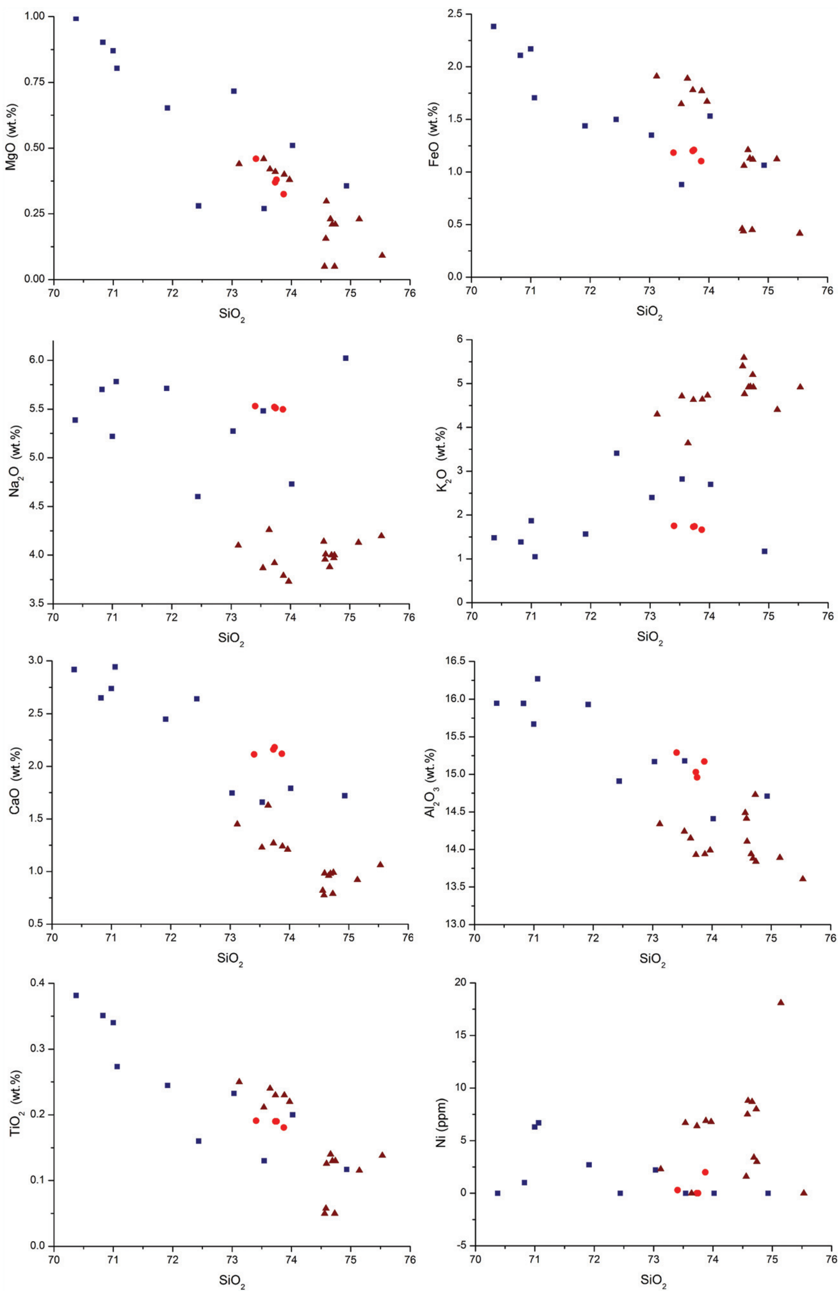


Fig. A2. Harker variation diagrams for TTGs and granites for major elements and Ni.

Japan. To obtain the SEM images a 0.2nA electron beam current and a 15kV acceleration voltage were used on the gold coating. An $O_2-$ primary ion beam of 1.6 to 2.7 nA intensity was utilized to sputter the analytical spot of 20 to 25um diameter (Köhler Ap.: 100–120 μm) on the zircons in the polished mount. TEMORA 2 ($^{206}$Pb/$^{238}$U age=416.8 Ma; Black and others, 2004) and 91500 (U concentration 81.2 ppm; Wiedenbeck and others, 1995) were used as calibration standard materials for the U-

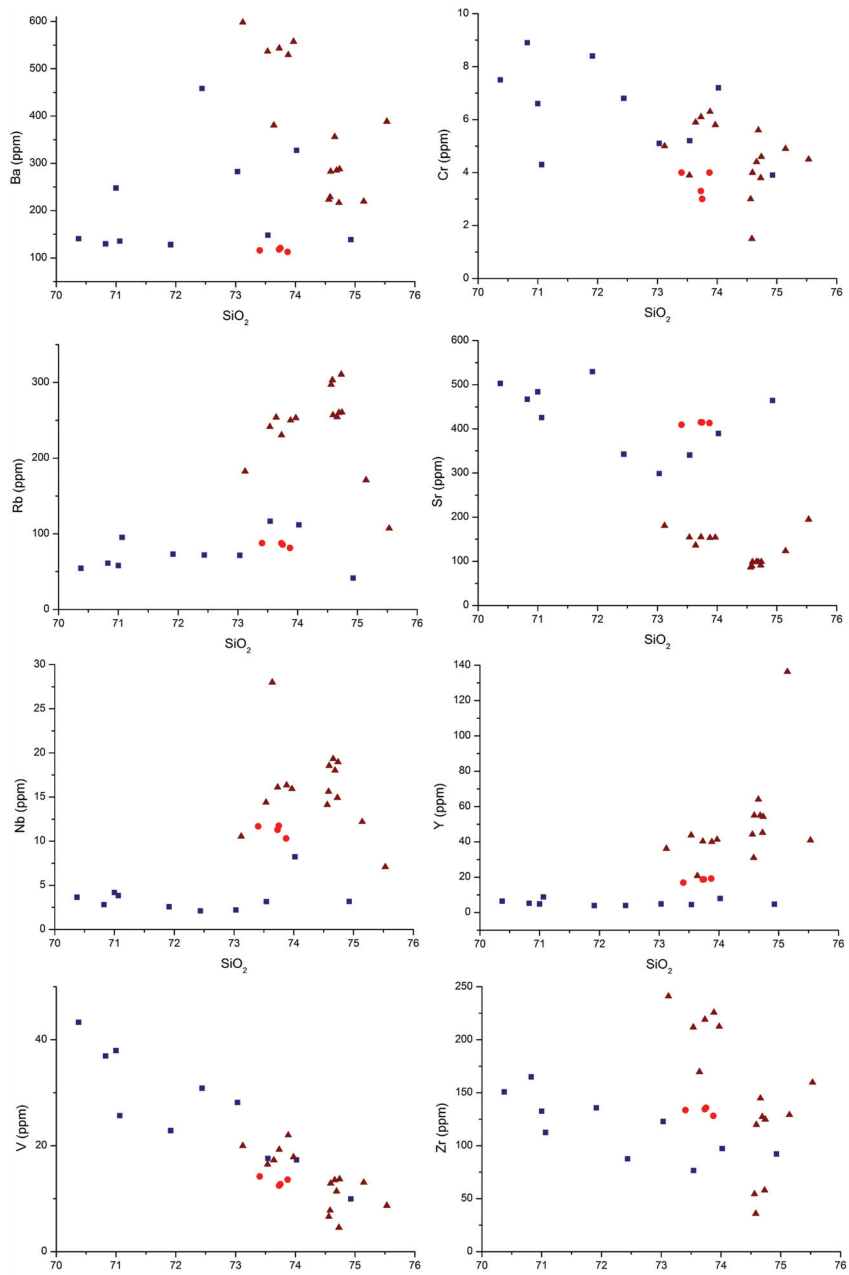


Fig. A3. Harker variation diagrams for TTGs and granites for trace elements.

Pb analysis and U concentration. FC1 (reference value: 1099.3 ± 0.3Ma; Paces and Miller, 1993) and OG-1 (reference value of Pb-Pb: 3465.4 ± 0.6; Stern and others, 2009) were used as additional standards. A correction for common Pb was made on the basis of the measured $^{204}$Pb and the model for common Pb compositions proposed by Stacey and Kramers (1975) for the bulk-crust Pb isotope composition model.

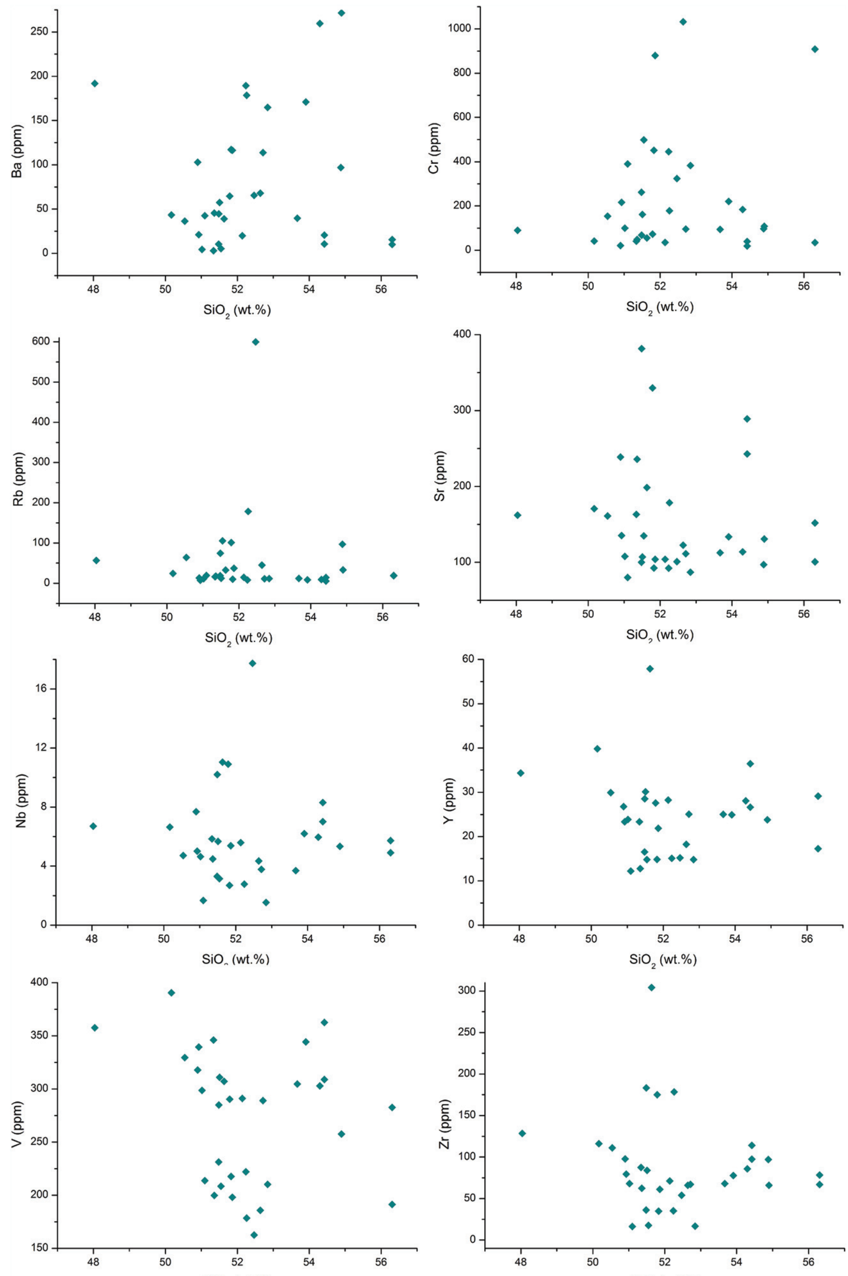


Fig. A4. Harker variation diagrams for amphibolites for major elements and Ni.

The U-Pb data were reduced in a manner similar to that described by Williams (1997), using the SQUID2 and Isoplot3 software. The pooled ages were calculated using the Isoplot/Ex software (Ludwig, 2008). Uncertainties reported for individual analyses are at the 1$\sigma$ level, and the error in the standard calibration was 0.16 to 0.33%.

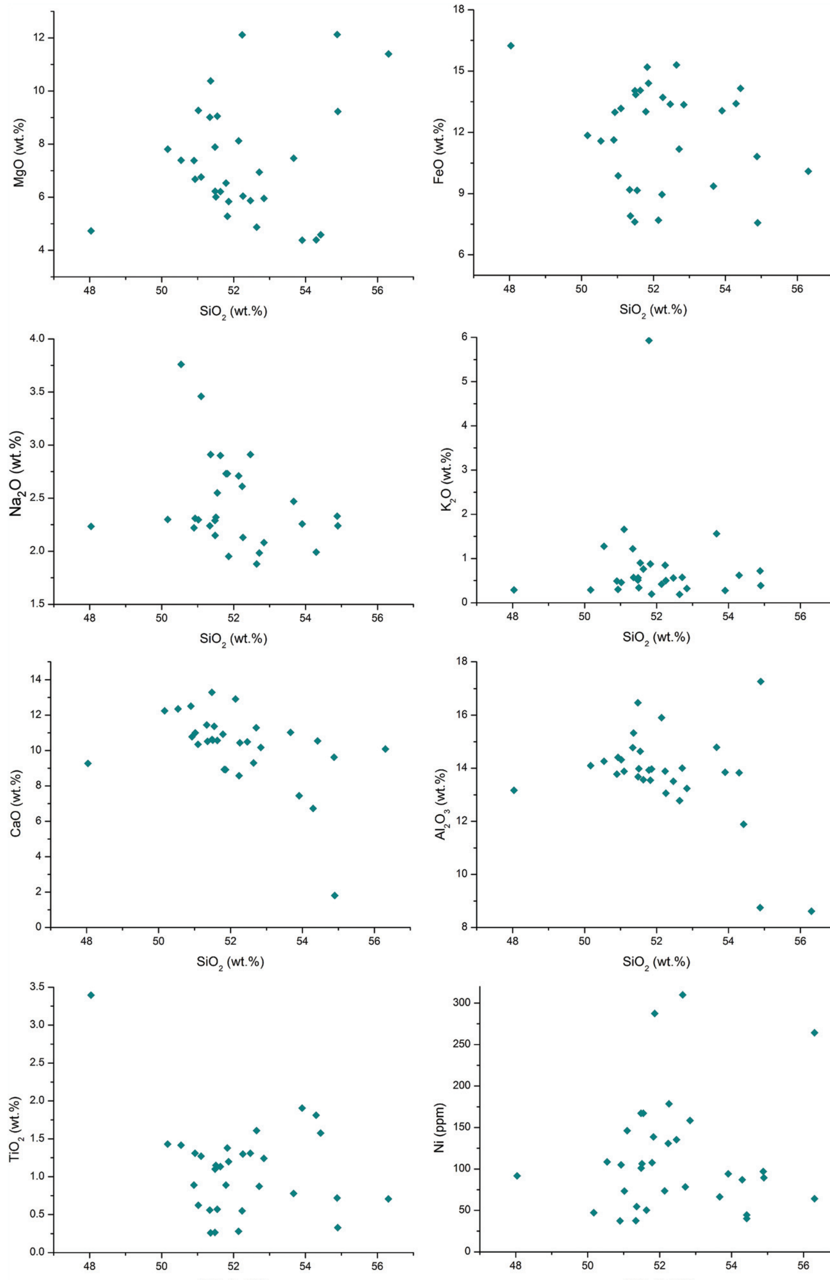


Fig. A5. Harker variation diagrams for amphibolites for trace elements.

### *Whole-Rock Sr and Nd Isotopic Analysis*

Isotopic determination of Sr and Nd for the 13 felsic and 10 amphibolite samples (table 4) (sample powders prepared at Niigata University) were made by Thermal Ionization Mass Spectrometry on a Finnigan MAT 262 mass spectrometer at Niigata University, Japan, following the procedures of Miyazaki and Shuto (1998). Based on

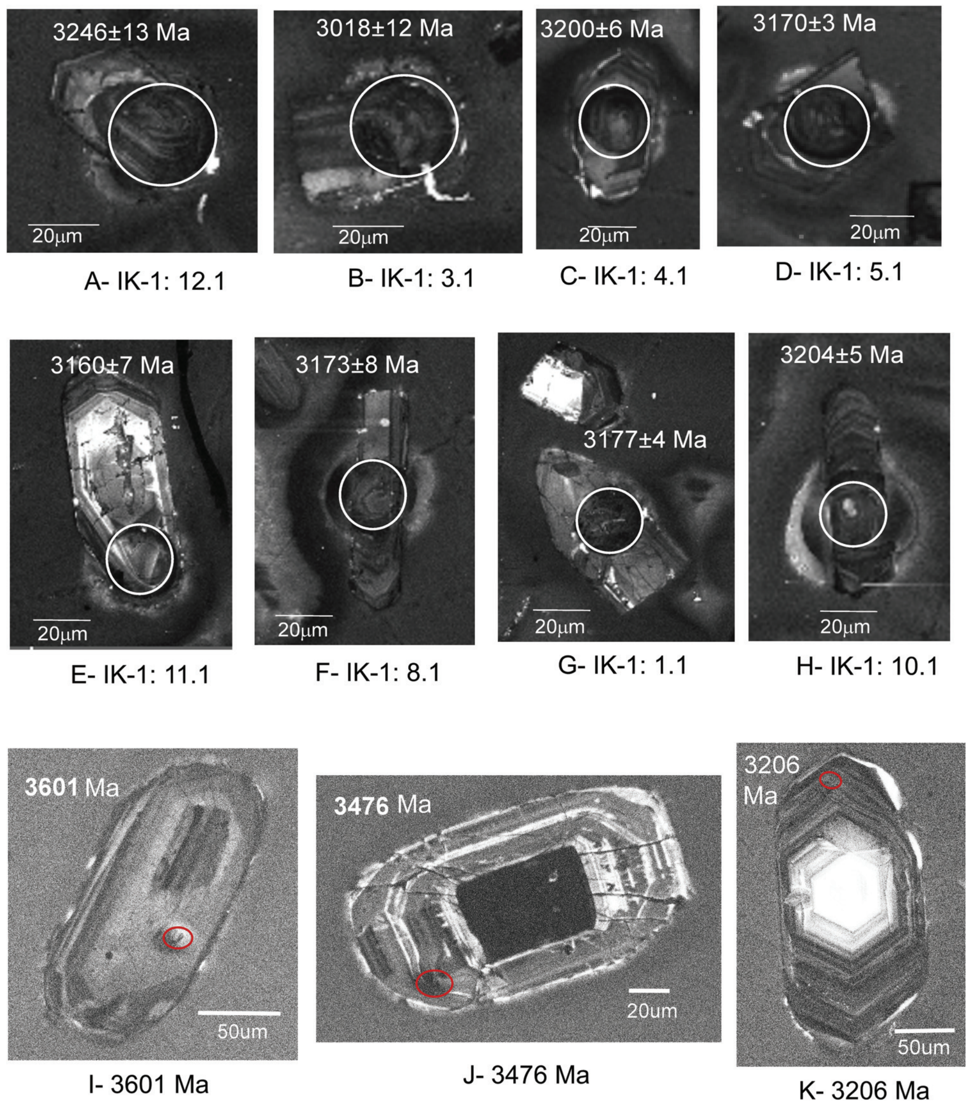


Fig. A6. CL images of zircons from TTG-I and granite showing internal morphology and textures A. TTG-I (sample IK-1), zircon CL images A to H are from sample IK-1 and images I, J, K are from other TTG-I sample (after Ishwar-Kumar and others, 2013) given here to show the zircon inherited ages.

mineralogical and chemical compositions such as major, trace and REE, powdered rocks samples ~0.05 g for TTG, 0.1 g for amphibolite, and 0.15 g for (IK-11, IK-19, IK-20) were digested in a mixed solution of $HCl+HClO_4+HNO_3+HF$ in a Teflon vessel (Kagami and others, 1987). Sr and Nd fractions were obtained by column separation using the methodology described by Miyazaki and Shuto (1998) and Kagami and others (1982, 1987). Powdered samples were decomposed in a sealed teflon vessel using a HF, HCl, $HNO_3$ and $HClO_4$ mixture. Extractions of Sr and Nd were carried out using different columns filled with a cation exchange resin (Dowex AG 50W-X8, 200–400 mesh). The extracted Sr and Nd were loaded onto Ta filaments with 2.5N

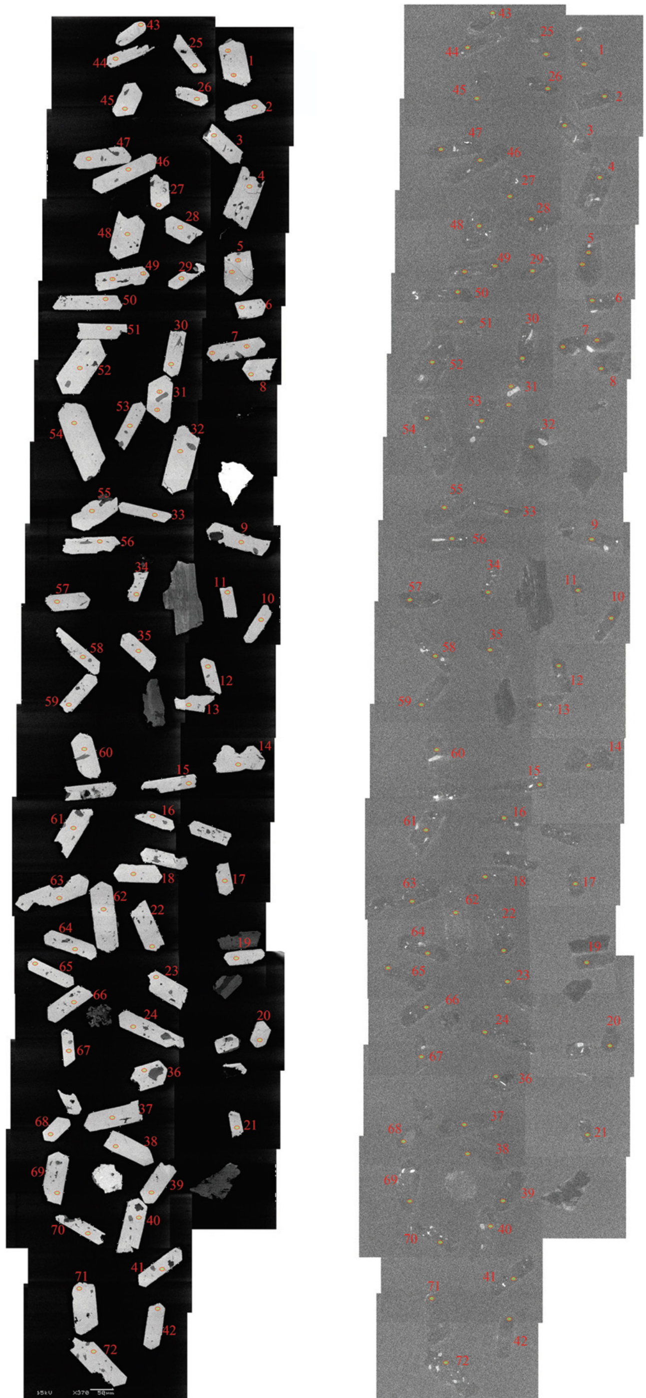

Fig. A7. BSE and CL images of zircons from granite (sample IK-2).

TABLE A5

*Zircon U-Pb and Oxygen isotopic compositions for IK-1 (TTG-I, 1512) and IK-2 (Granite, 1503) samples*

| Spot Name | U ppm | Th ppm | Pb* ppm | Th/U | % $^{206}Pb_c$ | $^{208}Pb^*/^{232}Th$ | ±1σ % | $^{206}Pb^*/^{238}U$ | ±1σ % | $^{207}Pb^*/^{235}U$ | ±1σ % | $^{207}Pb^*/^{206}Pb$ | ±1σ % | Dates (Ma) 208/232 | ± 1σ | 206/238 | ± 1σ | 207/235 | ± 1σ | 207/206 | ± 1σ | $\delta^{18}O_{SMOW}$ | 95% c.l. |
|---|---|---|---|---|---|---|---|---|---|---|---|---|---|---|---|---|---|---|---|---|---|---|---|
| *a. IK-1 (TTG-I)* | | | | | | | | | | | | | | | | | | | | | | | |
| 1512-1.1 | 329 | 70 | 153 | 0.22 | 0.27 | 0.159 | 2.5 | 0.54 | 1.1 | 18.7 | 1.1 | 0.250 | 0.31 | 2974 | 69 | 2791 | 25 | 3025 | 11 | 3184 | 5 | 5.95 | 0.24 |
| 1512-2.1 | 130 | 43 | 30 | 0.34 | 2.47 | 0.133 | 8.8 | 0.27 | 5.4 | 9.3 | 5.6 | 0.250 | 1.62 | 2516 | 206 | 1543 | 74 | 2371 | 50 | 3187 | 26 | 6.51 | 0.29 |
| 1512-3.1 | 209 | 70 | 111 | 0.34 | 0.13 | 0.184 | 4.1 | 0.62 | 1.4 | 21.5 | 1.5 | 0.251 | 0.55 | 3412 | 130 | 3118 | 35 | 3162 | 15 | 3190 | 9 | 5.30 | 0.27 |
| 1512-4.1 | 509 | 159 | 178 | 0.32 | 5.41 | 0.119 | 13.4 | 0.41 | 1.1 | 13.1 | 1.6 | 0.234 | 1.15 | 2267 | 285 | 2201 | 20 | 2688 | 15 | 3078 | 18 | 4.87 | 0.29 |
| 1512-5.1 | 741 | 12 | 151 | 0.02 | 2.67 | - | - | 0.24 | 3.0 | 7.1 | 3.3 | 0.217 | 1.25 | - | - | 1370 | 37 | 2123 | 29 | 2959 | 20 | 4.73 | 0.28 |
| 1512-6.1 | 637 | 174 | 145 | 0.28 | 1.90 | 0.114 | 2.7 | 0.26 | 1.5 | 8.3 | 1.6 | 0.227 | 0.48 | 2190 | 57 | 1513 | 20 | 2263 | 14 | 3032 | 8 | 4.40 | 0.36 |
| 1512-7.1 | 753 | 18 | 234 | 0.02 | 2.51 | 0.242 | 13.9 | 0.36 | 1.1 | 10.4 | 1.2 | 0.208 | 0.42 | 4372 | 538 | 1989 | 19 | 2469 | 11 | 2891 | 7 | 4.79 | 0.22 |
| 1512-8.1 | 310 | 134 | 162 | 0.45 | 0.61 | 0.183 | 3.1 | 0.61 | 1.1 | 21.2 | 1.3 | 0.253 | 0.70 | 3396 | 96 | 3058 | 27 | 3148 | 13 | 3206 | 11 | 4.83 | 0.36 |
| 1512-9.1 | 308 | 76 | 97 | 0.25 | 0.72 | 0.174 | 10.6 | 0.37 | 5.7 | 13.0 | 5.7 | 0.256 | 0.45 | 3240 | 315 | 2024 | 99 | 2681 | 52 | 3223 | 7 | 5.75 | 0.24 |
| 1512-10.1 | 427 | 6 | 125 | 0.02 | 0.90 | - | - | 0.34 | 3.2 | 11.0 | 3.2 | 0.234 | 0.39 | - | - | 1886 | 52 | 2521 | 29 | 3081 | 6 | 4.53 | 0.23 |
| 1512-11.1 | 306 | 21 | 146 | 0.07 | 0.19 | 0.169 | 5.4 | 0.56 | 1.1 | 19.4 | 1.1 | 0.253 | 0.29 | 3149 | 156 | 2853 | 25 | 3064 | 11 | 3206 | 5 | 5.05 | 0.31 |
| 1512-11.2 | 16 | 6 | 9 | 0.43 | 0.45 | 0.204 | 5.9 | 0.66 | 3.0 | 22.8 | 3.3 | 0.250 | 1.39 | 3747 | 202 | 3270 | 76 | 3217 | 31 | 3184 | 22 | 6.18 | 0.28 |
| 1512-12.1 | 364 | 137 | 160 | 0.39 | 0.27 | 0.182 | 2.8 | 0.51 | 1.1 | 18.0 | 1.2 | 0.254 | 0.36 | 3375 | 88 | 2666 | 24 | 2988 | 11 | 3212 | 6 | 5.97 | 0.20 |
| 1512-12.2 | 309 | 53 | 53 | 0.18 | 6.86 | 0.195 | 15.6 | 0.20 | 2.7 | 6.9 | 4.6 | 0.252 | 3.73 | 3601 | 508 | 1170 | 29 | 2100 | 40 | 3197 | 59 | 5.77 | 0.25 |
| 1512-12.3 | 243 | 44 | 108 | 0.19 | 0.41 | 0.179 | 3.5 | 0.52 | 1.7 | 18.1 | 1.7 | 0.254 | 0.40 | 3329 | 106 | 2683 | 37 | 2995 | 17 | 3211 | 6 | 6.06 | 0.29 |
| 1512-13.1 | 234 | 56 | 129 | 0.25 | 0.23 | 0.174 | 3.9 | 0.64 | 1.2 | 22.4 | 1.2 | 0.254 | 0.33 | 3248 | 118 | 3193 | 29 | 3202 | 12 | 3208 | 5 | 6.13 | 0.27 |
| 1512-14.1 | 375 | 146 | 217 | 0.40 | 0.33 | 0.169 | 2.0 | 0.67 | 1.1 | 28.0 | 1.1 | 0.301 | 0.22 | 3151 | 58 | 3324 | 28 | 3420 | 11 | 3476 | 3 | 5.19 | 0.29 |
| 1512-15.1 | 143 | 58 | 91 | 0.42 | 0.38 | 0.205 | 2.7 | 0.74 | 1.3 | 33.3 | 1.3 | 0.327 | 0.34 | 3764 | 93 | 3570 | 35 | 3590 | 13 | 3601 | 5 | 5.27 | 0.21 |
| 1512-16.1 | 464 | 1 | 204 | 0.00 | 0.07 | - | - | 0.51 | 1.6 | 16.8 | 1.6 | 0.239 | 0.22 | - | - | 2659 | 35 | 2925 | 15 | 3113 | 4 | 4.68 | 0.30 |
| 1512-16.2 | 433 | 87 | 242 | 0.21 | 0.05 | 0.178 | 3.8 | 0.65 | 1.2 | 22.8 | 1.2 | 0.254 | 0.20 | 3310 | 116 | 3228 | 31 | 3217 | 12 | 3211 | 3 | 6.06 | 0.27 |
| 1512-16.3 | 677 | 8 | 165 | 0.01 | 0.15 | 0.025 | 56.9 | 0.28 | 5.8 | 8.1 | 5.8 | 0.208 | 0.84 | 505 | 282 | 1613 | 82 | 2246 | 51 | 2887 | 14 | 2.35 | 0.31 |
| 1512-17.1 | 423 | 7 | 127 | 0.02 | 8.06 | - | - | 0.35 | 1.5 | 11.4 | 2.1 | 0.236 | 1.51 | - | - | 1938 | 25 | 2558 | 20 | 3094 | 24 | 4.14 | 0.25 |
| 1512-18.1 | | | | | | | | | | | | | | | | | | | | | | 7.12 | 0.21 |
| 1512-19.1 | | | | | | | | | | | | | | | | | | | | | | 4.63 | 0.32 |
| 1512-20.1 | 417 | 203 | 233 | 0.50 | 0.01 | 0.165 | 1.2 | 0.65 | 1.0 | 27.0 | 1.0 | 0.300 | 0.18 | 3079 | 34 | 3230 | 26 | 3382 | 10 | 3473 | 3 | 4.11 | 0.33 |
| 1512-20.2 | 744 | 424 | 197 | 0.59 | 0.09 | 0.081 | 1.4 | 0.31 | 1.0 | 9.0 | 1.0 | 0.213 | 0.23 | 1572 | 21 | 1732 | 15 | 2342 | 9 | 2927 | 4 | 3.95 | 0.35 |
| 1512-21.1 | 195 | 93 | 100 | 0.49 | 0.07 | 0.146 | 1.5 | 0.60 | 1.2 | 20.8 | 1.2 | 0.253 | 0.31 | 2746 | 39 | 3012 | 28 | 3128 | 12 | 3203 | 5 | 5.36 | 0.24 |
| 1512-22.1 | 90 | 27 | 47 | 0.31 | 0.06 | 0.166 | 2.8 | 0.61 | 1.4 | 21.2 | 1.5 | 0.253 | 0.45 | 3098 | 79 | 3066 | 35 | 3150 | 14 | 3204 | 7 | 5.36 | 0.29 |
| 1512-23.1 | 517 | 90 | 203 | 0.18 | 0.61 | 0.115 | 4.6 | 0.46 | 1.0 | 15.0 | 1.1 | 0.237 | 0.35 | 2198 | 96 | 2426 | 21 | 2812 | 10 | 3103 | 6 | 4.97 | 0.32 |
| 1512-24.1 | 434 | 142 | 181 | 0.34 | 0.65 | 0.127 | 4.6 | 0.48 | 1.0 | 15.8 | 1.2 | 0.236 | 0.58 | 2413 | 104 | 2545 | 22 | 2862 | 11 | 3094 | 9 | 4.44 | 0.19 |

TABLE A5

*(continued)*

| Spot Name | U ppm | Th ppm | Pb* ppm | Th/U | % $^{206}Pb_c$ | $^{208}Pb^*/^{232}Th$ | ±1σ % | $^{206}Pb^*/^{238}U$ | ±1σ % | $^{207}Pb^*/^{235}U$ | ±1σ % | $^{207}Pb^*/^{206}Pb$ | ±1σ % | Dates (Ma) 208/232 | ± 1σ | 206/238 | ± 1σ | 207/235 | ± 1σ | 207/206 | ± 1σ | $\delta^{18}O_{SMOW}$ | 95% c.l. |
|---|---|---|---|---|---|---|---|---|---|---|---|---|---|---|---|---|---|---|---|---|---|---|---|
| *b. IK-2 (Granite)* | | | | | | | | | | | | | | | | | | | | | | | |
| 1503-1.1 | 956 | 190 | 321 | 0.20 | 0.08 | 0.083 | 3.3 | 0.391 | 1.6 | 10.7 | 1.7 | 0.198 | 0.6 | 1615 | 52 | 2129 | 29 | 2497 | 16 | 2812 | 10 | 2.96 | 0.34 |
| 1503-1.2 | 1023 | 157 | 274 | 0.16 | 0.21 | 0.064 | 4.8 | 0.311 | 1.6 | 7.9 | 1.7 | 0.183 | 0.7 | 1260 | 58 | 1748 | 24 | 2215 | 15 | 2681 | 12 | 2.87 | 0.32 |
| 1503-2.1 | 3220 | 2466 | 353 | 0.79 | 2.46 | 0.044 | 2.7 | 0.128 | 1.1 | 1.9 | 2.6 | 0.108 | 2.4 | 867 | 23 | 775 | 8 | 1083 | 17 | 1770 | 43 | 3.21 | 0.24 |
| 1503-3.1 | 1418 | 1483 | 438 | 1.08 | 7.62 | 0.075 | 9.5 | 0.360 | 1.2 | 9.6 | 4.7 | 0.193 | 4.5 | 1460 | 133 | 1982 | 21 | 2396 | 42 | 2769 | 74 | 1.46 | 0.96 |
| 1503-4.1 | 1268 | 124 | 284 | 0.10 | 0.34 | 0.102 | 9.3 | 0.260 | 1.5 | 5.6 | 1.9 | 0.157 | 1.1 | 1954 | 173 | 1492 | 20 | 1923 | 16 | 2426 | 19 | 1.62 | 0.25 |
| 1503-5.1 | 1811 | 1055 | 250 | 0.60 | 4.03 | 0.048 | 8.7 | 0.160 | 1.5 | 2.7 | 5.1 | 0.121 | 4.9 | 946 | 80 | 959 | 13 | 1320 | 37 | 1965 | 88 | 5.10 | 0.27 |
| 1503-5.2 | 2155 | 1196 | 270 | 0.57 | 7.37 | 0.041 | 7.8 | 0.146 | 1.3 | 2.4 | 4.0 | 0.122 | 3.7 | 811 | 62 | 878 | 11 | 1256 | 28 | 1980 | 66 | 3.26 | 0.24 |
| 1503-6.1 | 1751 | 1331 | 295 | 0.79 | 0.28 | 0.052 | 2.4 | 0.196 | 1.3 | 3.3 | 1.9 | 0.122 | 1.3 | 1034 | 25 | 1153 | 14 | 1479 | 14 | 1984 | 23 | 0.69 | 0.23 |
| 1503-7.1 | 2036 | 601 | 371 | 0.30 | 0.67 | 0.069 | 3.7 | 0.212 | 1.3 | 4.2 | 1.7 | 0.142 | 1.1 | 1342 | 48 | 1240 | 14 | 1666 | 14 | 2253 | 19 | 1.54 | 0.28 |
| 1503-7.2 | 2370 | 2565 | 291 | 1.12 | 0.83 | 0.039 | 2.1 | 0.143 | 1.2 | 1.9 | 2.3 | 0.097 | 1.9 | 773 | 16 | 862 | 10 | 1085 | 15 | 1564 | 36 | 1.41 | 0.24 |
| 1503-8.1 | 3461 | 227 | 289 | 0.07 | 1.73 | 0.050 | 20.9 | 0.097 | 1.4 | 1.1 | 3.9 | 0.084 | 3.6 | 986 | 200 | 597 | 8 | 765 | 21 | 1292 | 70 | 3.99 | 0.24 |
| 1503-9.1 | 1514 | 72 | 295 | 0.05 | 0.26 | 0.060 | 13.9 | 0.227 | 1.6 | 4.9 | 1.9 | 0.155 | 1.1 | 1175 | 158 | 1318 | 19 | 1795 | 16 | 2405 | 19 | 0.05 | 0.34 |
| 1503-10.1 | 2515 | 1114 | 421 | 0.46 | 3.49 | 0.053 | 12.9 | 0.195 | 1.5 | 3.2 | 5.4 | 0.119 | 5.2 | 1047 | 131 | 1147 | 16 | 1457 | 41 | 1945 | 93 | 1.56 | 0.37 |
| 1503-11.1 | 2812 | 375 | 374 | 0.14 | 4.53 | 0.084 | 13.3 | 0.155 | 1.3 | 2.9 | 3.1 | 0.135 | 2.9 | 1624 | 206 | 929 | 11 | 1376 | 23 | 2159 | 50 | 5.41 | 0.30 |
| 1503-12.1 | 1638 | 1113 | 268 | 0.70 | 0.64 | 0.053 | 2.7 | 0.190 | 1.3 | 3.2 | 2.1 | 0.121 | 1.7 | 1035 | 27 | 1124 | 14 | 1448 | 16 | 1964 | 30 | 2.02 | 0.20 |
| 1503-13.1 | 2829 | 1760 | 540 | 0.64 | 0.69 | 0.063 | 2.1 | 0.222 | 1.2 | 4.3 | 1.8 | 0.141 | 1.3 | 1236 | 25 | 1293 | 14 | 1695 | 14 | 2237 | 22 | 0.56 | 0.25 |
| 1503-14.1 | 1161 | 109 | 251 | 0.10 | 0.42 | 0.084 | 7.7 | 0.251 | 1.8 | 5.8 | 2.1 | 0.166 | 1.1 | 1636 | 121 | 1446 | 24 | 1942 | 18 | 2523 | 18 | 4.05 | 0.21 |
| 1503-15.1 | 1880 | 797 | 338 | 0.44 | 0.28 | 0.060 | 3.3 | 0.209 | 2.4 | 4.2 | 2.5 | 0.145 | 0.6 | 1187 | 38 | 1224 | 27 | 1669 | 20 | 2286 | 10 | 0.47 | 0.25 |
| 1503-16.1 | 1908 | 1226 | 269 | 0.66 | 0.59 | 0.048 | 3.6 | 0.164 | 1.6 | 2.6 | 2.6 | 0.117 | 2.0 | 944 | 33 | 981 | 15 | 1314 | 19 | 1908 | 37 | 0.90 | 0.30 |
| 1503-17.1 | 2429 | 1482 | 357 | 0.63 | 3.51 | 0.055 | 5.7 | 0.171 | 1.6 | 2.5 | 4.4 | 0.106 | 4.1 | 1087 | 60 | 1019 | 15 | 1274 | 31 | 1734 | 75 | 2.20 | 0.22 |
| 1503-18.1 | 1159 | 391 | 274 | 0.35 | 0.16 | 0.073 | 3.4 | 0.276 | 1.9 | 6.4 | 2.1 | 0.168 | 0.9 | 1417 | 47 | 1570 | 26 | 2032 | 18 | 2541 | 16 | 1.31 | 0.23 |
| 1503-19.1 | 2861 | 2579 | 389 | 0.93 | 2.06 | 0.048 | 3.1 | 0.158 | 1.4 | 2.9 | 2.7 | 0.133 | 2.3 | 957 | 29 | 946 | 13 | 1379 | 20 | 2132 | 40 | 3.74 | 0.20 |
| 1503-20.1 | 2155 | 1837 | 481 | 0.88 | 2.70 | 0.081 | 4.0 | 0.260 | 1.6 | 5.4 | 3.1 | 0.151 | 2.6 | 1566 | 60 | 1490 | 21 | 1886 | 26 | 2355 | 45 | 2.20 | 0.23 |
| 1503-21.1 | 1978 | 1145 | 328 | 0.60 | 3.34 | 0.057 | 7.7 | 0.193 | 1.8 | 3.0 | 4.7 | 0.113 | 4.4 | 1127 | 84 | 1137 | 19 | 1411 | 36 | 1854 | 80 | 1.86 | 0.23 |
| 1503-22.1 | 2577 | 2131 | 377 | 0.85 | 1.40 | 0.049 | 3.0 | 0.170 | 1.5 | 2.9 | 2.4 | 0.125 | 1.9 | 961 | 28 | 1014 | 14 | 1390 | 18 | 2026 | 34 | 1.71 | 0.56 |
| 1503-23.1 | 1064 | 79 | 247 | 0.08 | 0.27 | 0.070 | 9.2 | 0.271 | 2.0 | 6.3 | 2.2 | 0.168 | 1.0 | 1374 | 122 | 1545 | 27 | 2012 | 19 | 2533 | 17 | 3.54 | 0.27 |
| 1503-24.1 | 2649 | 2220 | 534 | 0.87 | 0.15 | 0.063 | 1.9 | 0.234 | 1.4 | 4.9 | 1.6 | 0.151 | 0.7 | 1235 | 23 | 1358 | 17 | 1801 | 13 | 2362 | 12 | 0.78 | 0.22 |
| 1503-25.1 | 1400 | 191 | 321 | 0.14 | 1.44 | 0.104 | 15.5 | 0.267 | 2.0 | 5.7 | 3.0 | 0.156 | 2.3 | 2003 | 293 | 1524 | 27 | 1938 | 26 | 2415 | 39 | 1.08 | 0.29 |
| 1503-26.1 | 3234 | 2065 | 333 | 0.66 | 7.60 | 0.045 | 6.9 | 0.120 | 1.6 | 2.3 | 4.7 | 0.141 | 4.5 | 890 | 60 | 730 | 11 | 1219 | 33 | 2234 | 78 | 3.28 | 0.25 |
| 1503-27.1 | 3593 | 1997 | 449 | 0.57 | 3.77 | 0.043 | 5.8 | 0.146 | 1.4 | 2.6 | 3.5 | 0.128 | 3.2 | 852 | 48 | 876 | 11 | 1294 | 25 | 2075 | 57 | 2.23 | 0.22 |
| 1503-28.1 | 2356 | 2080 | 411 | 0.91 | 0.58 | 0.055 | 2.6 | 0.203 | 1.5 | 3.9 | 2.3 | 0.138 | 1.7 | 1078 | 27 | 1191 | 16 | 1607 | 18 | 2204 | 29 | 1.98 | 0.25 |
| 1503-29.1 | 1414 | 772 | 240 | 0.56 | 0.54 | 0.060 | 3.1 | 0.198 | 1.9 | 3.1 | 3.0 | 0.114 | 2.4 | 1169 | 35 | 1164 | 20 | 1435 | 23 | 1864 | 42 | 1.41 | 0.35 |

TABLE A5
*(continued)*

| Spot Name | U ppm | Th ppm | Pb* ppm | Th/U | % $^{206}Pb_c$ | $^{208}Pb^*/^{232}Th$ | ±1σ % | $^{206}Pb^*/^{238}U$ | ±1σ % | $^{207}Pb^*/^{235}U$ | ±1σ % | $^{207}Pb^*/^{206}Pb$ | ±1σ % | Dates (Ma) 208/232 | ± 1σ | 206/238 | ± 1σ | 207/235 | ± 1σ | 207/206 | ± 1σ | $\delta^{18}O_{SMOW}$ | 95% c.l. |
|---|---|---|---|---|---|---|---|---|---|---|---|---|---|---|---|---|---|---|---|---|---|---|---|
| *b. IK-2 (Granite)* | | | | | | | | | | | | | | | | | | | | | | | |
| 1503-30.1 | 3194 | 2409 | 285 | 0.78 | 1.41 | 0.035 | 3.0 | 0.104 | 1.4 | 1.4 | 3.0 | 0.098 | 2.6 | 690 | 21 | 637 | 8 | 887 | 18 | 1577 | 50 | 5.44 | 0.27 |
| 1503-31.1 | 1250 | 696 | 440 | 0.58 | 0.97 | 0.115 | 4.0 | 0.410 | 1.9 | 11.2 | 2.2 | 0.198 | 1.1 | 2199 | 82 | 2216 | 35 | 2538 | 20 | 2806 | 19 | 1.77 | 0.24 |
| 1503-31.2 | 1995 | 2370 | 525 | 1.23 | 1.99 | 0.069 | 3.0 | 0.307 | 1.6 | 7.7 | 2.1 | 0.183 | 1.4 | 1350 | 39 | 1724 | 24 | 2202 | 19 | 2683 | 23 | 1.47 | 0.23 |
| 1503-32.1 | 2339 | 1570 | 360 | 0.69 | 0.99 | 0.051 | 3.2 | 0.179 | 1.5 | 3.5 | 2.2 | 0.143 | 1.5 | 1008 | 31 | 1062 | 15 | 1532 | 17 | 2260 | 26 | 3.38 | 0.28 |
| 1503-33.1 | 1667 | 1649 | 301 | 1.02 | 1.32 | 0.054 | 3.7 | 0.210 | 1.7 | 4.1 | 2.9 | 0.142 | 2.3 | 1069 | 38 | 1230 | 19 | 1655 | 23 | 2246 | 39 | 1.92 | 0.27 |
| 1503-34.1 | 2304 | 1778 | 440 | 0.80 | 0.94 | 0.066 | 2.8 | 0.222 | 1.6 | 4.5 | 2.1 | 0.145 | 1.4 | 1295 | 35 | 1295 | 19 | 1723 | 18 | 2291 | 24 | 1.11 | 0.24 |
| 1503-35.1 | 2185 | 1816 | 322 | 0.86 | 0.24 | 0.049 | 2.3 | 0.172 | 1.5 | 2.6 | 1.9 | 0.108 | 1.2 | 969 | 21 | 1021 | 15 | 1287 | 14 | 1762 | 21 | 0.87 | 0.28 |
| 1503-36.1 | 1772 | 1131 | 255 | 0.66 | 0.26 | 0.047 | 2.8 | 0.167 | 1.7 | 2.6 | 1.9 | 0.111 | 0.8 | 922 | 25 | 997 | 16 | 1287 | 14 | 1809 | 15 | 1.57 | 0.26 |
| 1503-37.1 | 1011 | 490 | 267 | 0.50 | 1.45 | 0.087 | 13.2 | 0.308 | 2.5 | 7.5 | 4.6 | 0.177 | 3.9 | 1689 | 213 | 1731 | 37 | 2175 | 41 | 2625 | 65 | 1.67 | 0.28 |
| 1503-38.1 | 1655 | 1189 | 249 | 0.74 | 3.54 | 0.063 | 7.9 | 0.175 | 2.0 | 3.1 | 7.3 | 0.130 | 7.1 | 1231 | 95 | 1039 | 19 | 1442 | 55 | 2100 | 124 | 1.07 | 0.23 |
| 1503-39.1 | 2350 | 1947 | 410 | 0.86 | 2.42 | 0.057 | 10.4 | 0.203 | 7.5 | 3.4 | 12.0 | 0.123 | 9.4 | 1114 | 113 | 1191 | 82 | 1513 | 90 | 1997 | 167 | 2.06 | 0.27 |
| 1503-40.1 | 634 | 601 | 227 | 0.98 | 0.52 | 0.117 | 3.6 | 0.416 | 2.5 | 11.4 | 2.7 | 0.198 | 1.1 | 2244 | 76 | 2244 | 47 | 2555 | 25 | 2813 | 19 | 3.73 | 0.36 |
| 1503-42.1 | 2949 | 2268 | 736 | 0.79 | 1.18 | 0.079 | 3.0 | 0.290 | 1.5 | 7.0 | 1.9 | 0.174 | 1.2 | 1532 | 45 | 1644 | 22 | 2109 | 17 | 2599 | 21 | 3.78 | 0.22 |
| 1503-43.1 | 858 | 263 | 67 | 0.32 | 0.87 | 0.039 | 8.9 | 0.090 | 2.7 | 0.8 | 7.5 | 0.063 | 7.0 | 780 | 68 | 558 | 14 | 587 | 33 | 698 | 148 | 7.84 | 0.35 |
| 1503-44.1 | 2528 | 791 | 502 | 0.32 | 0.74 | 0.067 | 5.4 | 0.231 | 1.5 | 4.9 | 1.9 | 0.153 | 1.1 | 1304 | 69 | 1341 | 19 | 1797 | 16 | 2376 | 18 | 1.90 | 0.33 |
| 1503-45.1 | 1444 | 763 | 304 | 0.55 | 1.18 | 0.070 | 4.0 | 0.245 | 2.0 | 5.0 | 2.5 | 0.147 | 1.6 | 1373 | 53 | 1414 | 25 | 1817 | 21 | 2315 | 27 | 0.77 | 0.24 |
| 1503-46.1 | 2648 | 3116 | 485 | 1.22 | 0.30 | 0.057 | 2.1 | 0.213 | 1.6 | 3.9 | 1.9 | 0.131 | 1.0 | 1118 | 23 | 1246 | 18 | 1604 | 15 | 2113 | 18 | 0.77 | 0.23 |
| 1503-47.1 | 1950 | 1044 | 411 | 0.55 | 1.48 | 0.087 | 3.9 | 0.245 | 1.7 | 5.3 | 2.4 | 0.158 | 1.7 | 1692 | 63 | 1414 | 21 | 1873 | 20 | 2430 | 29 | 1.38 | 0.24 |
| 1503-48.1 | 1624 | 105 | 246 | 0.07 | 0.70 | 0.099 | 16.8 | 0.176 | 1.8 | 3.0 | 2.9 | 0.123 | 2.3 | 1910 | 304 | 1047 | 17 | 1404 | 22 | 1997 | 40 | 1.01 | 0.22 |
| 1503-49.1 | 1986 | 399 | 335 | 0.21 | 2.31 | 0.066 | 12.6 | 0.196 | 1.8 | 3.7 | 3.1 | 0.138 | 2.6 | 1299 | 157 | 1156 | 19 | 1582 | 25 | 2207 | 45 | 2.91 | 0.28 |
| 1503-49.2 | 1164 | 922 | 232 | 0.82 | 1.08 | 0.055 | 4.7 | 0.232 | 2.0 | 4.8 | 2.9 | 0.150 | 2.1 | 1079 | 49 | 1347 | 25 | 1783 | 24 | 2341 | 36 | 0.71 | 0.28 |
| 1503-50.1 | 1372 | 1422 | 261 | 1.07 | 0.53 | 0.062 | 3.2 | 0.222 | 1.9 | 4.1 | 2.2 | 0.135 | 1.3 | 1219 | 37 | 1292 | 22 | 1663 | 18 | 2170 | 22 | 2.14 | 0.24 |
| 1503-51.1 | 1405 | 978 | 258 | 0.72 | 0.48 | 0.057 | 3.0 | 0.213 | 1.8 | 4.1 | 2.2 | 0.141 | 1.3 | 1118 | 32 | 1247 | 21 | 1662 | 18 | 2236 | 22 | 1.01 | 0.23 |
| 1503-52.1 | 1142 | 98 | 305 | 0.09 | 0.58 | 0.075 | 22.2 | 0.310 | 2.0 | 7.7 | 2.4 | 0.179 | 1.3 | 1464 | 311 | 1743 | 30 | 2192 | 21 | 2644 | 22 | 1.91 | 0.23 |
| 1503-53.1 | 1657 | 1433 | 357 | 0.89 | 2.66 | 0.062 | 4.9 | 0.251 | 1.8 | 5.4 | 3.0 | 0.155 | 2.5 | 1223 | 58 | 1444 | 23 | 1882 | 26 | 2407 | 42 | 0.87 | 0.24 |
| 1503-54.1 | 4584 | 623 | 1456 | 0.14 | 0.71 | 0.197 | 3.0 | 0.370 | 1.2 | 10.1 | 1.3 | 0.199 | 0.5 | 3640 | 101 | 2028 | 21 | 2448 | 12 | 2818 | 8 | 1.37 | 0.20 |
| 1503-55.1 | 1109 | 225 | 246 | 0.21 | 0.40 | 0.065 | 10.3 | 0.258 | 2.0 | 5.7 | 2.5 | 0.161 | 1.5 | 1276 | 127 | 1479 | 26 | 1936 | 22 | 2468 | 26 | 1.05 | 0.24 |
| 1503-56.1 | 1645 | 743 | 263 | 0.47 | 6.07 | 0.049 | 12.7 | 0.186 | 1.8 | 2.9 | 5.8 | 0.114 | 5.5 | 962 | 119 | 1101 | 19 | 1391 | 43 | 1869 | 99 | 1.32 | 0.27 |
| 1503-57.1 | 1390 | 318 | 283 | 0.24 | 1.27 | 0.091 | 8.1 | 0.237 | 1.8 | 4.8 | 2.7 | 0.145 | 2.0 | 1757 | 136 | 1371 | 23 | 1776 | 23 | 2293 | 35 | 1.73 | 0.21 |
| 1503-58.1 | 2795 | 3312 | 247 | 1.22 | 2.72 | 0.037 | 2.9 | 0.103 | 1.5 | 1.3 | 4.8 | 0.089 | 4.5 | 739 | 21 | 631 | 9 | 827 | 27 | 1398 | 87 | 2.40 | 0.33 |
| 1503-59.1 | 1046 | 278 | 239 | 0.27 | 0.26 | 0.073 | 4.1 | 0.266 | 2.0 | 6.2 | 2.2 | 0.169 | 1.0 | 1415 | 56 | 1520 | 27 | 2003 | 19 | 2545 | 17 | 1.08 | 0.21 |
| 1503-60.1 | 858 | 33 | 417 | 0.04 | 0.29 | 0.209 | 11.0 | 0.566 | 2.2 | 16.5 | 2.2 | 0.212 | 0.4 | 3828 | 379 | 2892 | 51 | 2907 | 21 | 2918 | 7 | 2.08 | 0.20 |

TABLE A5

*(continued)*

| Spot Name | U ppm | Th ppm | Pb* ppm | Th/U | % $^{206}Pb_c$ | $^{208}Pb^*/^{232}Th$ | ±1σ % | $^{206}Pb^*/^{238}U$ | ±1σ % | $^{207}Pb^*/^{235}U$ | ±1σ % | $^{207}Pb^*/^{206}Pb$ | ±1σ % | Dates (Ma) 208/232 | ± 1σ | 206/238 | ± 1σ | 207/235 | ± 1σ | 207/206 | ± 1σ | $\delta^{18}O_{SMOW}$ | 95% c.l. |
|---|---|---|---|---|---|---|---|---|---|---|---|---|---|---|---|---|---|---|---|---|---|---|---|
| *b. IK-2 (Granite)* | | | | | | | | | | | | | | | | | | | | | | | |
| 1503-30.1 | 3194 | 2409 | 285 | 0.78 | 1.41 | 0.035 | 3.0 | 0.104 | 1.4 | 1.4 | 3.0 | 0.098 | 2.6 | 690 | 21 | 637 | 8 | 887 | 18 | 1577 | 50 | 5.44 | 0.27 |
| 1503-61.1 | 1148 | 884 | 389 | 0.80 | 1.35 | 0.102 | 3.9 | 0.395 | 2.0 | 10.5 | 2.5 | 0.193 | 1.4 | 1955 | 72 | 2145 | 37 | 2480 | 23 | 2768 | 22 | 1.33 | 0.31 |
| 1503-62.1 | 1420 | 1208 | 454 | 0.88 | 1.84 | 0.089 | 3.7 | 0.372 | 1.8 | 10.2 | 2.3 | 0.200 | 1.3 | 1732 | 62 | 2038 | 32 | 2456 | 21 | 2823 | 22 | 2.99 | 0.22 |
| 1503-63.1 | 1469 | 953 | 237 | 0.67 | 0.63 | 0.055 | 4.2 | 0.188 | 1.8 | 3.0 | 2.4 | 0.115 | 1.5 | 1084 | 44 | 1110 | 19 | 1401 | 18 | 1877 | 28 | 0.67 | 0.25 |
| 1503-64.1 | 1866 | 598 | 344 | 0.33 | 2.16 | 0.073 | 7.2 | 0.215 | 1.7 | 3.9 | 2.8 | 0.133 | 2.2 | 1419 | 98 | 1255 | 19 | 1620 | 22 | 2135 | 39 | -0.06 | 0.28 |
| 1503-65.1 | 1800 | 1337 | 319 | 0.77 | 3.08 | 0.063 | 4.7 | 0.206 | 1.7 | 3.5 | 3.6 | 0.123 | 3.2 | 1227 | 56 | 1209 | 19 | 1528 | 28 | 2002 | 57 | 0.05 | 0.37 |
| 1503-66.1 | 1695 | 394 | 309 | 0.24 | 0.81 | 0.092 | 6.0 | 0.212 | 1.7 | 4.2 | 2.4 | 0.144 | 1.6 | 1782 | 102 | 1241 | 20 | 1678 | 19 | 2279 | 27 | 1.71 | 0.24 |
| 1503-67.1 | 1253 | 210 | 231 | 0.17 | 0.25 | 0.046 | 6.3 | 0.214 | 1.9 | 4.4 | 2.2 | 0.150 | 1.2 | 907 | 56 | 1252 | 21 | 1717 | 18 | 2343 | 20 | 1.29 | 0.26 |
| 1503-69.1 | 2029 | 1678 | 359 | 0.85 | 2.49 | 0.064 | 4.0 | 0.206 | 1.7 | 3.7 | 3.2 | 0.131 | 2.8 | 1257 | 48 | 1207 | 18 | 1578 | 25 | 2118 | 48 | 1.74 | 0.24 |
| 1503-70.1 | 1841 | 1318 | 367 | 0.74 | 0.67 | 0.062 | 3.3 | 0.232 | 1.7 | 4.6 | 2.2 | 0.145 | 1.5 | 1222 | 39 | 1344 | 20 | 1758 | 19 | 2292 | 26 | 0.31 | 0.21 |
| 1503-71.1 | 1167 | 95 | 241 | 0.08 | 0.50 | 0.061 | 11.7 | 0.241 | 1.9 | 5.2 | 2.3 | 0.158 | 1.2 | 1205 | 137 | 1390 | 24 | 1858 | 19 | 2432 | 20 | 1.57 | 0.35 |
| 1503-72.1 | 1521 | 1565 | 233 | 1.06 | 0.50 | 0.051 | 2.6 | 0.178 | 1.8 | 2.7 | 2.4 | 0.109 | 1.5 | 1010 | 25 | 1058 | 18 | 1320 | 17 | 1776 | 28 | 1.31 | 0.25 |

HCl and 2.5N $HNO_3$, respectively. The measured Sr and Nd isotope ratios were normalized to $^{86}Sr/^{88}Sr$ = 0.1194 and $^{146}Nd/^{144}Nd$ = 0.7219, respectively. The standard value (NIST 987 for Sr and JNdi-1 for Nd) during this study was $^{87}Sr/^{86}Sr$ =0.710251 $\pm$0.000033 ($2\sigma$, n=15). $^{143}Nd/^{144}Nd$ = 0.512106 $\pm$0.000022 ($2\sigma$, n=8) were measured (The values of standard reference material are given in Appendix table A4), and analytical values were corrected using the values reported in Miyazaki and Shuto (1998). The measured values for the reference materials are given in Appendix table A3. $^{87}Sr/^{86}Sr$ and $^{143}Nd/^{144}Nd$ ratios are quoted in the $\varepsilon$Sr and $\varepsilon$Nd notation as deviations from the chondritic reference (CHUR) at the present-day; $^{87}Sr/^{86}Sr$ = 0.7045 and $^{87}Rb/^{86}Sr$ = 0.0827 (DePaolo and Wassenberg, 1979), $^{143}Nd/^{144}Nd$ = 0.512638 and $^{147}Sm/^{144}Nd$ = 0.1966 (O'Nions and others, 1977). The decay constants ($\lambda$) of $^{87}Rb = 1.397\times10^{-11}$ (Villa and others, 2015) and of $^{147}Sm = 6.54\times10^{-12}$ (Lugmair and Marti, 1978) were applied.

### *In Situ Zircon Lu-Hf Isotopic Analysis*

*In situ* zircon hafnium isotopic analysis of sample IK-1 (TTG-I) (table 5) from the Karwar block was carried out at the Institute of Geology and Geophysics, Chinese Academy of Sciences, Beijing. Sites previously dated by SHRIMP were selected for Lu-Hf analyses, and the measurements were performed using a Neptune MC-ICPMS fitted with a 193 nm ArF laser, with spot sizes of 40 to 50 μm and a laser repetition rate of 8 Hz at a laser power of 100 mJ/pulse. Analytical and data correction procedures were as described by Wu and others (2006). To calculate the $^{176}Lu/^{177}Hf$ ratio, interference of $^{176}Lu$ on $^{176}Hf$ was corrected by measuring the intensity of the interference-free $^{175}Lu$, by using the recommended $^{176}Lu/^{175}Lu$ ratio of 0.02669 (DeBievre and Taylor, 1993). To calculate the $^{176}Hf/^{177}Hf$ ratio isobaric interference of $^{176}Yb$ on $^{176}Hf$ was corrected by using the $^{176}Yb/^{172}Yb$ ratio of 0.5886 (Chu and others, 2002). Each ten analyses were bracketed by analysis of the standards Mud Tank and GJ-1.

### *In Situ Zircon Oxygen Isotope Analyses*

Zircon U-Pb dates were obtained using a sensitive high-resolution ion microprobe (SHRIMP II) at the National Institute of Polar Research (NIPR), Tokyo, Japan. Zircon oxygen isotopic compositions were measured for TTG sample IK-1 and granite sample IK-2 (Appendix table A5) using the SHRIMP II multi-collector ion microprobe at the Australian National University, Canberra, with techniques based on those described by Ickert and others (2008). In brief, following a light polish to remove the geochronology spots, the same areas dated by U-Pb were analyzed for $^{18}O/^{16}O$ using a *ca.* 30 μm diameter, 15 kV, *ca.* 3.5 nA beam of $Cs^+$ primary ions. Negative secondary oxygen ions were extracted at 10 kV and mass analyzed in multicollector mode with a pair of Faraday cups and electrometers operated in resistor mode ($10^{11}$ Ω). The count rate for $^{16}O$ was *ca.* 1.7 GHz. Build-up of positive charge on the sample surface was neutralized using a low energy, broadly focused beam of electrons. Each analysis took *ca.* 7 min, consisting of 5 min of pre-conditioning, baseline measurements and tuning, and 2 min of isotopic measurement. Measured ratios were normalized to the isotopic composition of TEMORA 2 zircon ($\delta\ ^{18}O$ = 8.2 ‰; Valley, 2003) following a small correction for electron-induced secondary ion emission. The standard deviation of repeated measurements of TEMORA 2 over two analytical sessions was 0.22 and 0.27 ‰ respectively, giving an uncertainty in the mean of 0.07 ‰, which was added in quadrature to the individual sample analyses in calculating estimates of their accuracy.

REFERENCES

Adam, J., Rushmer, T., O'Neil, J., and Francis, D., 2012, Hadean greenstones from the Nuvvuagittuq fold belt and the origin of the Earth's early continental crust: Geology, v. 40, n. 4, p. 363–366, https://doi.org/10.1130/G32623.1

Armistead, S. E., Collins, A. S., Payne, J. L., Foden, J. D., De Waele, B., Shaji, E., and Santosh, M., 2018, A re-evaluation of the Kumta Suture in western peninsular India and its extension into Madagascar: Journal of Asian Earth Sciences, v. 157, p. 317–328, https://doi.org/10.1016/j.jseaes.2017.08.020

Armstrong, R. L., 1981, Radiogenic isotopes: the case for crustal recycling on a near-steady-state no-continental-growth Earth: Philosophical Transactions of the Royal Society of London, v. 301, n. 1461, p. 443–472, https://doi.org/10.1098/rsta.1981.0122

Atherton, M. P., and Petford, N., 1993, Generation of sodium-rich magmas from newly underplated basaltic crust: Nature, v. 362, p. 144–146, https://doi.org/10.1038/362144a0

Barker, F., 1979, Trondhjemite: Definition, environment and hypotheses of origin, *in* Baker, F., editor, Developments in Petrology: Amsterdam, the Netherlands, Elsevier, v. 6, p. 1–12, https://doi.org/10.1016/B978-0-444-41765-7.50006-X

Bédard, J. H., Brouillette, P., Madore, L., and Berclaz, A., 2003, Archaean cratonization and deformation in the northern Superior Province, Canada: an evaluation of plate tectonic versus vertical tectonic models: Precambrian Research, v. 127, n. 1–3, p. 61–87, https://doi.org/10.1016/S0301-9268(03)00181-5

Bindeman, I., Gurenko, A., Sigmarsson, O., and Chaussidon, M., 2008, Oxygen isotope heterogeneity and disequilibria of olivine crystals in large volume Holocene basalts from Iceland: Evidence for magmatic digestion and erosion of Pleistocene hyaloclastites: Geochimica et Cosmochimica Acta, v. 72, n. 17, p. 4397–4420, https://doi.org/10.1016/j.gca.2008.06.010

Black, L. P., Kamo, S. L., Allen, C. M., Davis, D. W., Aleinikoff, J. N., Valley, J. W., Mundil, R., Campbell, I. H., Korsch, R. J., Williams, I. S., and Foudoulis, C., 2004, Improved $^{206}Pb/^{238}U$ microprobe geochronology by the monitoring of a trace-element-related matrix effect; SHRIMP, ID–TIMS, ELA–ICP–MS and oxygen isotope documentation for a series of zircon standards: Chemical Geology, v. 205, n. 1–2, p. 115–140, https://doi.org/10.1016/j.chemgeo.2004.01.003

Bleeker, W., 2003, The late Archean record: a puzzle in ca. 35 pieces: Lithos, v. 71, n. 2–4, p. 99–134, https://doi.org/10.1016/j.lithos.2003.07.003

Bowring, S. A., and Williams, I. S., 1999, Priscoan (4.00-4.03 Ga) orthogneisses from northwestern Canada: Contributions to Mineralogy and Petrology, Beitrage zur Mineralogie und Petrologie, v. 134, p. 3–16, https://doi.org/10.1007/s004100050465

Brown, M., Johnson, T., and Gardiner, N. J., 2020, Plate tectonics and the Archean Earth: Annual Review of Earth and Planetary Sciences, v. 48, p. 291–320, https://doi.org/10.1146/annurev-earth-081619-052705

Cawood, P. A., Kröner, A., Collins, W. J., Kusky, T. M., Mooney, W. D., and Windley, B. F., 2009, Accretionary orogens through Earth history: Geological Society of London, Special Publications, v. 318, p. 1–36, https://doi.org/10.1144/SP318.1

Cawood, P. A., Hawkesworth, C. J., and Dhuime, B., 2013, The continental record and the generation of continental crust: Geological Society of America Bulletin, v. 125, n. 1–2, p. 14–32, https://doi.org/10.1130/B30722.1

Chardon, D., Jayananda, M., Chetty, T. R. K., and Peucat, J.-J., 2008, Precambrian continental strain and shear zone patterns: South Indian case: Journal of Geophysical Research: Solid Earth, v. 113, n. B8, https://doi.org/10.1029/2007JB005299

Chowdhury, P., Chakraborty, S., Gerya, T. V., Cawood, P. A., and Capitanio, F. A., 2020, Peel-back controlled lithospheric convergence explains the secular transitions in Archean metamorphism and magmatism: Earth and Planetary Science Letters, v. 538, 116224, https://doi.org/10.1016/j.epsl.2020.116224

Chu, N.-C., Taylor, R. N., Chavagnac, V., Nesbitt, R. W., Boella, R. M., Milton, J. A., German, C. R., Bayon, G., and Burton, K., 2002, Hf isotope ratio analysis using multi-collector inductively coupled plasma mass spectrometry: an evaluation of isobaric interference corrections: Journal of Analytical Atomic Spectrometry, v. 17, n. 12, p. 1567–1574, https://doi.org/10.1039/b206707b

Condie, K. C., 1986, Origin and early growth rate of continents: Precambrian Research, v. 32, n. 4, p. 261–278, https://doi.org/10.1016/0301-9268(86)90032-X

Condie, K. C., 2005, TTGs and adakites: are they both slab melts? Lithos, v. 80, n. 1–4, p. 33–44, https://doi.org/10.1016/j.lithos.2003.11.001

Condie, K. C., and Pease, V., 2008, When did plate tectonics begin on planet earth?: Geological Society of America, Special Paper, v. 440, p. 281–294, https://doi.org/10.1130/SPE440

De Biévre, P., and Taylor, P. D. P., 1993, Table of the isotopic compositions of the elements: International Journal of Mass Spectrometry and Ion Processes, v. 123, n. 2, p. 149–166, https://doi.org/10.1016/0168-1176(93)87009-H

DePaolo, D. J., and Wasserburg, G. J., 1979, Neodymium isotopes in flood basalts from the Siberian Platform and inferences about their mantle sources: Proceedings of the National Academy of Sciences of the United States of America, v. 76, n. 7, p. 3056–3060, https://doi.org/10.1073/pnas.76.7.3056

Dessai, A. G., Arolkar, D. B., French, D., Viegas, A., and Viswanath, T. A., 2009, Petrogenesis of the Bondla layered mafic-ultramafic complex, Usgaon, Goa: Journal of the Geological Society of India, v. 73, p. 697–714, https://doi.org/10.1007/s12594-009-0054-4

de Wit, M. J., Furnes, H., and Robins, B., 2011, Geology and tectonostratigraphy of the Onverwacht Suite, Barberton Greenstone Belt, South Africa: Precambrian Research, v. 186, n. 1–4, p. 1–27, https://doi.org/10.1016/j.precamres.2010.12.007

Dey, S., 2013, Evolution of Archaean crust in the Dharwar craton: The Nd isotope record: Precambrian Research, v. 227, p. 227–246, https://doi.org/10.1016/j.precamres.2012.05.005
Dhuime, B., Hawkesworth, C. J., Cawood, P. A., and Storey, C. D., 2012, A change in the geodynamics of continental growth 3 billion years ago: Science, v. 335, n. 6074, p. 1334–1336, https://doi.org/10.1126/science.1216066
Drummond, M. S., and Defant, M. J., 1990, A model for Trondhjemite-Tonalite-Dacite Genesis and crustal growth via slab melting: Archean to modern comparisons: Journal of Geophysical Research: Solid Earth, v. 95, n. B13, 21503, https://doi.org/10.1029/JB095iB13p21503
Feng, R., and Kerrich, R., 1992, Geochemical evolution of granitoids from the Archean Abitibi Southern Volcanic Zone and the Pontiac subprovince, Superior Province, Canada: Implications for tectonic history and source regions: Chemical Geology, v. 98, n. 1–2, p. 23–70, https://doi.org/10.1016/0009-2541(92)90090-R
Foley, S., 2008, A trace element perspective on Archean crust formation and on the presence or absence of Archean subduction, *in* Condie, K. C., and Pease, V., editors, When Did Plate Tectonics Begin on Planet Earth?: Geological Society of America, Special Papers, v. 440, p. 31–50, https://doi.org/10.1130/2008.2440(02)
Foley, S., Tiepolo, M., and Vannucci, R., 2002, Growth of early continental crust controlled by melting of amphibolite in subduction zones: Nature, v. 417, p. 837–840, https://doi.org/10.1038/nature00799
Foley, S. F., Buhre, S., and Jacob, D. E., 2003, Evolution of the Archaean crust by delamination and shallow subduction: Nature, v. 421, p. 249–252, https://doi.org/10.1038/nature01319
Fyfe, W. S., and McBirney, A. R., 1975. Subduction and the structure of andesitic volcanic belts. American Journal of Science, v. 275-A, p. 285–297.
Garde, A. A., Windley, B. F., Kokfelt, T. F., and Keulen, N., 2020, Archaean plate tectonics in the North Atlantic Craton of West Greenland revealed by well-exposed horizontal crustal tectonics, island arcs and tonalite-trondhjemite-granodiorite complexes: Frontiers in Earth Science, v. 8, 540997, https://doi.org/10.3389/feart.2020.540997
Ge, R., Zhu, W., Wilde, S. A., and Wu, H., 2018, Remnants of Eoarchean continental crust derived from a subducted proto-arc: Science Advances, v. 4, n. 2, eaao3159, https://doi.org/10.1126/sciadv.aao3159
Geological Survey of India, 1993, Hyderabad: Geological map of India, 1: 500000.
Geological Survey of India, 1996, Hyderabad: Geological and Mineral Map of Goa, 1:125000.
Geological Survey of India, 2005, Hyderabad: District Resource map-Uttara Kannada district, Karnataka, 1:250000.
Gerya, T., 2014, Precambrian geodynamics: Concepts and models: Gondwana Research, v. 25, n. 2, p. 442–463, https://doi.org/10.1016/j.gr.2012.11.008
Gerya, T. V., Stern, R. J., Baes, M., Sobolev, S. V., and Whattam, S. A., 2015, Plate tectonics on the Earth triggered by plume-induced subduction initiation: Nature, v. 527, p. 221–225, https://doi.org/10.1038/nature15752
Guitreau, M., Blichert-Toft, J., Martin, H., Mojzsis, S. J., and Albarède, F., 2012, Hafnium isotope evidence from Archean granitic rocks for deep-mantle origin of continental crust: Earth and Planetary Science Letters, v. 337–338, p. 211–223, https://doi.org/10.1016/j.epsl.2012.05.029
Guitreau, M., Mukasa, S. B., Loudin, L., and Krishnan, S., 2017, New constraints on the early formation of the Western Dharwar Craton (India) from igneous zircon U-Pb and Lu-Hf isotopes: Precambrian Research, v. 302, p. 33–49, https://doi.org/10.1016/j.precamres.2017.09.016
Guitreau, M., Boyet, M., Paquette, J.-L., Gannoun, A., Konc, Z., Benbakkar, M., Suchorski, K., and Hénot, J.-M., 2019, Hadean protocrust reworking at the origin of the Archean Napier Complex (Antarctica): Geochemical Perspectives Letters, v. 12, p. 7–11, https://doi.org/10.7185/geochemlet.1927
Guo, J.-L., Gao, S., Wu, Y.-B., Li, M., Chen, K., Hu, Z.-C., Liang, Z.-W., Liu, Y.-S., Zhou, L., Zong, K.-Q., Zhang, W., and Chen, H.-H., 2014, 3.45Ga granitic gneisses from the Yangtze Craton, South China: Implications for Early Archean crustal growth: Precambrian Research, v. 242, p. 82–95, https://doi.org/10.1016/j.precamres.2013.12.018
Hamilton, W., 1969, Mesozoic California and the underflow of pacific mantle: Geological Society of America Bulletin, v. 80, n. 12, p. 2409, https://doi.org/10.1130/0016-7606(1969)80[2409:MCATUO]2.0.CO;2
Harrison, T.M., 2020, Hadean Earth, Springer, ebook, 291 p: Springer International Publishing, https://doi.org/10.1007/978-3-030-46687-9
Hastie, A. R., Kerr, A. C., McDonald, I., Mitchell, S. F., Pearce, J. A., Wolstencroft, M., and Millar, I. L., 2010, Do Cenozoic analogues support a plate tectonic origin for Earth's earliest continental crust? Geology, v. 38, n. 6, p. 495–498, https://doi.org/10.1130/G30778.1
Hastie, A. R., Fitton, J. G., Mitchell, S. F., Neill, I., Nowell, G. M., and Millar, I. L., 2015, Can fractional crystallization, mixing and assimilation processes be responsible for Jamaican-type adakites? Implications for generating eoarchaean continental crust: Journal of Petrology, v. 56, n. 7, p. 1251–1284, https://doi.org/10.1093/petrology/egv029
Hastie, A. R., Fitton, J. G., Bromiley, G. D., Butler, I. B., and Odling, N. W. A., 2016, The origin of Earth's first continents and the onset of plate tectonics: Geology, v. 44, n. 10, p. 855–858, https://doi.org/10.1130/G38226.1
Hawkesworth, C. J., Dhuime, B., Pietranik, A. B., Cawood, P. A., Kemp, A. I. S., and Storey, C. D., 2010, The generation and evolution of the continental crust: Journal of the Geological Society, v. 167, p. 229–248, https://doi.org/10.1144/0016-76492009-072
Hawkesworth, C. J., Cawood, P. A., and Dhuime, B., 2016, Tectonics and crustal evolution: GSA today, v. 26, p. 4–11, https://doi.org/10.1130/GSATG272A.1

Hawkesworth, C., Cawood, P. A., and Dhuime, B., 2020, The evolution of the continental crust and the onset of plate tectonics: Frontiers in Earth Science, v. 8, p. 326, https://doi.org/10.3389/feart.2020.00326

Herwartz, D., Pack, A., and Nagel, T. J., 2021, A $CO_2$ greenhouse efficiently warmed the early Earth and decreased seawater $^{18}O/^{16}O$ before the onset of plate tectonics: Proceedings of the National Academy of Sciences of the United States of America, v. 118, e2023617118, https://doi.org/10.1073/pnas.2023617118

Hoffmann, J. E., Münker, C., Næraa, T., Rosing, M. T., Herwartz, D., Garbe-Schönberg, D., and Svahnberg, H., 2011, Mechanisms of Archean crust formation inferred from high-precision HFSE systematics in TTGs: Geochimica et Cosmochimica Acta, v. 75, n. 15, p. 4157–4178, https://doi.org/10.1016/j.gca.2011.04.027

Hoffmann, J. E., Nagel, T. J., Münker, C., Næraa, T., and Rosing, M. T., 2014, Constraining the process of Eoarchean TTG formation in the Itsaq Gneiss Complex, southern West Greenland: Earth and Planetary Science Letters, v. 388, p. 374–386, https://doi.org/10.1016/j.epsl.2013.11.050

Hokada, T., Horie, K., Satish-Kumar, M., Ueno, Y., Nasheeth, A., Mishima, K., and Shiraishi, K., 2013, An appraisal of Archaean supracrustal sequences in Chitradurga Schist Belt, Western Dharwar Craton, Southern India: Precambrian Research, v. 227, p. 99–119, https://doi.org/10.1016/j.precamres.2012.04.006

Horie, K., Hokada, T., Hiroi, Y., Motoyoshi, Y., and Shiraishi, K., 2012, Contrasting Archaean crustal records in western part of the Napier Complex, East Antarctica: New constraints from SHRIMP geochronology: Gondwana Research, v. 21, n. 4, p. 829–837, https://doi.org/10.1016/j.gr.2011.08.013

Ickert, R. B., Hiess, J., Williams, I. S., Holden, P., Ireland, T. R., Lanc, P., Schram, N., Foster, J. J., and Clement, S. W., 2008, Determining high precision, in situ, oxygen isotope ratios with a SHRIMP II: Analyses of MPI-DING silicate-glass reference materials and zircon from contrasting granites: Chemical Geology, v. 257, n. 1–2, p. 114–128, https://doi.org/10.1016/j.chemgeo.2008.08.024

Irvine, T. N., and Baragar, W. R. A., 1971, A guide to the chemical classification of the common volcanic rocks: Canadian Journal of Earth Sciences, v. 8, n. 5, p. 523–548, https://doi.org/10.1139/e71-055

Ishwar-Kumar, C., ms, 2015, Mesoproterozoic suturing of Archean crustal blocks in western peninsular India: New insights on India-Madagascar correlations: Ph.D. thesis, Centre for Earth Sciences, Indian Institute of Science, Bangalore, India, p. 138–139.

Ishwar-Kumar, C., Windley, B. F., Horie, K., Kato, T., Hokada, T., Itaya, T., Yagi, K., Gouzu, C., and Sajeev, K., 2013, A Rodinian suture in western India: New insights on India-Madagascar correlations: Precambrian Research, v. 236, p. 227–251, https://doi.org/10.1016/j.precamres.2013.07.023

Ishwar-Kumar, C., Sajeev, K., Windley, B. F., Satish-Kumar, M., Hokada, T., Horie, K., and Itaya, T., 2014, Tectonic evolution of Karwar and Coorg blocks, southern India. Japan Geoscience Union Meeting-2014, Yokohama, Tokyo, Japan. Submission No. 00719.

Ishwar-Kumar, C., Rajesh, V. J., Windley, B. F., Razakamanana, T., Itaya, T., Babu, E. V. S. S. K., and Sajeev, K., 2016a, Petrogenesis and tectonic setting of the Bondla mafic-ultramafic complex, western India: Inferences from chromian spinel chemistry: Journal of Asian Earth Sciences, v. 130, p. 192–205, https://doi.org/10.1016/j.jseaes.2016.07.004

Ishwar-Kumar, C., Santosh, M., Wilde, S. A., Tsunogae, T., Itaya, T., Windley, B. F., and Sajeev, K., 2016b, Mesoproterozoic suturing of Archean crustal blocks in western peninsular India: Implications for India–Madagascar correlations: Lithos, v. 263, p. 143–160, https://doi.org/10.1016/j.lithos.2016.01.016

Jagoutz, O., Schmidt, M. W., Enggist, A., Burg, J.-P., Hamid, D., and Hussain, S., 2013, TTG-type plutonic rocks formed in a modern arc batholith by hydrous fractionation in the lower arc crust: Contributions to Mineralogy and Petrology, v. 166, p. 1099–1118, https://doi.org/10.1007/s00410-013-0911-4

Jayananda, M., Moyen, J.-F., Martin, H., Peucat, J.-J., Auvray, B., and Mahabaleswar, B., 2000, Late Archaean (2550–2520 Ma) juvenile magmatism in the Eastern Dharwar craton, southern India: constraints from geochronology, Nd–Sr isotopes and whole rock geochemistry: Precambrian Research, v. 99, n. 3–4, p. 225–254, https://doi.org/10.1016/S0301-9268(99)00063-7

Jayananda, M., Chardon, D., Peucat, J.-J., and Capdevila, R., 2006, 2.61Ga potassic granites and crustal reworking in the western Dharwar craton, southern India: Tectonic, geochronologic and geochemical constraints: Precambrian Research, v. 150, n. 1–2, p. 1–26, https://doi.org/10.1016/j.precamres.2006.05.004

Jayananda, M., Kano, T., Peucat, J., and Channabasappa, S., 2008, 3.35Ga komatiite volcanism in the western Dharwar craton, southern India: Constraints from Nd isotopes and whole-rock geochemistry: Precambrian Research, v. 162, n. 1–2, p. 160–179, https://doi.org/10.1016/j.precamres.2007.07.010

Jayananda, M., Peucat, J.-J., Chardon, D., Rao, B. K., Fanning, C. M., and Corfu, F., 2013, Neoarchean greenstone volcanism and continental growth, Dharwar craton, southern India: Constraints from SIMS U–Pb zircon geochronology and Nd isotopes: Precambrian Research, v. 227, p. 55–76, https://doi.org/10.1016/j.precamres.2012.05.002

Jayananda, M., Chardon, D., Peucat, J.-J., Tushipoklaand Fanning, C. M., 2015, Paleo- to Mesoarchean TTG accretion and continental growth in the western Dharwar craton, Southern India: Constraints from SHRIMP U–Pb zircon geochronology, whole-rock geochemistry and Nd–Sr isotopes: Precambrian Research, v. 268, p. 295–322, https://doi.org/10.1016/j.precamres.2015.07.015

Jayananda, M., Santosh, M., and Aadhiseshan, K. R., 2018, Formation of Archean (3600–2500 Ma) continental crust in the Dharwar Craton, southern India: Earth-Science Reviews, v. 181, p. 12–42, https://doi.org/10.1016/j.earscirev.2018.03.013

Jayananda, M., Guitreau, M., Thomas, T. T., Martin, H., Aadhiseshan, K. R., Gireesh, R. V., Peucat, J.-J., and Satyanarayanan, M., 2020, Geochronology and geochemistry of Meso- to Neoarchean magmatic epidote-bearing potassic granites, western Dharwar Craton (Bellur–Nagamangala–Pandavpura corridor), southern India: implications for the successive stages of crustal reworking and cratonization: Geological Society, London, Special Publication, v. 489, p. 79–114, https://doi.org/10.1144/SP489-2018-125

Jena, B. K., 1985, Usgaon ultramafic-gabbro complex, Goa: Journal of the Geological Society of India, v. 26, p. 492–495.

Johnson, T. E., Brown, M., Gardiner, N. J., Kirkland, C. L., and Smithies, R. H., 2017, Earth's first stable continents did not form by subduction: Nature, v. 543, p. 239–242, https://doi.org/10.1038/nature21383

Johnson, T. E., Kirkland, C. L., Gardiner, N. J., Brown, M., Smithies, R. H., and Santosh, M., 2019, Secular change in TTG compositions: Implications for the evolution of Archaean geodynamics: Earth and Planetary Science Letters, v. 505, p. 65–75, https://doi.org/10.1016/j.epsl.2018.10.022

Kagami, H., Okano, O., Sudo, H., and Honma, H., 1982, Isotope analysis of Rb and Sr using a full-automatic thermal ionization mass spectrometer: Okayama Daigaku Onsen Kenkyusho Hokoku, v. 52, p. 51–70.

Kagami, H., Iwata, M., Sano, S., and Honma, H., 1987, Sr and Nd isotopic compositions and Rb, Sr, Sm and Nd concentrations of standard samples: Technical Reports. ISEI, Okayama University of Science Bulletin, v. 4, 116 p.

Komiya, T., Yamamoto, S., Aoki, S., Sawaki, Y., Ishikawa, A., Tashiro, T., Koshida, K., Shimojo, M., Aoki, K., and Collerson, K. D., 2015, Geology of the Eoarchean, >3.95Ga, Nulliak supracrustal rocks in the Saglek Block, northern Labrador, Canada: The oldest geological evidence for plate tectonics: Tectonophysics, v. 662, p. 40–66, https://doi.org/10.1016/j.tecto.2015.05.003

Kröner, A., Windley, B. F., Badarch, G., Tomurtogoo, O., Hegner, E., Jahn, B. M., Gruschka, S., Khain, E. V., Demoux, A., and Wingate, M. T. D., 2007, Accretionary growth and crust formation in the Central Asian Orogenic Belt and comparison with the Arabian-Nubian shield, *in* Hatcher, R. D., Carlson, M. P., McBride, J. H., and Catalán, J. R. M., editors, 4-D Framework of Continental Crust: Geological Society of America Memoirs, v. 200, p. 181–209, https://doi.org/10.1130/2007.1200(11)

Kushev, V.G., and Kornilov, M.F. 1997, The Ukrainian Shield, *in* de Wit, M. J., and Ashwal, L.D., editors, Greenstone Belts: Oxford, United Kingdom, Clarendon Press, p. 726–729.

Laurent, O., Martin, H., Moyen, J. F., and Doucelance, R., 2014, The diversity and evolution of late-Archean granitoids: Evidence for the onset of "modern-style" plate tectonics between 3.0 and 2.5Ga: Lithos, v. 205, p. 208–235, https://doi.org/10.1016/j.lithos.2014.06.012

Li, S.-S., Santosh, M., Farkaš, J., Redaa, A., Ganguly, S., Kim, S. W., Zhang, C., Gilbert, S., and Zack, T., 2020, Coupled U-Pb and Rb-Sr laser ablation geochronology trace Archean to Proterozoic crustal evolution in the Dharwar Craton, India: Precambrian Research, v. 343, p. 105709, https://doi.org/10.1016/j.precamres.2020.105709

Liu, D., Wilde, S. A., Wan, Y., Wu, J., Zhou, H., Dong, C., and Yin, X., 2008, New U-Pb and Hf isotopic data confirm Anshan as the oldest preserved segment of the North China Craton: American Journal of Science, v. 308, n. 3, p. 200–231, https://doi.org/10.2475/03.2008.02

Ludwig, K. R., 2008, User's Manual for Isoplot 3.6: A Geochronological Toolkit for Microsoft Excel: Berkeley Geochronology Center, Special Publication No. 4, 77 p.

Lugmair, G. W., and Marti, K., 1978, Lunar initial $^{143}Nd/^{144}Nd$: Differential evolution of the lunar crust and mantle: Earth and Planetary Science Letters, v. 39, n. 3, p. 349–357, https://doi.org/10.1016/0012-821X(78)90021-3

Manikyamba, C., Ganguly, S., Santosh, M., and Subramanyam, K. S. V., 2017, Volcano-sedimentary and metallogenic records of the Dharwar greenstone terranes, India: Window to Archean plate tectonics, continent growth, and mineral endowment: Gondwana Research, v. 50, p. 38–66, https://doi.org/10.1016/j.gr.2017.06.005

Martin, H., 1986, Effect of steeper Archean geothermal gradient on geochemistry of subduction-zone magmas: Geology, v. 14, n. 9, p. 753–756, https://doi.org/10.1130/0091-7613(1986)14<753:EOSAGG>2.0.CO;2

Martin, H., Moyen, J.-F., Guitreau, M., Blichert-Toft, J., and Le Pennec, J.-L., 2014, Why Archaean TTG cannot be generated by MORB melting in subduction zones: Lithos, v. 198–199, p. 1–13, https://doi.org/10.1016/j.lithos.2014.02.017

Meschede, M., 1986, A method of discriminating between different types of mid-ocean ridge basalts and continental tholeiites with the Nb-Zr-Y diagram: Chemical Geology, v. 56, n. 3–4, p. 207–218, https://doi.org/10.1016/0009-2541(86)90004-5

Mishra, S., Deomurari, M. P., Wiedenbeck, M., Goswami, J. N., Ray, S., and Saha, A. K., 1999, $^{207}Pb/^{206}Pb$ zircon ages and the evolution of the Singhbhum Craton, eastern India: an ion microprobe study: Precambrian Research, v. 93, n. 2–3, p. 139–151, https://doi.org/10.1016/S0301-9268(98)00085-0

Miyazaki, T., and Shuto, K., 1998, Sr and Nd isotope ratios of twelve GSJ rock reference samples: Geochemical Journal, v. 32, n. 5, p. 345–350, https://doi.org/10.2343/geochemj.32.345

Moore, W. B., and Webb, A. A. G., 2013, Heat-pipe Earth: Nature, v. 501, p. 501–505, https://doi.org/10.1038/nature12473

Moyen, J.-F., 2011, The composite Archaean grey gneisses: Petrological significance, and evidence for a non-unique tectonic setting for Archaean crustal growth: Lithos, n. 1–4, v. 123, p. 21–36, https://doi.org/10.1016/j.lithos.2010.09.015

Moyen, J.-F., and Stevens, G., 2006, Experimental constraints on TTG petrogenesis: Implications for Archean geodynamics, *in* Benn, K., Mareschal, J.-C., and Condie, K. C., editors, Archean Geodynamics and Environments: American Geophysical Union, Geophysical Monograph Series, v. 164, p. 149–175, https://doi.org/10.1029/164GM11

Moyen, J.-F., and Martin, H., 2012, Forty years of TTG research: Lithos, v. 148, p. 312–336, https://doi.org/10.1016/j.lithos.2012.06.010

Moyen, J.-F., Martin, H., Jayananda, M., and Auvray, B., 2003, Late Archaean granites: a typology based on the Dharwar Craton (India): Precambrian Research, v. 127, n. 1–3, p. 103–123, https://doi.org/10.1016/S0301-9268(03)00183-9

Næraa, T., Scherstén, A., Rosing, M. T., Kemp, A. I. S., Hoffmann, J. E., Kokfelt, T. F., and Whitehouse, M. J., 2012, Hafnium isotope evidence for a transition in the dynamics of continental growth 3.2 Gyr ago: Nature, v. 485, p. 627–630, https://doi.org/10.1038/nature11140

Nagel, T. J., Hoffmann, J. E., and Münker, C., 2012, Generation of Eoarchean tonalite-trondhjemite-granodiorite series from thickened mafic arc crust: Geology, v. 40, n. 4, p. 375–378, https://doi.org/10.1130/G32729.1

Nelson, D. R., 1997, Compilation of SHRIMP U-Pb zircon geochronology data, 1996: Perth, Australia, Western Australia Geological Survey, Record, v. 1997/2, 189 p.

Neo, N., Yamazaki, S., and Miyashita, S., 2009, Data report: bulk rock compositions of samples from the IODP Expedition 309/312 sample pool, ODP Hole 1256D, Proceedings of the IODP: Integrated Ocean Drilling Program, https://doi.org/10.2204/iodp.proc.309312.204.2009

Nutman, A. P., Bennett, V. C., and Friend, C. R. L., 2015, The emergence of the Eoarchaean proto-arc: evolution of a c. 3700 Ma convergent plate boundary at Isua, southern West Greenland: Geological Society, London, Special Publications, v. 389, p. 113–133, https://doi.org/10.1144/SP389.5

O'Neil, J., Carlson, R. W., Paquette, J.-L., and Francis, D., 2012, Formation age and metamorphic history of the Nuvvuagittuq Greenstone Belt: Precambrian Research, v. 220–221, p. 23–44, https://doi.org/10.1016/j.precamres.2012.07.009

O'Neill, C., Turner, S., and Rushmer, T., 2018, The inception of plate tectonics: a record of failure: Philosophical Transactions of the Royal Society A: Mathematical, Physical, and Engineering Sciences, v. 376, n. 2132, 20170414, https://doi.org/10.1098/rsta.2017.0414

O'Nions, R. K., Hamilton, P. J., and Evensen, N. M., 1977, Variations in 143Nd/144Nd and 87Sr/86Sr ratios in oceanic basalts: Earth and Planetary Science Letters, v. 34, n. 1, p. 13–22, https://doi.org/10.1016/0012-821X(77)90100-5

Ohta, H., Maruyama, S., Takahashi, E., Watanabe, Y., and Kato, Y., 1996, Field occurrence, geochemistry and petrogenesis of the Archean Mid-Oceanic Ridge Basalts (AMORBs) of the Cleaverville area, Pilbara Craton, Western Australia: Lithos, v. 37, n. 2–3, p. 199–221, https://doi.org/10.1016/0024-4937(95)00037-2

Paces, J. B., and Miller, J. D. Jr, , 1993, Precise U-Pb ages of Duluth Complex and related mafic intrusions, northeastern Minnesota: Geochronological insights to physical, petrogenetic, paleomagnetic, and tectonomagmatic processes associated with the 1.1 Ga Midcontinent Rift System: Journal of Geophysical Research: Solid Earth, v. 98, n. B8, p. 13997–14013, https://doi.org/10.1029/93JB01159

Palin, R. M., White, R. W., and Green, E. C. R., 2016, Partial melting of metabasic rocks and the generation of tonalitic–trondhjemitic–granodioritic (TTG) crust in the Archaean: Constraints from phase equilibrium modelling: Precambrian Research, v. 287, p. 73–90, https://doi.org/10.1016/j.precamres.2016.11.001

Pearce, J. A., 1982, Trace element characteristics of lavas from destructive plate boundaries, *in* Thorpe, R. S., editor., Andesites: Orogenic andesites and related rocks: John Wiley and Sons, Chichester, England, p. 528–548.

Pearce, J. A., 1996, A user's guide to basalt discrimination diagrams, Trace element geochemistry of volcanic rocks: applications for massive sulphide exploration: Geological Association of Canada, Short Course Notes, v. 12, 113 p.

Pearce, J. A., 2008, Geochemical fingerprinting of oceanic basalts with applications to ophiolite classification and the search for Archean oceanic crust: Lithos, v. 100, n. 1–4, p. 14–48, https://doi.org/10.1016/j.lithos.2007.06.016

Pearce, J. A., and Cann, J. R., 1973, Tectonic setting of basic volcanic rocks determined using trace element analyses: Earth and Planetary Science Letters, v. 19, n. 2, p. 290–300, https://doi.org/10.1016/0012-821X(73)90129-5

Pearce, J. A., and Gale, G. H., 1977, Identification of ore-deposition environment from trace-element geochemistry of associated igneous host rocks: Geological Society, London, Special Publications, v. 7, p. 14–24, https://doi.org/10.1144/GSL.SP.1977.007.01.03

Pearce, J. A., Harris, N. B. W., and Tindle, A. G., 1984, Trace element discrimination diagrams for the tectonic interpretation of granitic rocks: Journal of Petrology, v. 25, p. 956–983, https://doi.org/10.1093/petrology/25.4.956

Peucat, J.-J., Jayananda, M., Chardon, D., Capdevila, R., Fanning, C. M., and Paquette, J.-L., 2013, The lower crust of the Dharwar Craton, Southern India: Patchwork of Archean granulitic domains: Precambrian Research, v. 227, p. 4–28, https://doi.org/10.1016/j.precamres.2012.06.009

Polat, A., 2012, Growth of Archean continental crust in oceanic island arcs: Geology, v. 40, n. 4, p. 383–384, https://doi.org/10.1130/focus042012.1

Ranjan, S., Upadhyay, D., Abhinay, K., and Srikantappa, C., 2020, Paleoarchean and Neoarchean Tonalite–Trondhjemite–Granodiorite (TTG) and granite magmatism in the Western Dharwar Craton, southern India: Implications for Archean continental growth and geodynamics: Precambrian Research, v. 340, p. 105630, https://doi.org/10.1016/j.precamres.2020.105630

Ratheesh-Kumar, R. T., Santosh, M., Yang, Q.-Y., Ishwar-Kumar, C., Chen, N.-S., and Sajeev, K., 2016, Archean tectonics and crustal evolution of the Biligiri Rangan Block, southern India: Precambrian Research, v. 275, p. 406–428, https://doi.org/10.1016/j.precamres.2016.01.022

Ratheesh-Kumar, R. T., Windley, B. F., Xiao, W. J., Jia, X.-L., Mohanty, D. P., and Zeba-Nezrin, F. K., 2020, Early growth of the Indian lithosphere: Implications from the assembly of the Dharwar Craton and adjacent granulite blocks, southern India: Precambrian Research, v. 336, 105491, https://doi.org/10.1016/j.precamres.2019.105491

Rekha, S., and Bhattacharya, A., 2013, Growth, preservation of Paleoproterozoic-shear-zone-hosted monazite, north of the Western Dharwar Craton (India), and implications for Gondwanaland assembly: Contributions to Mineralogy and Petrology, v. 166, p. 1203–1222, https://doi.org/10.1007/s00410-013-0917-y

Rekha, S., and Bhattacharya, A., 2014, Paleoproterozoic/Mesoproterozoic tectonism in the northern fringe of the Western Dharwar Craton (India): Its relevance to Gondwanaland and Columbia supercontinent reconstructions: Tectonics, v. 33, p. 552–580, https://doi.org/10.1002/2013TC003335

Rekha, S., Viswanath, T. A., Bhattacharya, A., and Prabhakar, N., 2013, Meso/Neoarchean crustal domains along the north Konkan coast, western India: The Western Dharwar Craton and the Antongil-Masora Block (NE Madagascar) connection: Precambrian Research, v. 233, p. 316–336, https://doi.org/10.1016/j.precamres.2013.05.008

Rekha, S., Bhattacharya, A., and Chatterjee, N., 2014, Tectonic restoration of the Precambrian crystalline rocks along the west coast of India: Correlation with eastern Madagascar in East Gondwana: Precambrian Research, v. 252, p. 191–208, https://doi.org/10.1016/j.precamres.2014.07.013

Rickwood, P. C., 1989, Boundary lines within petrologic diagrams which use oxides of major and minor elements: Lithos, v. 22, n. 4, p. 247–263, https://doi.org/10.1016/0024-4937(89)90028-5

Roberts, N. M. W., Van Kranendonk, M. J., Parman, S., and Clift, P. D., 2015, Continent formation through time: Geological Society, London, Special Publications, v. 389, p. 1–16, https://doi.org/10.1144/SP389.0

Rollinson, H., 2009, New models for the genesis of plagiogranites in the Oman ophiolite: Lithos, v. 112, n. 3–4, p. 603–614, https://doi.org/10.1016/j.lithos.2009.06.006

Rollinson, H., 2010, Coupled evolution of Archean continental crust and subcontinental lithospheric mantle: Geology, v. 38, n. 12, p. 1083–1086, https://doi.org/10.1130/G31159.1

Rozel, A. B., Golabek, G. J., Jain, C., Tackley, P. J., and Gerya, T., 2017, Continental crust formation on early Earth controlled by intrusive magmatism: Nature, v. 545, p. 332–335, https://doi.org/10.1038/nature22042

Schofield, D. I., Thomas, R. J., Goodenough, K. M., De Waele, B., Pitfield, P. E. J., Key, R. M., Bauer, W., Walsh, G. J., Lidke, D. J., Ralison, A. V., Rabarimanana, M., Rafahatelo, J. M., and Randriamananjara, T., 2010, Geological evolution of the Antongil Craton, NE Madagascar: Precambrian Research, v. 182, n. 3, p. 187–203, https://doi.org/10.1016/j.precamres.2010.07.006

Sengör, A. M. C., and Natal'in, B. A., 1996, Turkic-type orogeny and its role in the making of the continental crust: Annual Review of Earth and Planetary Sciences, v. 24, p. 263–337, https://doi.org/10.1146/annurev.earth.24.1.263

Shaw, D. M., 1970, Trace element fractionation during anatexis: Geochimica et Cosmochimica Acta, v. 34, n. 2, p. 237–243, https://doi.org/10.1016/0016-7037(70)90009-8

Shervais, J. W., 1982, Ti-V plots and the petrogenesis of modern and ophiolitic lavas: Earth and Planetary Science Letters, v. 59, p. 101–118, https://doi.org/10.1016/0012-821X(82)90120-0

Shirey, S. B., and Richardson, S. H., 2011, Start of the Wilson Cycle at 3 Ga Shown by Diamonds from Subcontinental Mantle: Science, v. 333, n. 6041, p. 434–436, https://doi.org/10.1126/science.1206275

Sizova, E., Gerya, T., Stüwe, K., and Brown, M., 2015, Generation of felsic crust in the Archean: A geodynamic modeling perspective: Precambrian Research, v. 271, p. 198–224, https://doi.org/10.1016/j.precamres.2015.10.005

Smithies, R. H., 2000, The Archaean tonalite–trondhjemite–granodiorite (TTG) series is not an analogue of Cenozoic adakite: Earth and Planetary Science Letters, v. 182, n. 1, p. 115–125, https://doi.org/10.1016/S0012-821X(00)00236-3

Smithies, R. H., Champion, D. C., and Van Kranendonk, M. J., 2009, Formation of Paleoarchean continental crust through infracrustal melting of enriched basalt: Earth and Planetary Science Letters, v. 281, p. 298–306, https://doi.org/10.1016/j.epsl.2009.03.003

Smithies, R. H., Lu, Y., Johnson, T. E., Kirkland, C. L., Cassidy, K. F., Champion, D. C., Mole, D. R., Zibra, I., Gessner, K., Sapkota, J., De Paoli, M. C., and Poujol, M., 2019, No evidence for high-pressure melting of Earth's crust in the Archean: Nature Communications, v. 10, 5559, https://doi.org/10.1038/s41467-019-13547-x

Spencer, C. J., 2020, Continuous continental growth as constrained by the sedimentary record: American Journal of Science, v. 320, n. 4, p. 373–401, https://doi.org/10.2475/04.2020.02

Sreehari, L., Toyoshima, T., Satish-Kumar, M., Takahashi, T., and Ueda, H., 2021, Structural and geochemical evidence for a failed rift crustal evolution model in Western Dharwar Craton, South India: Lithos, v. 388–389, 106020, https://doi.org/10.1016/j.lithos.2021.106020

Stacey, J. S., and Kramers, J. D., 1975, Approximation of terrestrial lead isotope evolution by a two-stage model: Earth and Planetary Science Letters, v. 26, n. 2, p. 207–221, https://doi.org/10.1016/0012-821X(75)90088-6

Stern, R. A., Bodorkos, S., Kamo, S. L., Hickman, A. H., and Corfu, F., 2009, Measurement of SIMS Instrumental Mass Fractionation of Pb Isotopes During Zircon Dating: Geostandards and Geoanalytical Research, v. 33, n. 2, p. 145–168, https://doi.org/10.1111/j.1751-908X.2009.00023.x

Sun, S. S., and McDonough, W. F., 1989, Chemical and isotopic systematics of oceanic basalts: implications for mantle composition and processes: Geological Society, London, Special Publications, v. 42, p. 313–345, https://doi.org/10.1144/GSL.SP.1989.042.01.19

Takahashi, T, and Shuto, K., 1997, Major and trace element analyses of silicate rocks using X-ray fluorescence spectrometer RIX3000: Rigaku-Denki Journal, v. 28, p. 25–37.

Taylor, S. R., and McLennan, S. M., 1985, The continental crust: its composition and evolution: Boston, Blackwell Scientific, 312 p.

Taylor, S. R., and McLennan, S. M., 1995, The geochemical evolution of the continental crust: Reviews of Geophysics, v. 33, n. 2, p. 241–265, https://doi.org/10.1029/95RG00262

Turkina, O. M., and Nozhkin, A. D., 2003, Genesis of Archean tonalite-trondhjemite suites: Plume or subduction related?: Russian Journal of Earth Sciences, v. 5, n. 2, p. 93–100, https://doi.org/10.2205/2003ES000121
Turner, S., Rushmer, T., Reagan, M., and Moyen, J.-F., 2014, Heading down early on? Start of subduction on Earth: Geology, v. 42, n. 2, p. 139–142, https://doi.org/10.1130/G34886.1
Upadhyay, D., Chattopadhyay, S., and Mezger, K., 2019, Formation of Paleoarchean-Mesoarchean Na-rich (TTG) and K-rich granitoid crust of the Singhbhum craton, eastern India: Constraints from major and trace element geochemistry and Sr-Nd-Hf isotope composition: Precambrian Research, v. 327, p. 255–272, https://doi.org/10.1016/j.precamres.2019.04.009
Valley, J. W., Bindeman, I. N., and Peck, W. H., 2003, Empirical calibration of oxygen isotope fractionation in zircon: Geochimica et Cosmochimica Acta, v. 67, n. 17, p. 3257–3266, https://doi.org/10.1016/S0016-7037(03)00090-5
van Hunen, J., and Moyen, J.-F., 2012, Archean Subduction: Fact or Fiction? Annual Review of Earth and Planetary Sciences, v. 40, p. 195–219, https://doi.org/10.1146/annurev-earth-042711-105255
Van Kranendonk, M. J., 2011, Onset of Plate Tectonics: Science, v. 333, n. 6041, p. 413–414, https://doi.org/10.1126/science.1208766
Van Kranendonk, M. J., Smithies, R. H., Griffin, W. L., Huston, D. L., Hickman, A. H., Champion, D. C., Anhaeusser, C. R., and Pirajno, F., 2015, Making it thick: a volcanic plateau origin of Palaeoarchean continental lithosphere of the Pilbara and Kaapvaal cratons, *in* Roberts, N. M. W., Van Kranendonk, M., Parman, S., Shirey, S., and Clift, P. D., editors, Continent Formation through Time: Geological Society, London, Special Publications, v. 389, p. 83–111, https://doi.org/10.1144/SP389.12[10.1144/SP389.12]
Vasanthi, A., and Santosh, M., 2021, Lithospheric architecture and geodynamics of the Archean Dharwar craton and surrounding terranes: New insights from satellite gravity investigation: Gondwana Research, v. 95, p. 14–28, https://doi.org/10.1016/j.gr.2021.03.008
Villa, I. M., De Bièvre, P., Holden, N. E., and Renne, P. R., 2015, IUPAC-IUGS recommendation on the half life of 87Rb: Geochimica et Cosmochimica Acta, v. 164, p. 382–385, https://doi.org/10.1016/j.gca.2015.05.025
Wakita, K., Pubellier, M., and Windley, B. F., 2013, Tectonic processes, from rifting to collision via subduction, in SE Asia and the western Pacific: A key to understanding the architecture of the Central Asian Orogenic Belt: Lithosphere, v. 5, n. 3, p. 265–276, https://doi.org/10.1130/L234.1
Wiedenbeck, M., Allé, P., Corfu, F., Griffin, W. L., Meier, M., Oberli, F., von Quadt, A., Roddick, J. C., and Spiegel, W., 1995, Three natural zircon standards for U-Th-PB, Lu-Hf, trace element and Ree analyses: Geostandards Newsletter, v. 19, n. 1, p. 1–23, https://doi.org/10.1111/j.1751-908X.1995.tb00147.x
Willbold, M., Hegner, E., Stracke, A., and Rocholl, A., 2009, Continental geochemical signatures in dacites from Iceland and implications for models of early Archaean crust formation: Earth and Planetary Science Letters, v. 279, n. 1–2, p. 44–52, https://doi.org/10.1016/j.epsl.2008.12.029
Williams, I. S., 1997, U-Th-Pb geochronology by ion microprobe, Applications of Microanalytical Techniques to Understanding Mineralizing Processes: Society of Economic Geologists, p. 1–35, https://doi.org/10.5382/Rev.07.01
Wilson, J. T., 1968, Static or mobile earth: the current scientific revolution: Proceedings of the American Philosophical Society, v. 112, n. 5, p. 309–320.
Winchester, J. A., and Floyd, P. A., 1977, Geochemical discrimination of different magma series and their differentiation products using immobile elements: Chemical Geology, v. 20, p. 325–343, https://doi.org/10.1016/0009-2541(77)90057-2
Windley, B. F., 1977, Timing of continental growth and emergence: Nature, v. 270, p. 426–428, https://doi.org/10.1038/270426a0
Windley, B.F., 1996, The Evolving Continents: Oceanographic Literature Review, v. 43, n. 8, 785 p.
Windley, B. F., Alexeiev, D., Xiao, W., Kröner, A., and Badarch, G., 2007, Tectonic models for accretion of the Central Asian Orogenic Belt: Journal of the Geological Society, v. 164, p. 31–47, https://doi.org/10.1144/0016-76492006-022
Windley, B. F., Kusky, T., and Polat, A., 2021, Onset of plate tectonics by the Eoarchean: Precambrian Research, v. 352, 105980, https://doi.org/10.1016/j.precamres.2020.105980
Wu, F.-Y., Yang, Y.-H., Xie, L.-W., Yang, J.-H., and Xu, P., 2006, Hf isotopic compositions of the standard zircons and baddeleyites used in U–Pb geochronology: Chemical Geology, v. 234, n. 1–2, p. 105–126, https://doi.org/10.1016/j.chemgeo.2006.05.003
Zheng, Y.-F., 2019, Subduction zone geochemistry: Geoscience Frontiers, v. 10, n. 4, p. 1223–1254, https://doi.org/10.1016/j.gsf.2019.02.003
Zincone, S. A., Oliveira, E. P., Laurent, O., Zhang, H., and Zhai, M., 2016, 3.30 Ga high-silica intraplate volcanic–plutonic system of the Gavião Block, São Francisco Craton, Brazil: Evidence of an intracontinental rift following the creation of insulating continental crust: Lithos, v. 266–267, p. 414–434, https://doi.org/10.1016/j.lithos.2016.10.011